Ultracold Fermi mixtures and simultaneous sub-Doppler laser cooling of fermionic 6Li and 40K

Franz Sievers

Département de physique
École Normale Supérieure

Laboratoire Kastler Brossel

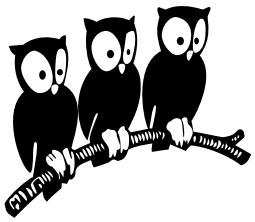

THÉSE de DOCTORAT de l'UNIVERSITÉ PARIS VI

Spécialité : Physique Quantique

présentée par

Franz SIEVERS

pour obtenir le grade de Docteur de l'Université Pierre et Marie Curie (Paris VI)

Ultracold Fermi mixtures and simultaneous sub-Doppler laser cooling of fermionic ^{6}Li and ^{40}K

Soutenue le 21 Juillet 2014

devant le jury composé de :

David Guéry-Odelin	.....	Rapporteur
Bruno Laburthe-Tolra	.....	Rapporteur
Arnaud Landragin	.....	Examinateur
Florian Schreck	.....	Examinateur
Christophe Salomon	.....	Directeur de thèse
Frédéric Chevy	.....	Membre invité

Contents

Abstract

This thesis reports on novel techniques for experimental studies of ultracold, fermionic lithium and potassium quantum gases. The new parts of our ^{6}Li-^{40}K apparatus are described and characterised. We present a narrow-linewidth, all-solid-state laser source, emitting 5 W at 671 nm. We employ the laser source in the context of a novel sub-Doppler cooling mechanism, operating on the D_1 atomic transition of alkali atoms, for laser cooling of lithium. This D_1 molasses allows us to simultaneously cool a mixture of ^{6}Li and ^{40}K atoms to deep sub-Doppler temperatures, while retaining large atom numbers and high atomic densities. The measured phase space densities after the molasses phase are on the order of 10^{-4} for both ^{6}Li and ^{40}K. The D_1 laser cooling paves the way for fast evaporation to quantum degeneracy in magnetic and optical traps. We present the evaporative cooling of ^{40}K atoms. The evaporation starts in an optically plugged magnetic quadrupole trap and continues in an optical dipole trap. At the end of the evaporation, we obtain a quantum degenerate spin-mixture of ^{40}K atoms, with more than 7×10^5 atoms in each of the two spin states and $T/T_\mathrm{F} < 0.34$.

Résumé

Ce travail rend compte de nouvelles techniques développées pour l'étude expérimentale de gaz ultrafroids de lithium et de potassium fermioniques. Les améliorations de notre expérience ^{6}Li-^{40}K y sont décrites et caractérisées. Nous présentons un laser solide de grande finesse capable d'émettre 5 W de puissance à 671 nm. Nous utilisons cette source laser dans le contexte d'une nouvelle technique de refroidissement sub-Doppler, reposant sur la transition atomique D_1 des atomes alcalins, pour refroidir des atomes de lithium. Cette melasse D_1 nous permet de refroidir simultanément les atomes de ^{6}Li et de ^{40}K à des températures bien inférieures à la limite Doppler, tout en manipulant des grands nombres d'atomes à des densités importantes. Nous avons mesuré une densité dans l'espace des phases après l'étape de mélasse de l'ordre de 10^{-4} à la fois pour le ^{6}Li et le ^{40}K. Le refroidissement laser D_1 ouvre la voie à une évaporation rapide vers la dégénérescence quantique dans un piège magnétique ou optique. Nous présentons le refroidissement évaporatif d'atomes de ^{40}K. L'évaporation débute dans une piège magnétique pluggé et continue dans un piège dipolaire optique. A l'issue de l'évaporation, nous obtenons un mélange de spins dégénéré, avec plus de 7×10^5 atomes dans chacun des deux états de spin et une température $T/T_F < 0.34$.

1 Introduction

1.1 Quantum gases

The study of ultracold dilute quantum gases is one of the most active research fields in modern quantum physics. The observation of quantum phenomena becomes possible, simply by cooling the trapped gas. At low temperatures, when the de Broglie wavelength reaches a size comparable to the interparticle separation, quantum statistics begin to play a dominant role.

At ultralow temperatures, particles can not be treated as point like and distinguishable any more, because the wave nature of the particles becomes apparent. Quantum statistics becomes important for a gas of indistinguishable particles. There are two categories, determined by the intrinsic angular momentum of the particle, the spin. Bosons have an integer spin and obey Bose-Einstein statistics. They tend to gather in one quantum state. This can lead to the formation of a Bose-Einstein condensate (BEC) [1–3], a macroscopic occupation of the ground state. The coherence in a BEC introduces a frictionless motion of particles, called superfluidity. Fermions have a half-integer spin and underlie the Pauli exclusion principle, which hinders identical fermions to occupy the same quantum state. Therefore, at zero temperature, they fill up the motional energy levels to the Fermi energy, resulting in the so-called Fermi sea [4]. In contrast to Bosons, the transition from the classical to the quantum degenerate Fermi gas occurs gradually, and is not accompanied by a phase transition.

Bose-Einstein condensation is a statistical phenomenon, not requiring any interactions [5, 6]. The first BEC of weakly-interacting alkali atoms was experimentally realized in 1995. A review of experiments on BEC is given in [7–10]. The review includes macroscopic matter wave interference [11], the creation of vortices [12,13], proving the superfluid character of BECs, dark [14,15] and bright solitons [16,17], the realization of two-dimensional gases [18–21], and the superfluid to Mott insulator transition in an optical lattice [22].

A dilute classical gas at low temperatures is rarely colliding, because the mean free path is larger than the interparticle spacing. In the quantum regime, the wave nature and the quantum statistics also modify the physics of collisions [23]. It is possible to tune

the collision cross section of a quantum gas by means of Feshbach resonances [24], where the scattering state resonantly couples to a bound state. This allows one to enter the regime of strong interactions, where $n|a|^3 \gtrsim 1$. Here, n is the atomic density and a the scattering length, characterizing the two-body interaction at low temperatures.

The regime of strong interactions is an active and challenging research field. The theoretical models are complex and experiments with highly controllable model systems are required [25–28]. The investigation of strongly interacting quantum matter forms the basis of a better understanding for a variety of systems like neutron stars, white dwarfs, a quark-gluon plasma, or high-temperature superconductors. This knowledge might ultimately lead to new technological applications.

1.2 Ultracold atoms – a highly controllable model system

The unprecedented degree of control over many system parameters makes ultracold Fermi gases an ideal model system to investigate quantum many body phenomena. Let us consider an experiment with a mixture of two components, 1 and 2. The components could be two different states of one atomic species or two different atomic species. The various parameters of the two components that can be controlled, range from the element and state of the component, the temperature, the populations of the components, the interatomic interaction strength, the mass ratio, over the confinement to the dimensionality of the system.

In an ultracold atom experiment, all these parameters can be varied from one experimental cycle to another. The cycling time of an usual ultracold atom experiment is on the order of some tens of seconds. Therefore, it is possible to investigate full phase diagrams and examine phase transitions.

Another advantage of ultracold atom experiments is the variety of existing tools to probe the gas, such as radio-frequency (RF) spectroscopy [29], Ramsey interference [30], Bragg spectroscopy [31], quantum noise correlations [32–35], single side imaging in optical lattices [36–38], or time of flight (TOF) measurements [39], where the gas can freely expand after it has been released from the trap. Absorption images yield important information about each component, such as the atom number, and the atomic distribution in real- and momentum space. One experimental run consists of setting the parameters, probing the gas and analyzing the absorption images. Most of the data points presented in this thesis are obtained by a series of such runs.

1.3 Quantum degenerate Fermi gases

A Fermi gas is quantum degenerate when its temperature is lower than the Fermi temperature $T_F = E_F/k_B$, where E_F is the Fermi energy and k_B the Boltzmann constant. The first degenerate Fermi gas was realized with ^{40}K [4], by adopting the cooling methods developed to reach BEC with bosonic atoms. At ultracold temperatures, the Fermi gas shows a strong deviation from the classical behaviour, unveiling the Fermi-Dirac distribution of the fermions over the trap states. To date, fermionic quantum degeneracy has also been reached for ^{6}Li [40,41], metastable ^{3}He* [42], the rare earth elements ^{173}Yb [43], ^{161}Dy [44] and recently ^{167}Er [45], and the alkaline earth element ^{87}Sr [46,47]. Early experiments reached temperatures of about one quarter of the Fermi temperature. State-of-the-art experiments cool the atoms to below one tenth the Fermi temperature [48,49].

Reaching quantum degeneracy requires evaporative cooling, a method relying on the rethermalization of the gas by elastic collisions. Cooling Fermi gases is challenging, because ultracold gases only collide via s-wave collisions, and the Pauli exclusion principle prohibits these collisions for indistinguishable fermions. Therefore, the gas has to be either prepared in two different internal states or sympathetically cooled. Furthermore, the collision rate for fermions decreases for low temperatures, because scattering in low-lying momentum states requires these states to be empty, and becomes less likely [4, 50]. In addition, inelastic collisions diminish the cooling efficiency and can create hole excitations deep in the Fermi sea [51,52].

To reach quantum degeneracy, several approaches are in use. The single-species evaporation scheme with two different internal states has been used for ^{40}K [4], ^{6}Li [53,54] and ^{173}Yb [43]. Sympathetic cooling with bosons has been employed for ^{6}Li-^{7}Li [40,41], ^{6}Li-^{23}Na [48], ^{6}Li-^{87}Rb [55], ^{40}K-^{87}Rb [56–60], ^{3}He*-^{4}He* [42], ^{6}Li-^{40}K-^{87}Rb [61] and ^{6}Li-^{40}K-^{41}K [62]. The Fermi-Fermi mixture ^{6}Li-^{40}K has been cooled with several methods. In Innsbruck, ^{6}Li in two spin states is cooled in an optical trap, sympathetically cooling ^{40}K along [63]. The Amsterdam group performed evaporation of a ^{40}K spin-mixture in a magnetic trap, sympathetically cooling ^{6}Li along.

Early experiments investigated one-component, nearly ideal, non-interacting Fermi gases and their thermodynamics [4, 40, 64]. Interacting Fermi gases, composed of two components, became accessible by tuning the interactions between atoms using Feshbach resonances [65, 66]. These resonances, where two colliding atoms couple resonantly to a bound molecular state, were first investigated in bosonic systems [24]. By applying a magnetic field, one can change the relative energy of the colliding atoms and the bound state and hence tune the scattering length [67].

The research on strongly interacting Fermi gases began with the characterization of Feshbach resonances in fermionic systems, e.g. for ^{6}Li [68–70] and ^{40}K [71–73]. In contrast to Bosons, fermionic atoms are quite stable in the vicinity of a Feshbach resonance, because the Pauli exclusion principle prohibits three-body relaxation [74]. Therefore, it was possible to create a Bose-Einstein condensate of weakly bound Feshbach molecules [75–77]. Subsequently, also the Bardeen-Cooper-Schriefer (BCS)-type superfluid was realized [78–80], where the pairing mechanism for weakly attractive interactions is not molecule formation but Cooper pairing. The stability of strongly interacting fermions enabled the investigation of the crossover from the BEC- to the BCS-type superfluid [80–82]. The crossover smoothly connects the two superfluid states across the strongly interacting regime.

Experiments with strongly interacting ultracold Fermi gases proved the superfluid character by the creation of vortices [83], studied fermionic mixtures with population imbalance, leading to a phase separation between paired and unpaired fermions [84,85], measured the speed of sound in a Fermi gas [86] and the critical velocities [87]. Moreover, a fermionic Mott insulator was realized [88, 89] and the equation of state of a strongly interacting Fermi gas was directly measured [49, 90, 91]. The list could be continued, and is only a selection of examples, meant to illustrate the activity in this field of research.

For a strongly interacting Fermi gas, the transition to a superfluid of paired fermions occurs at a relatively high critical temperature relative to the Fermi temperature, $T_C \sim 0.17\,T_F$ [92,93]. Therefore, strongly interacting Fermi gases might play an important role for understanding high-T_C superconductivity, and future experiments could throw new light on the underlying physics of this phenomenon [94].

1.4 Fermi-Fermi mixtures with two different atomic species

The study of mixtures of two different fermionic species is intriguing, because of the large number of controllable system parameters, such as the mass-imbalance and the dimensionality of the system. The different mass of the two species yields unmatched Fermi surfaces and symmetric BCS pairing cannot occur. New quantum phases with different pairing mechanisms are predicted [95]. For instance the Fulde-Ferrell-Larkin-Ovchinnikov (FFLO) state [96–98] or the breached pair state [99, 100]. Other phenomena such as a crystalline phase transition [101] and the formation of long-lived trimers [102] might exist. One can study bosonic polar molecules with long-range dipole-dipole interactions [103, 104].

Furthermore, species-selective potentials [105,106] can be used to study systems in mixed dimensions, where species 1 particles evolve in three dimensions and species 2 evolve in two, one or zero dimensions [107]. The mixed dimensionality influences the two-body interaction leading to confinement induced resonances [108–112]. The 3D-0D case corresponds to the Anderson impurity model and can lead to Kondo correlated states [113–115]. A dilute gas of trapped impurity scatterers also provides a novel system to study Anderson localization [116–118]. Few-body effects such as p-wave resonances between species 1-2 dimers and species 1 atoms tunable by the lattice depth [102], and the Efimov-effect in mixed dimensions [119] can be studied. New many-body quantum phases, where species 1 mediates interactions between species 2 atoms in different layers might lead to interlayer superfluidity [120].

The mixture ^{6}Li-^{40}K is a prime candidate for these studies. Lithium and potassium are widely used alkali atoms in a variety of applications ranging from Bose-Einstein condensation and fermionic pairing to atom interferometry and precision measurements. They possess easily accessible fermionic and bosonic isotopes and can be conveniently cooled and trapped by laser light. The bosonic isotopes can also be used to study Bose-Fermi mixtures in optical lattices [121, 122]. Moreover, ^{6}Li and ^{40}K are the only stable, fermionic alkali atoms.

To date, all research groups investigating Fermi-Fermi mixtures with two different atomic species chose the mixture ^{6}Li-^{40}K [62, 63, 123–125]. So far, three groups reported on quantum degeneracy of the mixture [61–63]. The interspecies Feshbach resonances are characterized [126–130] and weakly bound Feshbach molecules were studied [63,131]. Furthermore the Innsbruck group studied the hydrodynamic expansion of ^{6}Li and ^{40}K in the strong interaction regime [132], measured the excitation spectrum of ^{40}K impurities resonantly interacting with a Fermi sea of ^{6}Li, where they observed repulsive polarons for strong interactions [133], and recently observed a strong atom-dimer attraction in a mass-imbalanced mixture [134].

To use an ultracold Fermi gas as a model for other physical systems, universality is a prerequisite. In the universal regime, the properties of the gas solely depend on the scattering length and the interparticle separation, and not on microscopic details of the interaction potential. To enter the universal regime a strong Feshbach resonance with a large width is required. To date, the universal regime can be only reached for the single species ^{6}Li [135] and ^{40}K [136]. However, it might be possible to reach the universal regime for the ^{6}Li-^{40}K-mixture, by using the 1.5 Gauss-wide Feshbach resonance at $B_0 \sim 115$ G [128].

1.5 Sub-Doppler laser cooling

The road towards quantum degeneracy in atomic gases usually starts by a laser cooling and trapping phase that should provide a large initial phase space density of the atomic ensemble. This favors a high collision rate for initiating efficient evaporative cooling to quantum degeneracy. Sub-Doppler cooling has proven to be a powerful technique to increase the phase-space density of the atomic sample [137]. However, cooling lithium and potassium using optical transitions is difficult compared to the other alkali-metal atoms. The small separation of the excited-state structure of the D_2 transition, compromises the efficiency of standard sub-Doppler cooling techniques such as polarization gradient cooling [137–139].

The central scientific result of my thesis is the simultaneous sub-Doppler cooling of ^{6}Li and ^{40}K using a bichromatic cooling scheme on the D_1 transition [140, 141]. The D_1 molasses phase not only cools the atoms to deep sub-Doppler temperatures, 44 μK for ^{6}Li and 11 μK for ^{40}K, but preserves the large atom numbers of the magneto optical trap (MOT). In combination with a preceding compressed MOT phase, the atomic density is increased by a factor of five, yielding a phase space density of $\sim 10^{-4}$ for both species. The combined temperature and density improvement after the D_1 molasses is at least a thirty-fold increase in phase space density compared to our MOT. The D_1 cooling scheme is applicable to other alkali atoms [141–145], and enables fast evaporation to quantum degeneracy in optical or magnetic traps. Furthermore, it can be used to directly load atoms in a far detuned optical trap with high efficiency [144, 145], offering a promising route for the all-optical production of alkali degenerate gases.

Another possibility to pre-cool ^{6}Li and ^{40}K is to operate the MOT on a transition with smaller linewidth to reduce the Doppler-temperature. Such transitions exist for ^{6}Li and ^{40}K in the near-UV and blue regions of the spectrum respectively, leading to temperatures near 60 μK [146, 147]. Yet, special optics and a coherent source at 323 nm (405 nm) for ^{6}Li (^{40}K) are needed for this approach. Additionally, at these wavelengthes the available power is still a limiting factor.

1.6 Thesis outline

This thesis presents novel techniques for experimental studies of ultracold quantum gas mixtures of fermionic lithium and potassium and the further construction of our ^{6}Li- ^{40}K experimental apparatus. Our machine is designed to produce a degenerate Fermi-Fermi

mixture with large atom number. Large atom numbers bring several advantages, such as a high Fermi temperature and a large signal-to-noise ratio.
At the beginning of my thesis, a fully functional dual-species MOT existed and produced large samples of ^{6}Li and ^{40}K, with atom numbers on the order of 10^9 for both species, and temperatures of $\sim 1\,\mathrm{mK}$ and $\sim 240\,\mu\mathrm{K}$, respectively. All subsequent steps to reach quantum degeneracy, such as D_1 cooling, magnetic transport, vacuum improvements, and the setup to perform evaporative cooling in a plugged optical quadrupole magnetic trap and a crossed optical dipole trap, had to be developed and have been implemented during my thesis work.
This manuscript is structured such as it follows an atomic gas from its creation to its evaporation to quantum degeneracy. In Chapter 2, we present the experimental setup. Chapter 3 describes home-made, high power all solid state laser sources at 671 nm for laser cooling of lithium. In Chapter 4, we introduce the simultaneous D_1 sub-Doppler laser cooling of ^{6}Li and ^{40}K. Finally, Chapter 5 presents thermalization experiments in the magnetic trap, the magnetic transport from the MOT- to the science chamber, and evaporative cooling to quantum degeneracy.

Chapter 2 – Experimental setup

We present the complete experimental apparatus, focusing on the updates and new parts of the setup. These comprise a new part of the vacuum assembly, including the transport region and the ultra-high vacuum chamber, with a pressure lower than $10^{-11}\,\mathrm{mbar}$ in the science cell, the laser systems and the optical setup for the D_1 sub-Doppler cooling, the modified 2D-Mot for ^{40}K, a new magnetic trap, the optimized magnetic transport, the parts necessary to perform evaporation in an optically plugged magnetic quadrupole trap and in a crossed optical dipole trap as well as a new experimental control.

Chapter 3 – High power 671 nm laser system

We describe the development of our home-made all solid-state laser sources for laser cooling of lithium atoms. The lasers are based on a diode pumped neodymium-doped yttrium orthovanadate (Nd:YVO_4) gain medium, lasing at the fundamental wavelength of 1342 nm. Second harmonic generation is then established using periodically-poled potassium titanyl phosphate (ppKTP) as the nonlinear medium. We present three development stages. The first laser generation already existed when I started my thesis, and emitted up to 670 mW at 671 nm. With the second laser version, we investigated intracavity-frequency doubling and achieved output powers of up to 2.1 W at 671 nm.

The third and latest version comprises a new built up cavity for second harmonic generation and emits up to 5 W at 671 nm. We used this laser for the D_1 sub-Doppler laser cooling of ^{6}Li.

Chapter 4 – D_1 sub-Doppler laser cooling

This chapter presents a new, three-dimensional optical molasses scheme for simultaneous sub-Doppler cooling of fermionic ^{6}Li and ^{40}K. The cooling scheme is suitable for all alkali atoms, operates on the D_1 line and is based on gray optical molasses. We obtain phase-space densities on the order of 10^{-4} for both ^{6}Li and ^{40}K. After recalling the principles of cooling schemes that are useful to understand the mechanism behind the D_1 molasses, we start with a description of the D_1 cooling mechanism, followed by the experimental results for ^{40}K and ^{6}Li in single species and dual-species operation. Moreover, we compare experimental results with semiclassical simulations of the D_1 cooling mechanism. Thereby we investigate the cooling efficiency as a function of the repumping-detuning from the Raman-resonance-condition.

Chapter 5 – Magnetic trapping, transport and evaporation

We start this chapter by recalling the principles of magnetic trapping, before describing thermalization experiments, that unveil the non-ergodicity of a quadrupole magnetic trap. Furthermore, we characterize the magnetic transport from the MOT- to the science chamber and explain how the D_1 molasses phase helped to increase the transport efficiency to 80%. Finally, we present our current evaporative cooling sequence, which we are still optimizing. To achieve high final atom numbers, we first evaporatively cool the atoms in a plugged magnetic quadrupole trap. After this intermediate stage, we load an optical dipole trap, where we continue the evaporation. To date, we are able to create a degenerate spin mixture of ^{40}K in the spin-states $|F = 9/2, m_\mathrm{F} = 9/2\rangle$ and $|F = 9/2, m_\mathrm{F} = 7/2\rangle$, with atom numbers of $\sim 1.2 \times 10^6$ and $\sim 7.1 \times 10^5$, temperatures of 260 nK and 270 nK, and $T/T_\mathrm{F} \sim 0.27$ and $T/T_\mathrm{F} \sim 0.34$, respectively.

2 Experimental setup

In this chapter we describe the different parts of the Fermix machine, focusing on the upgrades and further developments of the experimental setup described in [125,148,149]. Our goal is to produce degenerate mixtures of ultracold fermions of two different atomic species with large atom numbers and high repetition rates of experimental cycles. A dual-species experiment is more complex, than just joining two single-species setups. The requisite of combining certain techniques for the two species and constraints imposed by the dual-species operation, demand for sophisticated strategies to accomplish a high performing system. Our approach yields large atom numbers for both atomic species while minimizing the complexity of the experimental setup.

2.1 Design

To reach quantum degeneracy, the thermal deBroglie wavelength of the atoms must be on the same order of magnitude as the inter-particle distance. Therefore the atoms need to be cooled and tightly confined in a trap. We follow the standard pathway to quantum degeneracy: laser pre-cooling followed by forced evaporative cooling.
A magneto-optical trap (MOT) (Section 2.6) and a gray optical molasses (Chapter 4) serve as pre-cooling stages. To load the MOT we use continuous beams of slow atoms for both atomic species. This has several advantages: First, the MOT can operate in an ultra-high vacuum environment (Section 2.2), in contrast to a MOT loaded from a background vapor. Second, the flux of the atomic beam and hence the MOT loading rate is large compared to pulsed loading with an alkali getter dispenser [150] or ultraviolet light-induced absorption [151, 152]. Furthermore, we use a separate source for each species, namely a Zeeman slower for ^{6}Li (Section 2.4) and a 2D-MOT for ^{40}K (Section 2.5).
After the MOT phase, a three dimensional gray optical molasses phase cools the atoms to sub-Doppler temperatures.
The evaporative cooling efficiency improves with the vacuum quality, because of the longer lifetime of the trapped atoms. Therefore the cloud is magnetically transported [153] to a ultra-high vacuum (UHV) glass cell (Section 5.3). We perform radio-frequency

(RF) evaporative cooling in an optically plugged magnetic quadrupole trap. A magnetic quadrupole trap is advantageous because of the large optical access compared to other magnetic traps. Its large trapping volume and steep confinement yield an efficient cooling procedure. We evaporate ^{40}K in two different spin states while sympathetically cooling ^{6}Li.
The pre-cooled atoms are loaded into an optical dipole trap, where we continue to cool the atoms by means of optical evaporation (Section 5.4).

2.2 Vacuum system

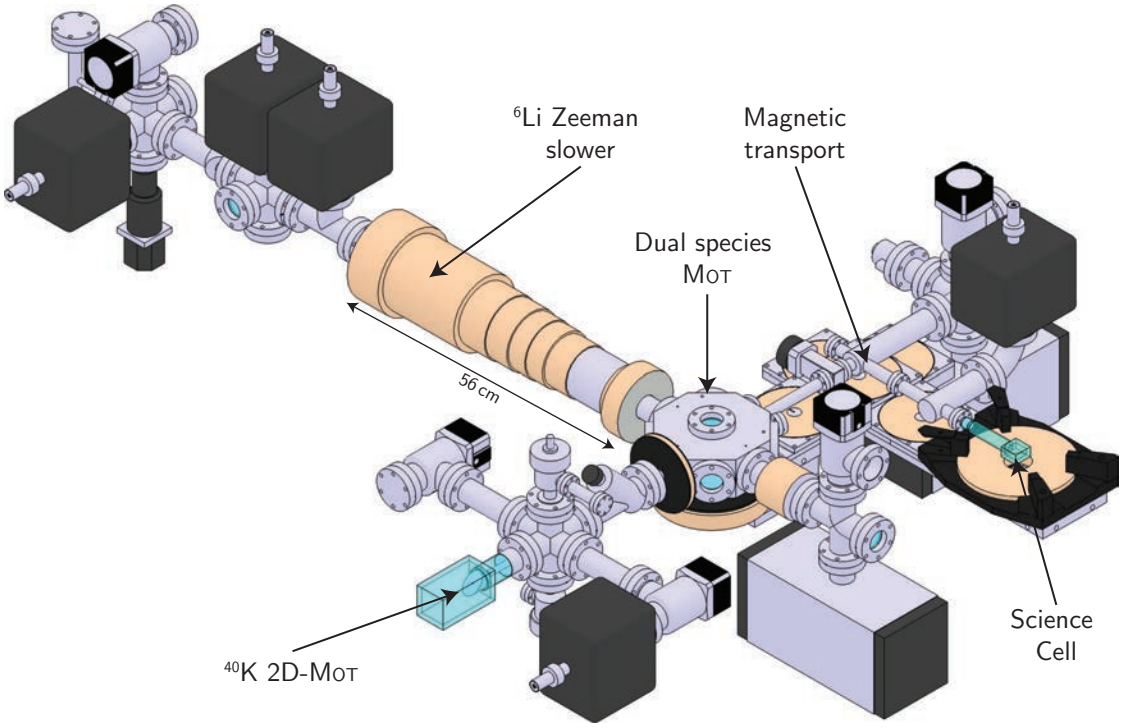

Figure 2.1: Schematics of the vacuum assembly. A 2D-MOT for ^{40}K and a Zeeman slower for ^{6}Li load the dual-species MOT in the octagonal MOT-chamber. A magnetic transport transfers the cloud to a UHV glass cell with improved vacuum quality and large mechanical and optical access.

Our vacuum system is designed to ultimately provide an ultra-high vacuum with large mechanical and optical access to experiment with a large number of ultracold atoms in the quantum degenerate regime. Figure 2.1 shows a CAD model of our vacuum system. The vacuum system consists of two source regions for the ^{40}K 2D-MOT and the

^{6}Li Zeeman slower, the MOT-chamber for the ^{6}Li-^{40}K dual-species MOT, the magnetic transport region, and the science cell, where we will investigate ultracold quantum gases. All-metal UHV vacuum valves can isolate the MOT-chamber from the science cell and the source regions, allowing for separate bake-out and trouble shooting. Differential pumping tubes between the source regions and the MOT-chamber ensure a high vacuum quality in the MOT-chamber. Another differential pumping tube in the first arm of the transport with an inner diameter of 1 cm, allows to further improve the vacuum quality in the transport and science cell. To pump the 2D-MOT and the Zeeman slower region we use one and three 20 l/s ion pumps, respectively. The MOT-chamber is pumped by a 40 l/s ion pump and an active getter tape [1]. For the transport region and the science cell we use a 40 l/s ion pump, located at the elbow of the magnetic transport, a 20 l/s ion pump and active getter tape near the science cell as well as a coating with a thermally activated Titanium-Zirconium-Vanadium alloy in the second transport arm, which acts as an efficient non-evaporable getter. The new transport region consists of CF16 vacuum parts and replaced the setup described in [148]. The new vacuum design increased the 1/e-lifetime of ^{40}K in the science cell from ∼25 s (old setup) to more than 100 s, and solved one of the major problems of the old experimental setup.
The science cell is ideally suited to prepare and investigate an ultracold atomic sample. [2] Its small size provides large mechanical and optical access. Magnetic coils can be placed close to the atoms, enhancing the magnetic confinement and therefore the evaporative cooling efficiency. Moreover, high-resolution imaging, comprising an objective with large numerical aperture, is possible.

2.3 D_2 laser system

Our laser system is designed to provide light for slowing, trapping and probing ^{6}Li and ^{40}K atoms. For this purpose, we address the D_2 line of each atomic species. The only exceptions are the D_1 line sub-Doppler cooling (Section 2.7.2) and the D_1 spin polarization for ^{6}Li (Section 5.1.2). Figure 2.2 shows the level diagrams for the D_2 and D_1 lines of ^{6}Li and ^{40}K. Because the transition wavelengths for ^{6}Li and ^{40}K differ by ~ 100 nm, separate laser systems and optics for ^{6}Li and ^{40}K are necessary. Furthermore, we need several beams with different frequencies and intensities for each atomic species. Figure 2.3 shows the laser schemes of the D_2 lines for ^{6}Li and ^{40}K. We built up the laser

[1] SAES, ref. St 707 strips
[2] The science cell was manufactured by Hellma and is made out of Vycor, a synthetic fused silicon dioxide. The thickness of the glass walls is 4 mm and the cell's inner dimensions are $23 \times 23 \times 10$ mm^3. A glass-to-metal junction connects the glass cell with the magnetic transport vacuum assembly.

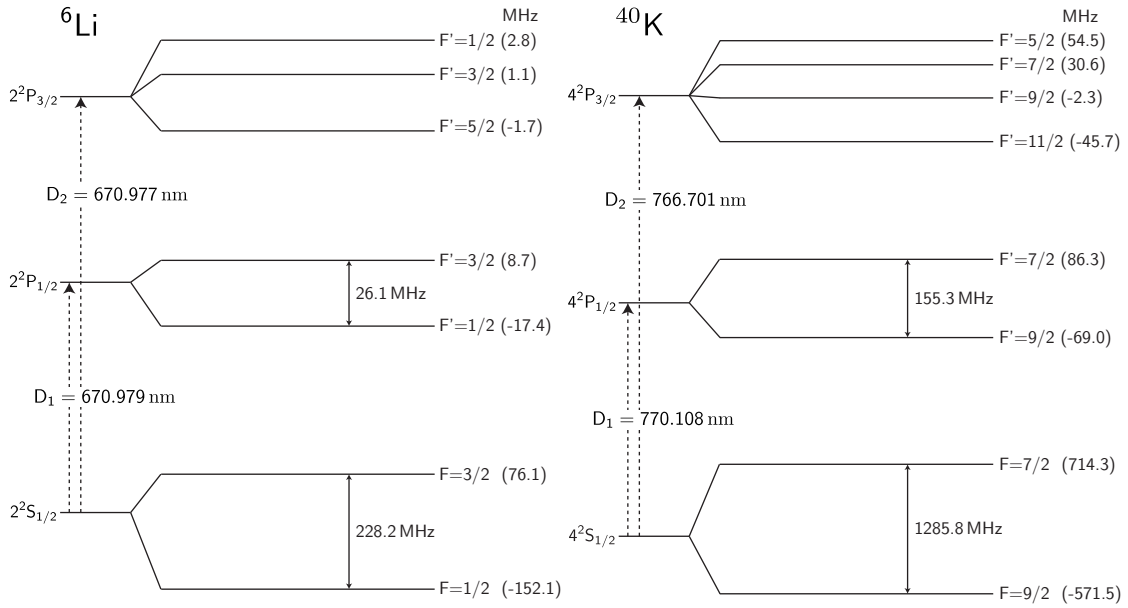

Figure 2.2: Level diagrams for the ^{6}Li and ^{40}K D_2 and D_1 lines with their respective hyperfine structures. The D lines of lithium lie in the red-, those for potassium in the near infrared spectral region. Note the small hyperfine splitting of the $2^2P_{3/2}$ manifold of ^{6}Li.

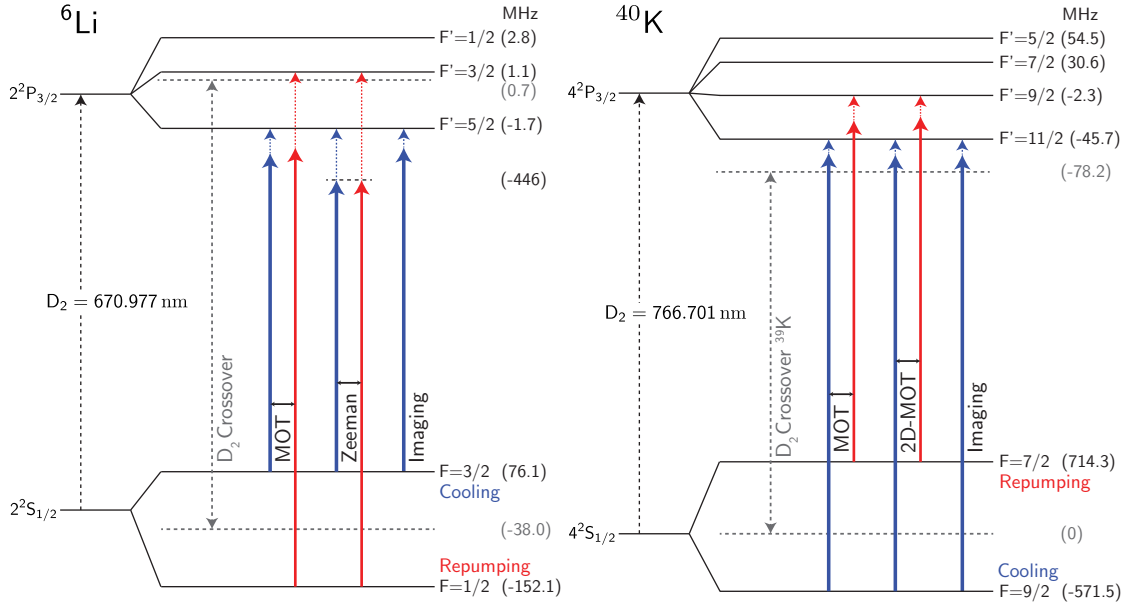

Figure 2.3: D_2 laser scheme for ^{6}Li and ^{40}K. Solid arrows illustrate the frequencies required for the dual-species MOT operation. Dashed arrows indicate the detunings from the corresponding transitions. The diode lasers are locked to the saturated absorption crossover signals $2^2S_{1/2}$ ($|F = 1/2\rangle, |F = 3/2\rangle$) $\rightarrow 2^2P_{3/2}$ of ^{6}Li and $4^2S_{1/2}$ ($|F = 1\rangle, |F = 2\rangle$) $\rightarrow 4^2P_{3/2}$ of ^{39}K.

system for each atomic species on an individual optical table. The generated laser beams are fiber-coupled to the main experimental table.

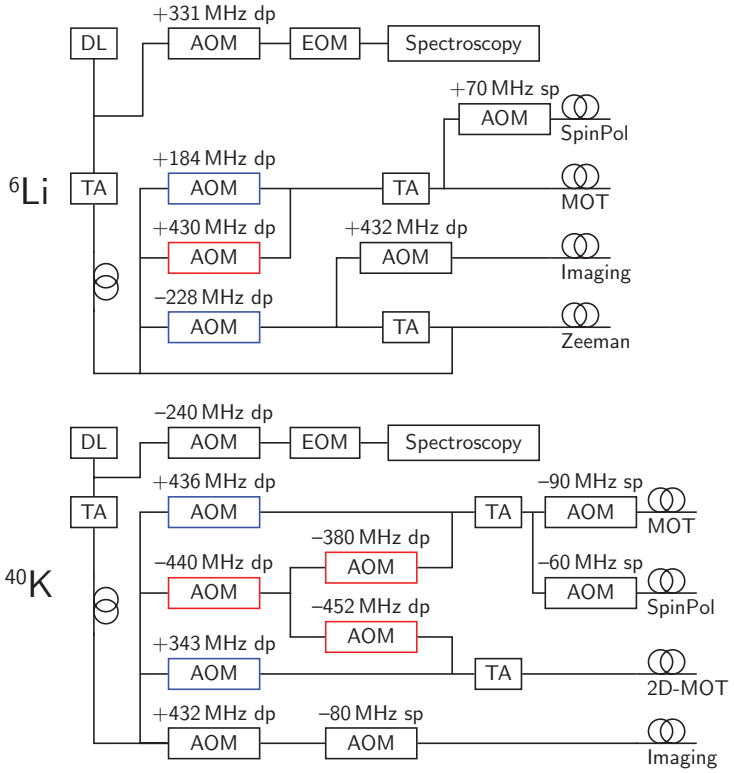

Figure 2.4: D_2 laser systems for ^{6}Li and ^{40}K. The frequencies and amplitudes of the various beams are controlled by AOMs in single pass (sp) or double pass (dp) configuration. Blue and red AOMs create the cooling and repumping frequencies, respectively. The EOMs phase modulate a part of the beam for the diode laser's frequency stabilization. Single mode polarization maintaining fibers spatially filter and shape the beams. The indicated AOM frequencies allow the generation of the beam frequencies required for the dual-species MOT operation (see Fig. 2.3).

The D_2 laser systems for ^{6}Li and ^{40}K share an analogous design. Figure 2.11 shows a simplified scheme for both atomic species. A low power diode laser (DL) [3] serves as light source. The laser frequency is stabilized by means of saturated absorption spectroscopy. The master laser beam is amplified by a tapered amplifier (TA) [4] before it is coupled into a single-mode polarization maintaining optical fiber. The fiber-output is distributed to the laser beams, required for our experiment (Fig. 2.3), by means of a combination of polarizing beam splitters an $\lambda/2$ waveplates. We use Acousto-optical modulators (AOMs)

[3] We use a DL Pro laser from Toptica for ^{6}Li and a home made diode laser described in [148] for ^{40}K.
[4] ^{6}Li TA chip (I-mount): Toptica, ref. TA-0675-0500-1. ^{40}K TA chip (C-mount): Eagleyard, ref. EYP-TPA-0765-01500-3006-CMT03-0000. For both ^{6}Li and ^{40}K, we use home made mounts [148].

to shift the frequencies and regulate the intensities of these beams. The cooling and repumping beams are injected to TAs. The TA outputs are linearly polarized bichromatic beams, containing the cooling- and repumping frequencies. Injecting a TA with two laser beams, differing in frequency, creates sidebands [154]. However, in our case the power losses are negligible ($\sim 5\%$ for ^{6}Li and $\sim 0.2\%$ for ^{40}K) and we do not excite unwanted transitions with one exception: a sideband of the bichromatic Zeeman slower beam would be near-resonant with ^{6}Li atoms trapped in the MOT. Therefore, we only amplify the Zeeman cooling beam and combine the cooling- and repumping beams after the Zeeman TA. Finally, all beams are injected to fibers and transferred to the main experimental table.

2.4 ^{6}Li Zeeman slower

As a source for our ^{6}Li-MOT we use a Zeeman slower [155, 156]. It consists of an oven, creating an thermal atomic beam, a counter-propagating laser beam and an assembly of magnetic field coils. To provide a continuous deceleration, the counter-propagating laser beam has to be close to the atomic resonance during the entire slowing process. Therefore the Zeeman shift, generated by the inhomogeneous magnetic field of the coil assembly, must compensate the changing Doppler shift of the decelerating atoms.

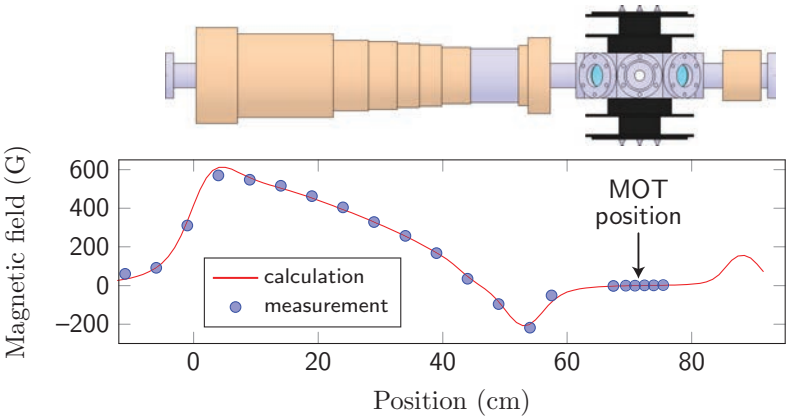

Figure 2.5: ^{6}Li Zeeman slower coil assembly (top) and generated axial magnetic field profile (bottom). The thermal atoms coming from the ^{6}Li-oven enter the coil assembly at the position 0, and a fraction of them is slowed down and finally captured in the ^{6}Li-MOT, which is located at 71.4 cm. A compensation coil placed on the opposite side of the MOT (at 84.1 cm) ensures that the magnetic field at the position of the MOT is zero. The coil assembly extends over 55 cm. (see [148])

We use a sign-changing field Zeeman slower because it has certain advantages compared to a positive-field Zeeman slower. Namely, the maximum magnetic field is smaller, the laser beam is non-resonant with the ^{6}Li-MOT atoms and it has less coil windings close to the MOT, improving the optical access. Yet repumping light is needed in the region where the magnetic field changes sign.

In the following we review the most important parameters and the performance of our Zeeman slower. A detailed characterization can be found in [148]. Figure 2.5 shows the coil assembly and the axial magnetic field profile of the Zeeman slower. The ^{6}Li-MOT is 71.4 cm away from the entry of the slower. A compensation coil at 84.1 cm minimizes the magnetic field at the MOT position. Table 2.1 summarizes the optimal parameters of the ^{6}Li Zeeman slower. We heat the oven to $\sim 500\,^\circ$C, yielding a ^{6}Li-MOT capture rate of $\sim 1.2 \times 10^9$ atoms/s.

^{6}Li Zeeman slower	
P_{fiber} (mW)	50
$\Delta\omega_{\text{slow}}$ (Γ)	-75
$\Delta\omega_{\text{rep}}$ (Γ)	-75
$I_{\text{rep}}/I_{\text{slow}}$	1/8
B_{max} (G)	570

Table 2.1: Optimized values for the parameters of the ^{6}Li Zeeman slower. $\Delta\omega_{\text{slow}}$ and $\Delta\omega_{\text{rep}}$ denote the detuning of the slowing and repumping beams, respectively. The natural linewidth of ^{6}Li is $\Gamma/(2\pi) = 5.87$ MHz. An oven temperature of $\sim 500\,^\circ$C yields a ^{6}Li-MOT capture rate of $\sim 1.2 \times 10^9$ atoms/s.

2.5 ^{40}K 2D-MOT

A two-dimensional magneto-optical trap (2D-MOT) loads the ^{40}K 3D-MOT. A 2D-MOT is a high flux cold atom source, used for rubidium [157–159], cesium [160], potassium [161] and lithium [162]. Although Zeeman slowers can produce higher fluxes, they produce magnetic fields and hot flux in the MOT-chamber. 2D-MOTs are more compact and can be operated at lower temperatures and are thus more economic. This is important for fermionic potassium, because enriched ^{40}K samples are expensive [5]. Furthermore, the 2D-MOT separates ^{40}K from the more abundant ^{39}K, as the atomic beam contains only the cooled ^{40}K atoms, avoiding a significant thermal background.

[5] We paid 4000€ for 100 mg of a 4% enriched sample

2.5.1 Principle of a 2D-MOT

A 2D-MOT transversally confines atoms, captured from a background vapor, and out-couples an atomic beam in the longitudinal direction through a differential pumping tube. The tube also acts as a velocity filter which yields a transversally and longitudinally cold atomic beam arriving in the 3D-MOT chamber. A longitudinal molasses cooling increases the flux of a 2D-MOT [157], because atoms spend more time in the transverse cooling region. In our setup we use a 45°-angled mirror inside the vacuum chamber allowing for two independent, counter propagating, longitudinal molasses beams, labeled long+ and long- in Fig. 2.6. In our new setup, we implement an independent pushing beam that out-couples the atomic beam through a small hole in the center of the 45°-angled mirror.

2.5.2 Experimental setup

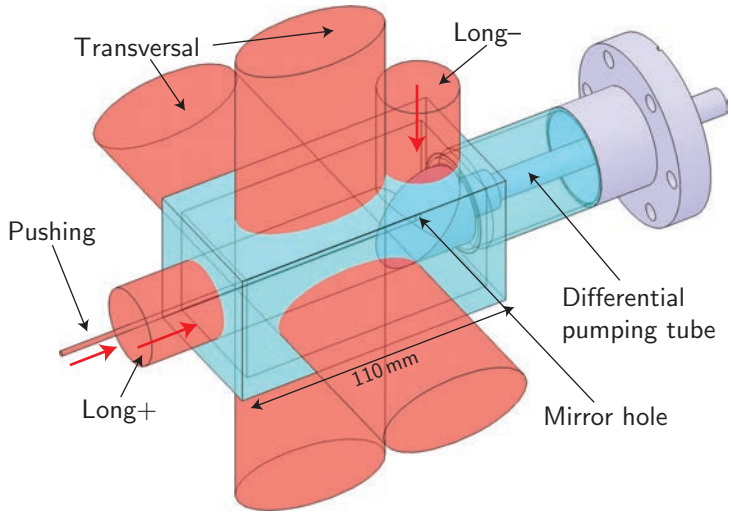

Figure 2.6: Illustration of the ^{40}K 2D-MOT beams. The elliptic beams provide transversal cooling. A mirror is placed inside the vacuum chamber to allow an independent control over the longitudinal molasses beam pair. The pushing beam out-couples the atomic beam through the mirror hole. Optimized beam parameters are summarized in Table 2.2.

The centerpiece of the 2D-MOT vacuum chamber is the glass cell with dimensions $110 \times 55 \times 55\,\mathrm{mm}^3$ shown in Fig. 2.6. The polished stainless steel mirror is attached to the differential pumping tube inside the vacuum. It is inert to potassium vapor and has a reflectivity of 50%. The 2D- and 3D-MOT centers are separated by 55 cm. The pressure ratio between the 2D- and the 3D-MOT chambers is $\sim 10^3$.

Our 4% enriched ^{40}K sample is located close to the glass-to-metal junction of the glass cell (see *Cold point* on page 18). We created a cold point by winding a water cooled tube at this point (see Fig. 2.7). The temperature of the cold point can be controlled to choose a convenient K-pressure in the glass cell. We work at a cold point temperature of $\sim 40\,^{\circ}$C, corresponding to a pressure of $\sim 2 \times 10^{-7}$ mbar and a partial pressure of $\sim 1 \times 10^{-8}$ mbar for ^{40}K.

We use a racetrack coil geometry to create a 2D quadrupole magnetic field with cylindrical symmetry and a horizontal line of zero magnetic field. The optimal magnetic field gradients are $\partial_x B = \partial_y B = 11\,\mathrm{G/cm}$.

The 2D-MOT bichromatic laser beam has a total power of $P_{\mathrm{fiber}} = 350\,\mathrm{mW}$ at the fiber output. The cooling frequency is red detuned by $\sim 3.5\,\Gamma$ from the $|F = 9/2\rangle \rightarrow |F' = 11/2\rangle$ transition whereas the repumping frequency is detuned by $\sim 2.5\,\Gamma$ from the $|F = 7/2\rangle \rightarrow |F' = 9/2\rangle$ transition (see Fig. 2.3). The beam is split into five beams needed for the transverse and longitudinal 2D-MOT beams (see Fig. 2.6). The beams are expanded by spherical and/or cylindrical telescopes and circularly polarized. The transverse beams have an elliptical cross section with $1/e^2$-diameters of 27.5 mm and 55 mm. They are retro-reflected by right-angled prisms, preserving the beam helicity. The longitudinal cooling beams have a $1/e^2$-diameter of 27.5 mm, the $1/e^2$-diameter of the pushing beam is 3.8 mm. 87% of the fiber output power is used for the transverse beams, 11% for the longitudinal cooling beams and 2% for the pushing beam.
Table 2.2 summarizes the optimal values of the important 2D-MOT parameters. With these parameters, we obtain a ^{40}K-MOT loading rate of $\sim 3 \times 10^8$ atoms/s.

^{40}K 2D-MOT	
P_{fiber} (mW)	350
$\Delta\omega_{\mathrm{cool}}$ (Γ)	-3.5
$\Delta\omega_{\mathrm{rep}}$ (Γ)	-2.5
$I_{\mathrm{rep}}/I_{\mathrm{cool}}$	0.5
$I_{\mathrm{trans}+}/I_{\mathrm{trans}-}$	2.4
P_{push} (mW)	8.6
$\partial_x B$, $\partial_y B$ (G/cm)	11
K vapor Pressure (mbar)	2.3×10^{-7}

Table 2.2: Optimal values of the ^{40}K 2D-MOT parameters, yielding a ^{40}K MOT loading rate of 3×10^8 atoms/s. The definition of the symbols is given in the text. The natural linewidth of ^{40}K is $\Gamma/(2\pi) = 6.04\,\mathrm{MHz}$.

2.5.3 Characterization of the 2D-MOT upgrade

The performance of the 2D-MOT is characterised by the loading rate of the ^{40}K-MOT. Its dependence on several 2D-MOT parameters [6] has been already studied in the thesis of Armin Ridinger [148]. Here we focus on the upgrades of the 2D-MOT setup, namely, a new strategy to control the pressure in the 2D-MOT glass cell (see *Cold point* on page 18), and the integration of an independent pushing beam (see *Independent pushing beam* on page 19).

Cold point

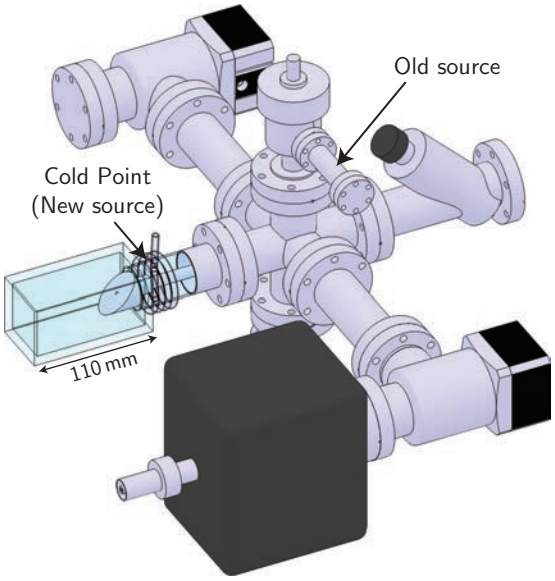

Figure 2.7: The ^{40}K 2D-MOT vacuum system. The cold point is our new potassium source because the old source no longer contains potassium. We heat the old source region to $\sim 120\,^{\circ}$C, the glass cell to $\sim 45\,^{\circ}$C and all intermediate parts to $\sim 70\,^{\circ}$C to establish a temperature gradient. The cold point temperature can be varied with a chiller to control the 2D-MOT pressure (see Fig. 2.8).

The vacuum assembly of the 2D-MOT is shown in Fig. 2.7. Originally our potassium source has been located 20 cm from the glass cell in a CF16 bellow. Here a small ampule with isotopically enriched ^{40}K has been broken under vacuum. A malfunctioning of the heating close to the ion pump caused the potassium atoms to condense in this region and depleted the old source. Therefore, we decided to create a cold point near the glass cell

[6] e.g. the total cooling light intensity and frequency, intensity ratios, the vapor pressure in the 2D-MOT cell, etc.

to serve as a new source. To control the cold point temperature a water cooled tube is enclosing the glass tube of the 2D-MOT cell (see Fig. 2.7). A chiller stabilizes the water temperature. In the current setup the old source region is heated to $\sim 120\,^{\circ}$C, the glass cell to $\sim 45\,^{\circ}$C and all other parts, except for the cold point, to $\sim 70\,^{\circ}$C. In operating mode the cold point temperature is set to $\sim 40\,^{\circ}$C. Otherwise, it is cooled to $\sim 15\,^{\circ}$C to recollect potassium atoms.

We determine the vapor pressure of potassium by measuring the absorption profile of a low intensity probe beam passing through the 2D-MOT cell with a path length of 10.5 cm.[7]. Figure 2.8 shows how the 3D-MOT loading rate and the 2D-MOT pressure rise with the cold point temperature. A cold point temperature of $\sim 40\,^{\circ}$C yields a potassium pressure of 2×10^{-7} mbar, implying a partial pressure of $\sim 1 \times 10^{-8}$ mbar for ^{40}K.

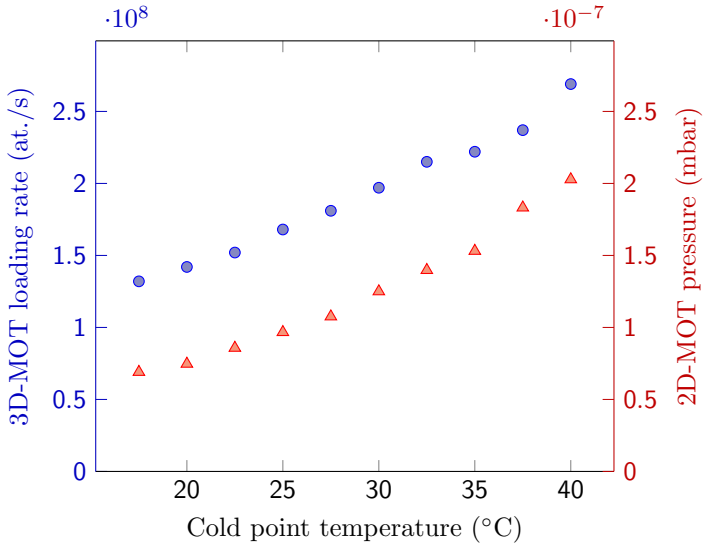

Figure 2.8: 3D-MOT loading rate (circles) and 2D-MOT pressure (triangles) as functions of the cold point temperature. The pressure is deduced from the maximum absorption of a weak probe beam passing through the 2D-MOT cell.

Independent pushing beam

To increase the 2D-MOT performance we added a pushing beam matching the size of the mirror hole (see Fig. 2.6). The new beam allows for independent optimization of the atomic beam outcoupling and the longitudinal 2D-MOT molasses. Therefore, the power of the longitudinal molasses can be reduced from ~ 90 mW to ~ 40 mW, yielding higher

[7] Details are explained in Appendix A of [148]

powers for the transversal beams. Compared to the old setup we were able to increase the 3D-MOT loading rate by a factor of two.[8] We found the best performance for a circular polarized pushing beam and a longitudinal molasses in a σ^+–σ^- configuration.[9] Figure 2.9 shows the 3D-MOT loading rate as a function of the pushing beam power. For this measurement, the power of the other 2D-MOT beams was kept constant. We find an optimum loading rate of $\sim 3 \times 10^8$ at./s for $P_{\text{push}} = 8.6\,\text{mW}$. The $1/e^2$-diameter of the pushing beam is 3.8 mm.

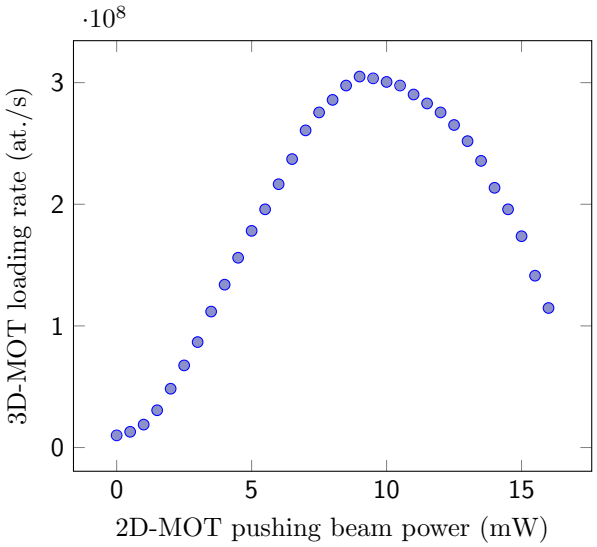

Figure 2.9: 3D-MOT loading rate as a function of the 2D-MOT pushing beam power. We find an optimum loading rate of $\sim 3\times10^8$ at./s for $P_{\text{push}} = 8.6\,\text{mW}$. The $1/e^2$-diameter of the pushing beam is 3.8 mm.

2.6 ^{6}Li-^{40}K dual-species MOT

In this section we present the implementation and performance of our ^{6}Li-^{40}K dual-species MOT. Combining three orthogonal pairs of counter-propagating red-detuned laser beams with a magnetic quadrupole field cools and magneto-optically confines atoms around the field zero [156]. Hence the name magneto-optical trap. We use bichromatic MOT-beams for both ^{6}Li and ^{40}K with a cooling and repumping frequency. The latter is needed for alkali atoms in general and ensures that the atoms stay in the almost cycling cooling transition. For ^{6}Li the repumping frequency even contributes to the cooling.

[8] Here, "old setup" refers to the optimized 2D-MOT setup without independent pushing beam, the day we implemented the new setup comprising the independent pushing beam.
[9] The old setup used a lin⊥lin configuration

Because of the very small hyperfine structure of the excited-state, the ^{6}Li atoms very likely leave the cooling transition.
For a dual-species MOT it is important to minimize the light-induced interspecies collisions to avoid losses. We are able to limit these losses to less than 10%, by using low magnetic field gradients and low intensity repumping light for both atomic species [125].

2.6.1 Experimental setup

The two bichromatic laser beams for the dual-species MOT, one for each species, are fiber-coupled to the main experimental table. The optical scheme, creating the MOT beams, is presented in Section 2.7.3 and Fig. 2.12. The $1/e^2$-diameter of the MOT-beams is 22 mm.
The total power of the bichromatic fiber output for the ^{40}K-MOT beam is $P_{\text{fiber,K}} = 190\,\text{mW}$. The cooling frequency is red-detuned by $\sim 3\,\Gamma$ from the $4^2S_{1/2}\,|F = 9/2\rangle \rightarrow 4^2P_{3/2}\,|F' = 11/2\rangle$ transition whereas the repumping frequency is detuned by $\sim 5\,\Gamma$ from the $4^2S_{1/2}\,|F = 7/2\rangle \rightarrow 4^2P_{3/2}\,|F' = 9/2\rangle$ transition (see Fig. 2.3). The cooling/repumping ratio is ~ 20.
The fiber output power for the ^{6}Li-MOT is $P_{\text{fiber,Li}} = 70\,\text{mW}$. The frequencies are red-detuned by $\sim 5\,\Gamma$ from the $2^2S_{1/2}\,|F = 3/2\rangle \rightarrow 2^2P_{3/2}\,|F' = 5/2\rangle$ cooling and $\sim 3\,\Gamma$ from the $2^2S_{1/2}\,|F = 1/2\rangle \rightarrow 2^2P_{3/2}\,|F' = 3/2\rangle$ repumping transition (see Fig. 2.3). The cooling/repumping ratio is ~ 5.
A pair of water cooled coils in anti-Helmholtz configuration creates the MOT magnetic field. The coils are separated by ∼13 cm and create an axial magnetic field gradient of 0.94 G/(cm A). We operate the dual-species MOT at $\partial_z B = 8\,\text{G/cm}$, yielding an optimal atom number for the ^{40}K-MOT.
Table 2.3 summarizes the optimal values of the ^{6}Li-^{40}K dual-species MOT parameters. In dual-species operation we obtain $\sim 3.2 \times 10^9$ ^{40}K atoms at $\sim 240\,\mu$K and $\sim 2 \times 10^9$ ^{6}Li atoms at $\sim 1\,$mK yielding phase space densities on the order of 10^{-7} for both atomic species.

	^{40}K-MOT	^{6}Li-MOT
P_{fiber} (mW)	190	70
$\Delta\omega_{\text{cool}}$ (Γ)	-3	-5
$\Delta\omega_{\text{rep}}$ (Γ)	-5	-3
I_{cool} per beam (I_{sat})	11	2.5
$I_{\text{cool}}/I_{\text{rep}}$	20	5
$\partial_z B$ (G/cm)	8	8
N_{single} ($\times 10^9$)	3.5	2.1
N_{dual} ($\times 10^9$)	3.2	2
T (μK)	240	1000
n_{c} ($\times 10^{10}\,\text{cm}^{-3}$)	7	2.6
ϕ [a] ($\times 10^{-7}$)	2	3
D_2 line properties	^{40}K	^{6}Li
$\Gamma/(2\pi)$ (MHz)	6.04	5.87
I_{sat} (mW/cm^2)	1.75	2.54

Table 2.3: Optimal values of the ^{6}Li-^{40}K dual-species MOT parameters. n_{c} is the peak atomic density and T the temperature of the atomic clouds. $\phi = n\lambda_{\text{B}}^3$ is the peak phase-space density, where $\lambda_{\text{B}} = \sqrt{2\pi\hbar/mk_BT}$ is the thermal de Broglie wavelength.

[a] The given phase-space density does not take into account the different internal states

2.7 Optical molasses – D_1 sub-Doppler cooling

To increase the phase-space density of the ^{6}Li-^{40}K mixture we apply an optical molasses phase in combination with a preceding compressed MOT phase (CMOT). The CMOT phase increases the densities of the atomic samples, before the D_1 molasses phase cools them to deep sub-Doppler temperatures. Here we describe the implementation of the ^{6}Li-^{40}K dual-species molasses. Its characterization is presented in Chapter 4.

2.7.1 Compressed MOT

To increase the density of the MOT we apply a compressed MOT phase. In 5 ms the magnetic gradient is linearly ramped from 8 G/cm to 45 G/cm. At the same time the frequencies of the cooling and repumping light are brought closer to resonance while the beam intensities are reduced. For ^{40}K the density increases from 7×10^{10} at./cm^3 to 3.7×10^{11} at./cm^3 while the temperature increases from 240 μK to 2 mK. The ^{6}Li density increases from 2.6×10^{10} at./cm^3 to 1.8×10^{11} at./cm^3 and the temperature decreases from 1 mK to 800 μK.

2.7.2 D_1 laser system

Figure 2.10 shows the level schemes of the D_1 lines for ^{6}Li and ^{40}K as well as the molasses beams. The D_1 sub-Doppler cooling scheme requires two more separate laser systems, because the AOMs of the D_2 systems can only be tuned by some tens of MHz (see Fig. 2.11), while the frequency separations of the D_1 and D_2 lines for ^{6}Li and ^{40}K, are $\sim 10\,$Ghz and $\sim 11\,$Thz, respectively (see Fig. 2.2).

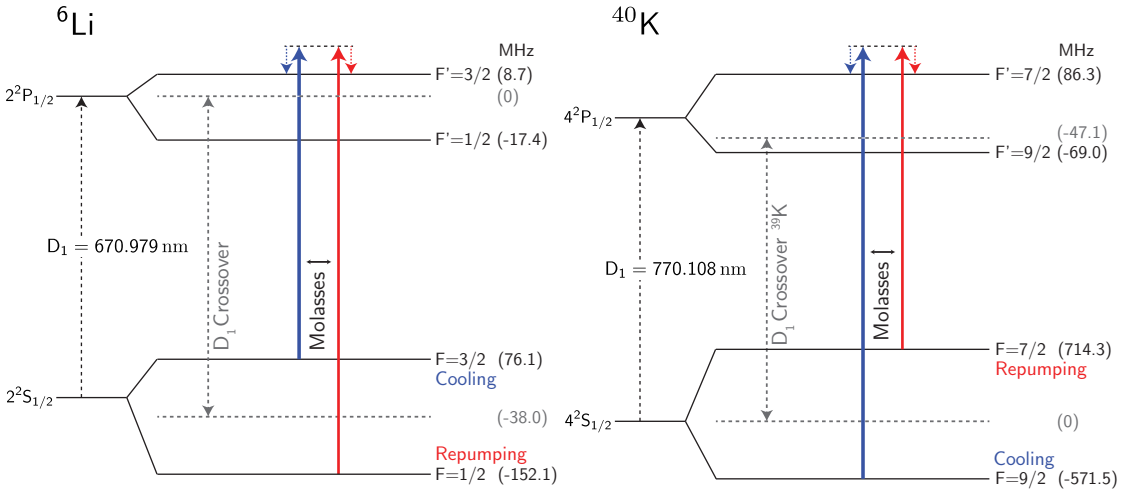

Figure 2.10: Level schemes for the ^{6}Li and ^{40}K D_1 lines. Solid and dashed arrows depict the frequencies and detunings required for the sub-Doppler cooling, respectively. The lasers are locked to the saturated absorption crossover signals $2^2S_{1/2}$ $(\left|F=1/2\right\rangle, \left|F=3/2\right\rangle) \rightarrow 2^2P_{1/2}$ of ^{6}Li and $4^2S_{1/2}$ $(|F=1\rangle, |F=2\rangle) \rightarrow 4^2P_{1/2}\left|F'=2\right\rangle$ of ^{39}K. The D_1 sub-Doppler cooling is described in Chapter 4.

The D_1 laser systems for ^{6}Li and ^{40}K are shown in Fig. 2.11). In both setups the overall detuning can be changed with the double-pass AOM in the saturated absorption spectroscopy path. For the ^{40}K D_1 system, we use an electro-optic modulator (EOM) to create the repumping frequency. Sending a beam through an EOM creates two small sidebands, separated from the original carrier frequency by the modulation frequency of the EOM. The sideband with the lower frequency constitutes the repumping light. The power lost to the second sideband is negligible because the D_1 cooling scheme works with a very low repumping power. Furthermore, this sideband does not excite unwanted transitions.

As a source for the ^{6}Li D_1 cooling light, we use a home-made all solid-state laser (SSL), we present in Section 3.4. The high power output of 5 W allows us to use a flexible setup for the characterization of the D_1 molasses. In our setup we can scan the power of

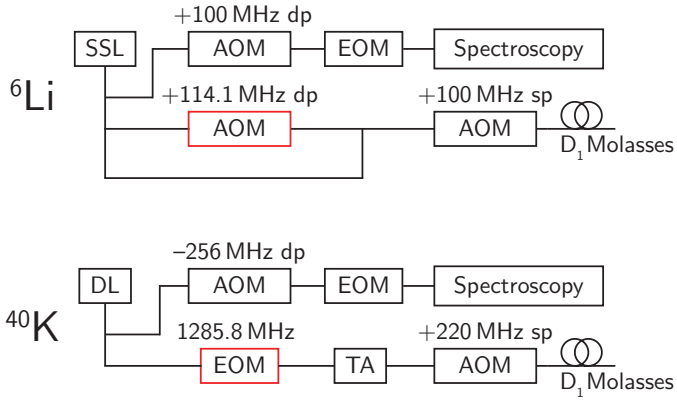

Figure 2.11: Laser systems of the D_1 molasses cooling schemes for ^{6}Li and ^{40}K. The frequencies and amplitudes of the various beams are controlled by AOMs in single pass (sp) or double pass (dp) configuration. An EOM creates the repumping frequency in the ^{40}K setup. The EOMs in the spectroscopy phase modulate a part of the beam for the laser's frequency stabilization. Single mode polarization maintaining fibers couple the beams to the experimental setup. The indicated AOM frequencies allow the generation of the beam frequencies required for the molasses cooling (see Fig. 2.3).

the repumping light independently. Furthermore, we can scan the repumping frequency without changing the repumping power. However, to operate a ^{6}Li molasses, it is sufficient to use a master oscillator power amplifier (MOPA) setup, comprising a master diode and a TA, and to create the repumping frequency with an EOM (like we did for ^{40}K). The available power after an optical fiber, $P_{\mathrm{MOPA,fiber}} \sim 200\,\mathrm{mW}$, yields reasonable transfer efficiencies from the CMOT to the D_1 molasses, when an appropriate beam diameter of the molasses beams is chosen (see Chapter 4).

2.7.3 Implementation of the D_1 molasses

We implement the D_1 molasses by merging the molasses light and the MOT light. The bichromatic fiber outputs for the ^{6}Li-^{40}K-molasses have a total power of $P_{\mathrm{fiber,Li}} = 300\,\mathrm{mW}$ and $P_{\mathrm{fiber,K}} = 230\,\mathrm{mW}$, respectively. Figure 2.12 shows how the two bichromatic molasses beams for ^{6}Li and ^{40}K, emerging from the optical fibers labeled $D_{1,\mathrm{Li}}$ and $D_{1,\mathrm{K}}$, are superimposed with the MOT light with D-shaped mirrors (M_{D}).

A dichroic mirror (M_{dichroic}) combines the lithium and potassium light. The beam, containing all MOT- and molasses frequencies, is expanded with a 10:1 telescope and distributed to the three pairs of σ^+–σ^- counter-propagating beams of the 3D-MOT and the D_1 molasses. The $1/e^2$-diameters of the molasses beams after expansion are

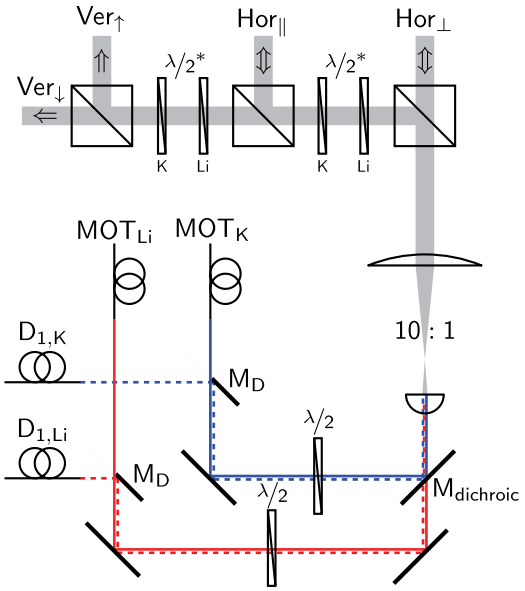

Figure 2.12: Optical scheme of the MOT and the D_1-molasses. The MOT light and the D_1 cooling light are superposed using a D-shaped mirror (M_D) for both atomic species. Afterwards a dichroic mirror ($M_{dichroic}$) combines the lithium- and potassium light, which is subsequently expanded and distributed to the three perpendicular axes of the 3D-MOT.

$\sim 17.1\,\mathrm{mm}$ for ^{6}Li and $\sim 17.8\,\mathrm{mm}$ for ^{40}K. The $1/e^2$-diameter of the 3D-MOT is $\sim 22\,\mathrm{mm}$ for both ^{6}Li and ^{40}K.

The two horizontal axes are retroreflected, the vertical axis consists of two independent beams. The $\lambda/2$ plates of order four for lithium ($\lambda/2^*_{\mathrm{Li}}$) and potassium ($\lambda/2^*_{\mathrm{K}}$) allow for independent control of the ^{6}Li and ^{40}K MOT power distribution. To a very good approximation each of these wave plates can turn the polarization direction for one wavelength without affecting the polarization of the other one since $4.5 \times 767 \approx 5 \times 671$ and $4.5 \times 671 \approx 4 \times 767$. We use first order $\lambda/4$ waveplates for 767 nm to circularly polarize the MOT beams. The waveplates perform adequately for 671 nm.

2.8 Magnetic trapping

To further increase the phase space density, the atomic sample, captured and cooled by the MOT and the D_1 molasses, must be evaporatively cooled (see Section 5.4). Therefore, the atoms need to be transferred to a non-dissipative trap. Conventional conservative traps used for evaporative cooling are magnetic traps and optical dipole traps (ODTs). The latter have a limited trapping volume and therefore a small transfer efficiency for

atoms from a MOT. Therefore we decided to start the evaporation in a magnetic trap before ultimately loading the atoms into an ODT (see Section 5.4).

In the following we summarize the different stages of magnetic trapping in our experimental setup and characterize the experimental tools, used in this stages. For a detailed discussion of magnetic trapping we refer the reader to Chapter 5.

2.8.1 Transfer to the magnetic quadrupole trap

After the optical cooling phase, the atoms are transferred to a magnetic quadrupole trap. For an efficient transfer, the atoms need to be optically pumped to magnetically trappable states (see Section 5.1.2). Therefore, in presence of a small bias field, a short spin polarization light pulse is applied before the magnetic trap is switched on. The magnetic trapping field is created by the same coil pair as for the MOT. It takes $\sim$3 ms to ramp up the magnetic gradient from zero to 45 G/cm. From there, the gradient is linearly ramped to its final value of 145 G/cm in 500 ms.

2.9 Magnetic transport

The lifetime of the atoms, prepared in the dual species MOT, and the optical access can be increased by transferring the trapped cloud to the UHV science cell. We use a magnetic transport technique with a 90° corner [153], yielding additional optical access on the transport axis.

The magnetic transport is realized with 14 overlapping coil pairs and a pushing coil. Time varying currents continuously move the magnetic trap center from the MOT chamber to the science cell over a total distance of 64 cm. A detailed discussion of the magnetic transport is presented in Section 5.3.

2.10 Optically plugged magnetic quadrupole trap

In the science cell, we perform RF evaporative cooling in an optically plugged magnetic quadrupole trap. The optical plug avoids atom loss caused by Majorana spin-flips by repelling the atoms from the trap center. The steep, linear confinement of the quadrupole trap leads to high elastic collision rates, enabling an efficient evaporative cooling.

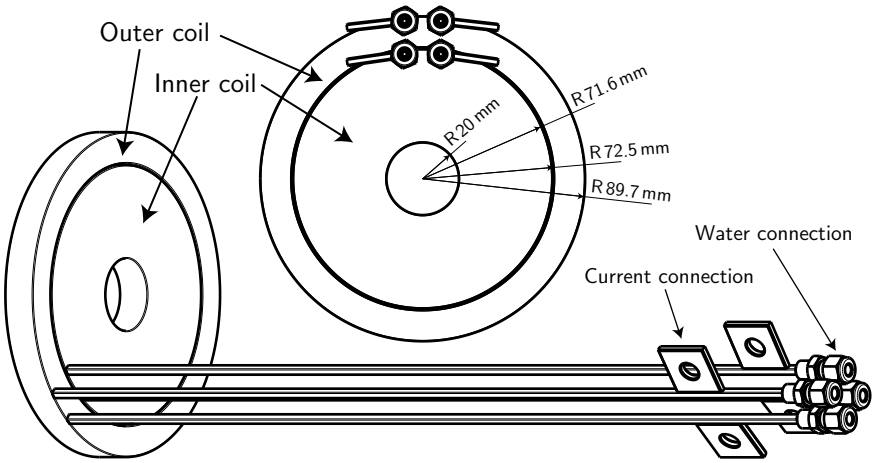

Figure 2.13: Technical drawing of the quadrupole (inner) and Feshbach (outer) coils. The inner coils are used for the optically plugged magnetic trap. They are separated by 35 mm and create an axial magnetic field gradient of 2.51 G/(cm A)

2.10.1 Coils

The magnetic trap in the science cell is formed by a custom made coil pair [10]. It consists of two coil pairs, the inner and the outer one (see Fig. 2.13). During the transport both coil pairs are operated in anti-Helmholtz operation. When the atoms arrive in the glass cell the current of the outer coil pair is ramped to zero and the inner coil pair forms the magnetic trap. Both inner and outer coils are made of 4 mm thick copper wire with squared cross section. A circular hole whit 2.5 mm diameter allows for efficient water cooling.

The inner coils have 4 layers with 12 turns per layer with an inner and outer coil diameter of 40 mm and 72 mm, respectively. They are separated by 35 mm and create an axial magnetic field gradient of 2.5 G/(cm A).

The outer coils have 4×4 turns and an inner and outer coil diameter of 73 mm and 90 mm, respectively. In transport configuration they create an axial magnetic field gradient of 0.24 G/(cm A). In Helmholtz configuration they produce a field of 2.2 G/A at the center of the coil pair with a curvature of -0.027 G/cm^2 in z-direction.

The coils are placed inside the transport coil assembly with a stable mount (see Fig. 5.7). The mount is made of a fiber-reinforced plastic material [11], ensuring high stability and avoiding Eddy currents.

[10] Manufactured by the company Oswald
[11] Faigle, ref. PAS-80 GF30

IGBTs allow for fast switching of the currents. A varistor in parallel to its junction protects the IGBT from induction currents. The IGBT's computer controls are galvanically isolated by opto-couplers.

2.10.2 Optical plug

To prevent atoms from undergoing Majorana spin-flips in the quadrupole trap, a far blue-detuned laser beam is used to repel the atoms from the trap center. This can be essential for an efficient evaporative cooling, especially at low temperature. The first Sodium Bose-Einstein condensate was realized in such an optically plugged magnetic trap [2]. Majorana losses are discussed in Section 5.1.1.

The source for the plug beam is an intracavity-doubled Nd:YVO_4 single mode laser [12], with a wavelength of 532 nm and an output power of 12 W, blue detuned from the D-line transitions of both ^{6}Li and ^{40}K. The plug beam has a power of 7 W and is focused to the magnetic trap center, along the weak axis (x-direction) of the magnetic trap (see Fig. 2.15). Its waist at the focus is $\sim 20\,\mu$m. The resulting barrier has a hight of $\sim 800\,\mu$K for both ^{6}Li and ^{40}K.

A 110 MHz-AOM [13] is employed to switch the plug beam. The amplified [14] output of a voltage-controlled oscillator (VCO) drives the AOM. We monitor the position of the plug beam, by focusing leaking light from a dichroic mirror on a quadrant photodiode [15], and can be adjusted with a motor controlled mirror mount [16] (see Fig. 2.15). An algorithm in our control sequence allows to automatically center the beam on the quadrant photodiode. The computerized alignment ensures a high stability of the setup and compensates for position drifts caused by temperature fluctuations.

2.10.3 RF evaporative cooling

The suppression of s-wave collisions make the evaporative cooling of fermions more difficult than for bosons. Furthermore, the angular momentum barrier suppresses p-wave collisions at low temperatures (typically below $T \sim 6$ mK for ^{6}Li and $T \sim 50\,\mu$K for ^{40}K [7, 163]). Therefore, high elastic collision rates at low temperature are only possible between two different species or two different internal states.

[12] Coherent, ref. Verdi V12
[13] AA optoelectronic, ref. MCQ110-A2 VIS
[14] We use a 5 W high power amplifier (Minicircuits, ref. ZHL-5W-1)
[15] Newport, ref. 2901
[16] Agilis, ref. AG-M100N

^{6}Li-^{40}K collisions are less efficient because of the mass difference [17] and the small cross section. Collisions occur in the triplet channel and have a s-wave scattering length of $a = 64.41\,a_0$ [127], yielding a collision cross section of $\sigma_{\mathrm{LiK}} = 1.5 \times 10^{-10}\,\mathrm{m}^2$.
In a magnetic trap only the stretched state of ^{6}Li is stable because spin relaxation between two different trappable spin states can occur [164]. However, spin relaxation is suppressed for ^{40}K due to the inverted hyperfine structure [4]. The s-wave scattering length between the spin states $|F, m_{\mathrm{F}}\rangle = |9/2, 9/2\rangle$ and $|9/2, 7/2\rangle$ is $a \sim 170\,a_0$ [165]. The corresponding collision cross section $\sigma_{\mathrm{KK}} = 1 \times 10^{-9}\,\mathrm{m}^2$ is an order of magnitude larger than σ_{LiK}.
Therefore we follow the approach demonstrated in [124], and evaporate a ^{40}K spin mixture while sympathetically cooling a small cloud of ^{6}Li.
The principle of evaporative cooling is explained in Section 5.4.1. In the following we present the tools, used in our experiment, to perform evaporation.

RF source

The radio frequency for the RF evaporative cooling of ^{40}K, is generated by an analog signal generator [18], connected to our experimental control (see Section 2.13.3). The RF signal can be fast switched [19] and is amplified by a 30 W high-power amplifier [20]. To protect the output of the amplifier, a circulator [21] interconnects the amplifier and the antenna through its input and transmission port. The reflection port of the circulator connects to a high power -40 dB attenuator [22] and a 50 Ω termination [23].
For the RF evaporation of the ^{40}K spin mixture, we address the transitions $|9/2, 9/2\rangle \rightarrow |7/2, 7/2\rangle$ and $|9/2, 7/2\rangle \rightarrow |7/2, 7/2\rangle$ to flip the atoms to untrapped states (see Section 5.1). In a magnetic quadrupole trap, which is a linear trap (see Eq. (5.4)), the frequency of the RF knife for ^{40}K increases for decreasing energy cut values (see Fig. 5.1). We perform the RF evaporation at a magnetic gradient of $B'_{\mathrm{z}} = 280\,\mathrm{G/cm}$. Therefore, the frequencies, required for the ^{40}K RF evaporation, range from $\sim 1.1\,\mathrm{GHz}$, corresponding to a trap depth of some millikelvin, to 1.285 GHz, the hyperfine splitting of the ^{40}K ground states at zero field (see Fig. 2.2).
An antenna converts electric signals to electromagnetic radiation. The RF output power of the antenna strongly depends on the frequency of the electric input signal. Therefore,

[17] The different mass increases the thermalization time by a factor of two [124]
[18] Agilent, ref. N5161A MXG ATE
[19] Minicircuits, ref. ZASW-2-50DR+
[20] Minicircuits, ref. ZHL-30W-252+
[21] Raditek, ref. RADC-800-2000M-S23-10-100WR-b
[22] Minicircuits, ref. BW-40N100W+
[23] Minicircuits, ref. KARN-50+

the transmission resonance of the ^{40}K RF antenna should coincide with the frequency range from 1.1 GHz to 1.285 GHz. We use a $\lambda/2$ single-loop antenna [24], with a diameter of ∼2 cm. To reduce the losses induced by the skin effect [25] and the proximity effect [26], we make use of a Litz wire, consisting of multiple strands insulated electrically from each other. To tune the transmission resonance of the antenna, we apply the stub technique [166]. Here, a BNC cable with a loose end, integrated to the RF circuit with a T-connector, servers as stub. The length of the BNC cable is adjusted, such that it changes the impedance of the circuit an hence the transmission resonance to the target value. Our optimized antenna shows a high and homogeneous transmission in the frequency range from 1.1 GHz to 1.285 GHz.

2.11 Optical dipole trap

In our setup, the optically plugged magnetic quadrupole trap serves to pre-cool the atoms to achieve an efficient transfer into the optical dipole trap (ODT). An ODT has the advantage, that the magnetic field is a free parameter, and can be used to tune the collision cross section of the gas by means of Feshbach resonances [24]. Our ODT is a focused high power laser beam, operating at a wavelength of 1064 nm. When an atom interacts with a red detuned light field, the induced negative light shifts of the atomic levels depend on the light intensity [167]. A gradient of these light shifts induces a dipole force. The atoms are attracted to the region of highest intensity. Therefore, the atoms are trapped at the focus of the optical dipole beam.
The source of the optical dipole beam is a high power, ultra-narrow linewidth laser [27] with an output power of 25 W at 1064 nm. We use a 80 MHz AOM [28] to control the beam power of the -1st order beam, that is used for the first ODT (ODT_1). The zero order beam is used for a second ODT (ODT_2), which will be discussed later. The AOM is designed for high power applications. The quartz crystal has an active aperture of 2.5×2.5 mm and withstands a power density of 500 MW/cm^2. The ODT_1 beam is fiber-coupled to the optical table, placed around the science cell, to increase the pointing stability and to improve the beam quality. We use a single-mode polarization-maintaining high-power

[24] The diameter of the circular loop is half the wavelength of the RF output. $\omega_{RF-Evap} \sim 2\pi \times 1.14$ GHz $\Rightarrow f_{antenna} \sim 7.2$ GHz $\Rightarrow \lambda/2 \sim 2$ cm.
[25] For AC currents in the microwave range, the electric current flows mainly in a small layer of the conductor, between the outer surface and a level called the skin depth
[26] For AC currents in the microwave range, the current flow region in a conductor is constrained by currents flowing in nearby conductors.
[27] Coherent, ref. Mephisto MOPA 25 W
[28] AA Opto-Electronic, ref. MCQ80-A2.5-L1064-Z42-C47Bc

fiber [29] with a length of two meters, and high-power connectors [30]. At high power, the fiber coupling efficiency is $\sim 60\%$ and we obtain up to 11 W at the fiber output. On the optical table, a lens for UV high energy lasers [31] with a focal length of f=200 mm focuses the beam into the science cell (see Fig. 2.15).

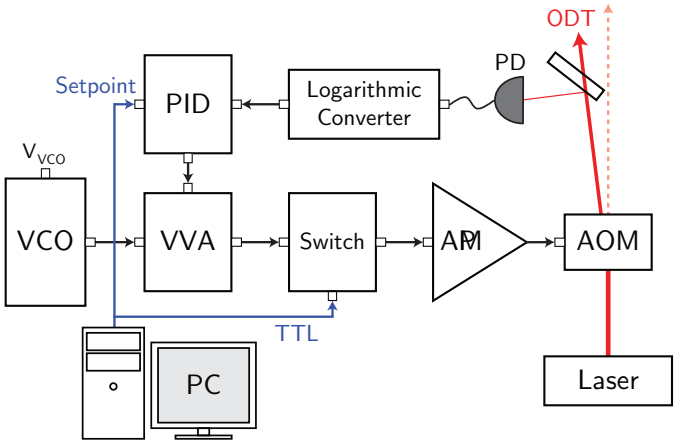

Figure 2.14: Feedback loop to control and stabilize the power of the ODT beam. The AOM driver consists of a voltage controlled oscillator (VCO), a voltage variable attenuator (VVA), a switch and an amplifier (AMP). Part of the ODT power is measured with a photo diode. The photo diode (PD) current is logarithmically converted into a voltage. A PID circuit compares this voltage to a setpoint, chosen in the experimental control software, and acts on the VVA to change the AOM efficiency. Due to the logarithmic converter, the power of the ODT can be varied in a range of three orders of magnitude. The switch allows to turn the ODT on or of, by sending a TTL signal from the experimental control.

2.11.1 Power stabilization

To stabilize the laser power of the ODT, we use the circuit shown in Fig. 2.14. The laser beam power changes with the power of the radio frequency (RF) signal applied to the AOM. The RF signal is generated by the AOM driver, which comprises a voltage controlled oscillator (VCO) with a frequency of 80 MHz, a voltage variable attenuator [32] (VVA), a switch [33] and a 20 W high-power amplifier [34] (AMP). We can control and stabi-

[29] NKT Photonics, ref. LMA-PM-10
[30] Input connector: Schafter+Kirchoff, ref. 60FC-SMA-T-4-A11-03, output connector: Schafter+Kirchoff, ref. 60FC-SMA-0-M30-37
[31] Melles-Griot, ref. BFPL-200-UV
[32] Mini-Circuits, ref. ZX73-2500-S+
[33] Mini-Circuits, ref. ZAS-1
[34] Mini-Circuits, ref. ZHL-20W-13+

lize the laser power of the ODT by measuring a part of its power [35] with a photodiode [36] (PD), and using this information to act on the RF power for the AOM. For that purpose, the photodiode is connected to a logarithmic converter [37], which generates a voltage proportional to the logarithm of the photodiode current. This voltage serves as the input of a PID controller [38]. The PID controller compares the input to the setpoint we impose with our experimental control software. The PID output is used as the control voltage of the VVA and changes the AOM efficiency and hence the ODT power, hereby closing the feedback loop. The logarithmic converter allows for regulating the laser power in a range of three orders of magnitude.

2.11.2 ODT_2

In the second step of our optical evaporation, we load the atoms into a crossed ODT (see Section 5.4.2). Therefore we need a second ODT (ODT_2). For this we use the zero order beam of the ODT_1 AOM. At the end of the first optical evaporation in ODT_1, the decreased ODT_1 beam power, yields a high power in the zero order beam. This beam passes another 80 MHz AOM [39], and we utilize the +1st order-beam for ODT_2. The beam power control and stabilization are analogous to the ODT_1 circuit (see Fig. 2.14). The components are exactly the same, except for the 2 W RF amplifier [40] driving the second AOM. With one AOM for each ODT, we can switch both dipole traps independently.

2.12 Optical setup – Science Cell

In this section we present the optical setup of the science cell, mounted on an U-shaped optical table (see Fig. 2.15). The two thick red paths (starting at ODT_1 and ODT_2) indicate the setup of the crossed dipole trap at 1064 nm. In addition to a previous separation in frequency [41], the polarisation of ODT_2 is turned by a $\lambda/2$ plate to avoid interference effects with the ODT_1 beam, since both originate from the same laser source. For power control (see Fig. 2.14), reflections of both trapping beams are monitored on logarithmic scaling diodes (D_4 and D_2, respectively). Furthermore, a linearly operating

[35] This can be a leak or a reflection from an optical element.
[36] Thorlabs, ref. SM05PD4A
[37] Analog Devices, ref. AD8304
[38] Stanford Research Systems, ref. SIM960
[39] AA Opto-Electronics, ref. MTS80-A3-1064Ac
[40] Mini-Circuits, ref. ZHL-1-2W
[41] For ODT_1 we use the -1st order beam of the first AOM, and for ODT_2 we utilize the +1st order beam, yielding a frequency separation of 160 MHz.

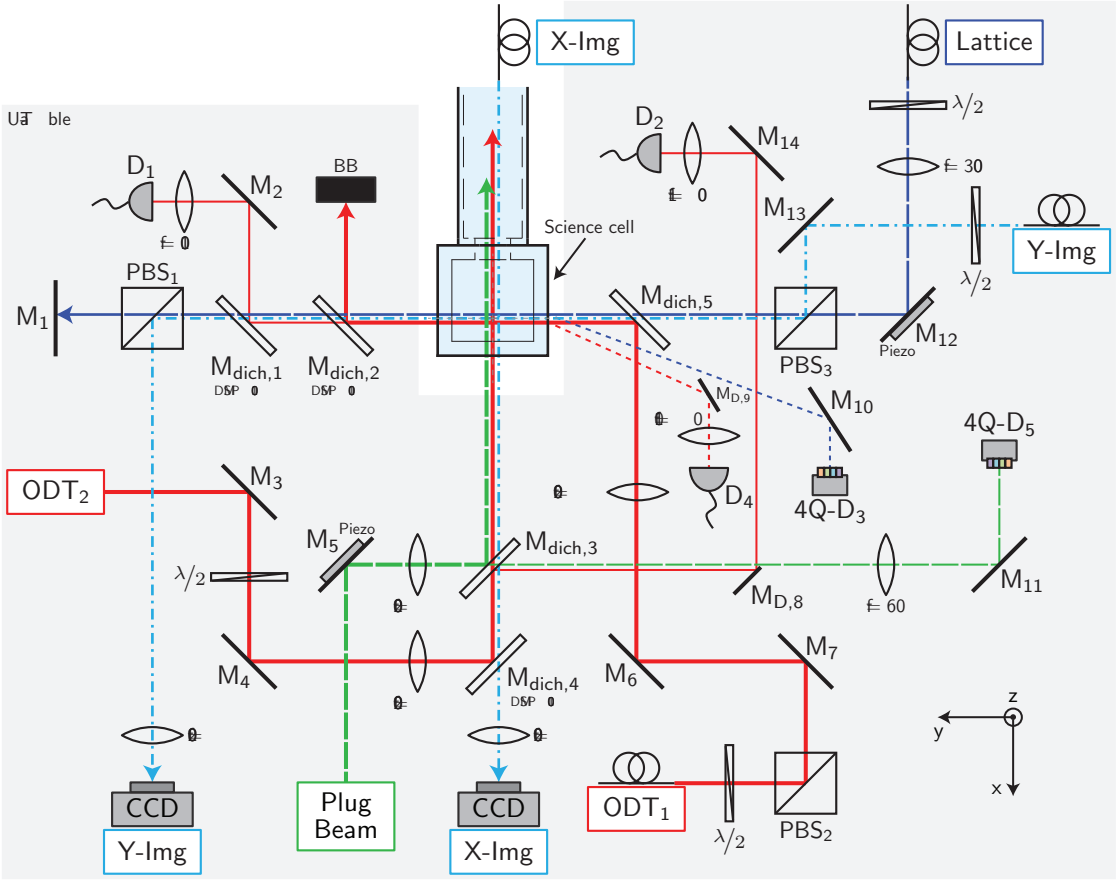

Figure 2.15: Schematic of the optical setup around the science cell. The optics are mounted on a U-shaped table. The optical setup comprises the crossed optical dipole trap (ODT_1 and ODT_2, in red), the optical plug for the magnetic quadrupole trap (Plug Beam, in green), the bichromatic imaging in x- and y-direction (X-Img and Y-Img, dotted blue) as well as the intended optical lattice (Lattice, dark blue). For simplicity, we do not show that all beams have a non zero incident angle on the glass cell to avoid direct back reflections and interference effects. More details are given in the text.

diode (D_1) is used to monitor ODT_1. The dichroic filter $M_{dich,3}$ [42] serves to overlap the blue detuned plug beam with ODT_2. Since the plug-beam needs to be precisely overlapped with the field zero of the magnetic quadrupole trap, its position is monitored on a four-quadrant photodiode (4Q-D_5) and is controlled by a piezo-driven mirror (M_4). A similar technic will be used to monitor the position of the lattice laser which we plan to overlap with ODT_1 ($M_{dich,5}$ [43]). In the later case, a back reflection on the glass cell will be used. All beams have a non zero incident angle on the glass cell to avoid direct back reflections and interference effects. For simplicity, the beam angles are not shown in Fig. 2.15. The two bichromatic imaging beams (X-Img, Y-Img), used for absorption imaging of ^{6}Li and ^{40}K, are depicted in dotted lines. The imaging beam in z-direction is not shown. In x-direction, the magnetic field center is shifted with respect to the science cell center. In this direction, the trap center has a distance of 6.5 mm from the inner glass wall. Therefore, also the laser beams are displaced with respect to the cell center. We shifted the magnetic field center to improve the optical access in x-direction. Because the hight of the glass cell amounts to only 18 mm, the z-direction has the best optical access.

2.13 Diagnostic tools

To gain information about the atomic cloud properties we implemented several probing tools. In the following we describe the fluorescence monitoring and the absorption imaging technique. The section concludes with the experimental control and the data acquisition.

2.13.1 Fluorescence monitoring

We continuously record a part of the emitted MOT fluorescence power with a large area photo diode to estimate the atom number. The fluorescence is proportional to the atom number but depends on the number of excited atoms, the effective MOT beam detunings and intensities. However, when calibrated to the more accurate absorption imaging atom number (see Section 2.13.2), the fluorescence yields good estimates. Furthermore we record the MOT fluorescence with a video camera connected to a TV-screen to obtain information about the MOT position, shape and size. Both detection systems are useful for atom number optimization procedures and debugging.

[42] Thorlabs, ref. DMLP567
[43] CVI Melles Griot, ref. BSR-15-1025

2.13.2 Absorption imaging

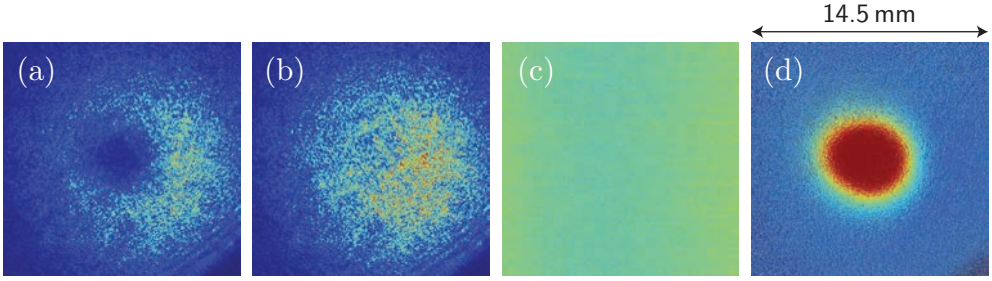

Figure 2.16: Absorption imaging. Three images are necessary to obtaining a normalized transmission profile $T(x,y)$: (a) an image of the probe beam after passing through the atom cloud, (b) an image of the probe beam in absence of the atoms and (c) a background image. Equation (2.1) yields the normalized transmission image (d). The picture shows a ^{40}K cloud, cooled by the D_1 molasses phase (see Chapter 4), after a TOF of 13 ms. The $\sim 1.3 \times 10^9$ ^{40}K atoms have a temperature of 11 μK. The imaging beam is detuned by 1 Γ.

To gain information about the atomic distribution, a charge-coupled device (CCD) camera records the transmission profile $I_{\mathrm{abs}}(x,y)$ of a laser beam. The imaging beam is a near-resonant short pulse with low intensity ($I \ll I_{\mathrm{sat}}$) yielding an intensity independent relative transmission. To account for the inhomogeneous intensity profile of the imaging beam and ambient light, the transmission profile is normalized. Therefore we record a reference picture of the unabsorbed imaging beam yielding $I_{\mathrm{ref}}(x,y)$ and a background picture with $I_{\mathrm{bg}}(x,y)$ and no imaging beam. Figure 2.16 shows the normalized transmission profile

$$T(x,y) = \frac{I_{\mathrm{abs}}(x,y) - I_{\mathrm{bg}}(x,y)}{I_{\mathrm{ref}}(x,y) - I_{\mathrm{bg}}(x,y)}. \tag{2.1}$$

The transmission profile is related to the atomic density distribution $n(x,y,z)$ by

$$T(x,y) = \exp\left(-\mathrm{OD}(x,y)\right) = \exp\left(-\sigma \int n(x,y,z)dz\right), \tag{2.2}$$

where $\mathrm{OD}(x,y)$ is the optical density and σ the scattering cross section. For low beam intensity

$$\sigma = C^2 \frac{3\lambda^2}{2\pi} \frac{1}{1 + (2\Delta\omega_{\mathrm{img}}/\Gamma)^2}. \tag{2.3}$$

Here C and λ are the Clebsch Gordan coefficient and the wavelength of the atomic transition, respectively. $\Delta\omega_{\mathrm{img}}$ is the detuning of the imaging beam from resonance.

When imaging the 3D-MOT, we do not spin-polarize the atoms before imaging and therefore average the squared Clebsch-Gordan coefficients of all possible transitions. [44]

Time-of-flight temperature measurement

In a time-of-flight (TOF) measurement the atoms are released from the trap and expand freely. Assuming a Maxwell-Boltzmann velocity distribution and a collisionless expansion, the waist of the atomic cloud evolves as

$$\sigma_{\mathrm{i}}(t_{\mathrm{TOF}}) = \sqrt{\sigma_{\mathrm{i}}^2(t_{\mathrm{TOF}}=0) + \frac{k_{\mathrm{B}}T}{m}t_{\mathrm{TOF}}^2}, \tag{2.4}$$

with $i \in \{x, y, z\}$ and T the cloud temperature. We determine the temperature by taking absorption images for different time-of-flights and fitting Eq. (2.4) to the measured cloud sizes.

Optical setup

For the MOT chamber imaging, the two imaging beams for ^{6}Li and ^{40}K are superimposed with a dichroic mirror and expanded to a $1/e^2$-diameter of 27.5 mm. The bichromatic beam is circularly polarized and operates on the $4^2S_{1/2}\,|F=9/2\rangle \rightarrow 4^2P_{3/2}\,|F'=11/2\rangle$ and the $2^2S_{1/2}\,|F=3/2\rangle \rightarrow 2^2P_{3/2}\,|F'=5/2\rangle$ cooling transitions of ^{40}K and ^{6}Li, respectively (see Fig. 2.3).
The CCD sensor of our camera [45] has 1392×1024 pixels with a pixel size of $6.45 \times 6.45\,\mu\mathrm{m}^2$. The 2-inch lens that images the atoms on the CCD chip has a focal length of 6 cm and is placed 21 cm away from the atom cloud. Its numerical aperture is $NA = 0.12$. The magnification of the imaging system is ~ 0.4.

2.13.3 Experiment control and data acquisition

In our experiment we use three computers. The first one controls the experiment. The second receives the raw images of the CCD cameras and evaluates the normalized transmission profile (see Fig. 2.16). Important cloud parameters are extracted and automatically saved to an output file. The third computer can access these files and is used for data analysis.

[44] For ^{6}Li and ^{40}K we image on the transitions $|F=3/2\rangle \rightarrow |F'=5/2\rangle$ and $|F=9/2\rangle \rightarrow |F'=11/2\rangle$, respectively. Hence, the averages of the squared Clebsch-Gordan coefficients are $C_{\mathrm{Li}}^2 = 0.5$ and $C_{\mathrm{K}}^2 = 0.4$.
[45] PCO imaging, ref. Pixelfly qe

Experiment control

As a user interface to control our experiment we utilize Cicero Word Generator [46], an open source control software suite designed for atomic physics experiments. It can be used to create and run time sequences on National Instruments cards providing analog and digital outputs.
Cicero Word Generator consists of two main applications, Cicero and Atticus [168]. Cicero is the user interface for editing sequences. Atticus translates the sequences to output buffers and sends these buffers to the output hardware. Cicero supports "batch mode" runs, in which parameters can be scanned through a number of values. We extended and customized the source code to our needs concerning hardware integration and ease-of-use of the control software.
The relevant time scales in our experiment vary from seconds to microseconds, during one experimental sequence. The MOT loading takes several seconds, during which none of the digital or analog channels have changing values. On the other hand the duration of an imaging pulse is $\sim 100\,\mu$s. To avoid long redundant buffers we synchronize the output cards with a variable frequency clock [47]. It generates clock pulses only when the outputs need to change. The output cards use this variable timebase as their sample clock. This reduces the buffer size and generation time, and improves the achievable time resolution [48].
In our experiment we use six analog [49] and three digital [50] output cards. The analog cards have 8 BNC outputs delivering -10 to 10 Volts and up to 250 mA. The digital cards have 24 outputs, giving out either 0 V or 5 V. Most of the digital outputs are opto-coupled to galvanically isolate them from the experiment. This is important because fast switching of high currents in magnetic coils induces high voltages that can disrupt or destroy the output cards.

Data acquisition

The program that saves the raw images recorded during the imaging process is written in Python and is based on a previous version described in [169]. It displays the density profiles of each image and the normalized transmission profile. To calculate the total atom number, the cloud size, its central optical density and other quantities of interest,

[46] http://akeshet.github.io/Cicero-Word-Generator/
[47] Opal Kelly, ref. XEM 3001
[48] The minimum timebase in Cicero is 500 ns.
[49] National Instruments, ref. NI PXI-6713
[50] National Instruments, ref. NI PXI-6533

we use another program written in Octave. It automatically analyses new images and saves the results to an output file, which can be accessed for further data analysis.

2.14 Conclusion

In this chapter we described the components of our experimental setup. We presented the vacuum system, the optical systems, the atomic sources, optical and magnetic traps, the magnetic transport, the optical setup around the science cell, imaging devices and the computer control system.

3 High power 671 nm laser system

In this chapter we present the all solid-state laser source, developed in our group, for laser cooling of lithium atoms. Up to date there are three development stages, each exceeding its antecedent in output power. In Section 3.2, we review the first laser generation. It emits up to 670 mW of coherent light at a wavelength of 671 nm frequency-locked to the lithium D-line transitions, and is described in the thesis of Ulrich Eismann [170]. Section 3.3 is about the intracavity-frequency-doubled light source, emitting 2.1 W at 671 nm [171]. Finally, we introduce the third version of the laser that we use for D_1 sub-Doppler cooling of ^{6}Li (see Section 3.4). Optimization of the thermal management in the gain medium and a new external doubling cavity result in 5 W output power at 671 nm [172].

3.1 Introduction

Lithium atoms are one of the most versatile species used for research on quantum gases. Nature offers significantly abundant bosonic and fermionic isotopes to the experimentalist, allowing the study of both types of quantum statistics [26] in the atomic physics lab. The simple yet powerful technique of magnetic Feshbach tuning of the atomic interactions [173] is the quintessential ingredient for a large number of experiments, and it explains the outstanding role the lithium atom has played in the development of the field.

For realizing a degenerate quantum gas, one needs to implement different laser cooling schemes which typically require near-resonant single-frequency light input in the watt range. The benefits of all-solid-state designs like large output power, high reliability, low maintenance effort and high intrinsic stability are helpful for realizing light sources that will be welcome tools for every ultracold atom experiment.

In this chapter we will present an all-solid-state laser emitting multi-watt single-frequency radiation near 671 nm. The diode-end-pumped design is based on neodymium-doped yttrium orthovanadate (ND:YVO_4) as the gain medium, lasing at the fundamental wavelength of 1342 nm. Second harmonic generation (SHG) is then established using

periodically-poled potassium titanyl phosphate (ppKTP) as the nonlinear medium. Both materials show optimum performances for generating high powers at our target wavelength. The development of a number of related laser sources has been published recently [174–176], and the system realized in our group [176] has proven highly reliable in every-day operation over the period of one year. However, the forementioned sources are currently limited to output powers in the few-hundred-milliwatts regime. We have identified two major limitations for pushing the single-frequency ND:YVO_4-ppKTP concept into the multi-watt range, which are the loss introduced by thermal lensing in the gain medium, and the break down of the nonlinear conversion efficiency at high power. Therefore, one key ingredient of our novel high-power design is an improved heat management in the ND:YVO_4.

Apart from laser cooling of atoms, more applications in the fields of atomic physics and nonlinear optics are currently limited by the available single-frequency 671 nm power. In atom interferometers, a larger and thus more homogeneous gaussian beam can increase the signal-to-noise ratio. The small mass of lithium is advantageous, because it yields a large spatial splitting of the atomic wavepackets [177]. When high-intensity laser beams are employed, the spatial splitting can even be increased by means of multi-photon Bragg scattering [178] . Furthermore, the lithium D-line isotope splitting is large enough to allow selective addressing of the isotopes in hot vapors, making a narrow-bandwidth source attractive for lithium isotope separation [179]. In addition, the creation and long-distance transmission of entangled photons in the low-dispersion, low-absorption wavelength region of standard silica fibers near 1.3 µm has recently been proposed. The scheme uses the output of a sub-threshold optical parametric oscillator in the degenerate regime pumped by a single-frequency 671-nm laser [174]. Finally, our laser could serve as a low-intensity-noise pump for Cr:LiSAF lasers [180].

3.2 First generation

The first generation of the all-solid-state laser source comprises an 1342 nm infrared laser and an external buildup cavity for resonant doubling. Figure 3.1 shows the scheme of the laser system. The active medium, a neodymium-doped yttrium orthovanadate (Nd:YVO_4) crystal, is pumped by a fiber-coupled 808 nm diode stack. The crystal is placed in a bow-tie cavity. The two spherical mirrors produce a stable, Gaussian cavity eigenmode. The flat mirrors serve as input- and output coupler for the pumping light and the 1342 nm output beam, respectively. A Faraday rotator and a $\lambda/2$ waveplate

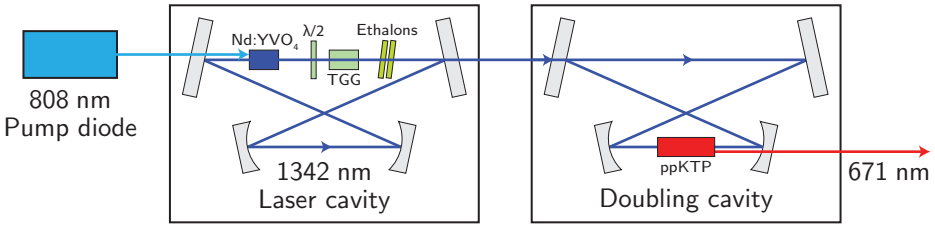

Figure 3.1: Scheme of the first version of the laser system. The laser cavity contains a Nd:YVO_4 laser crystal, a Faraday rotator (TGG) and a $\lambda/2$ waveplate for unidirectional oscillation, and two etalons for frequency selection. The pump diode output is focused in the Nd:YVO_4 crystal. The doubling cavity encloses a nonlinear crystal (ppKTP) for second-harmonic generation.

establish unidirectional lasing. Here the uniaxial laser crystal serves as a polarizer. Two intra-cavity etalons provide single-longitudinal-mode (SLM) operation and coarse tuning. The infrared laser output is mode-matched to the external, unidirectional, bow-tie doubling cavity. Two spherical mirrors produce a focused, Gaussian beam in the nonlinear, periodically-poled potassium titanyl phosphate (ppKTP) crystal for frequency doubling. The flat mirrors are the input- and output couplers for the 1342 nm and the 671 nm light, respectively.

To lock the 671 nm output from the doubling cavity to the lithium D lines, first the doubling cavity's resonance frequency is locked to the infrared cavity's emission wavelength via a feedback circuit. Then the infrared laser is locked to the lithium D lines by means of Doppler-free spectroscopy in a lithium vapor cell. A double-pass AOM in the spectroscopy setup creates an adjustable offset frequency.

3.2.1 The Nd:YVO_4 gain medium

Neodymium-doped yttrium (ortho-) vanadate ia a popular gain medium, because of the strong emission line at 1342 nm and other advantageous characteristics. Figure 3.2 shows a simplified level scheme of the neodymium ion in the YVO_4 host. The laser source operates on the ${}^4F_{3/2} \rightarrow {}^4I_{13/2}$ transition at 1342 nm and is pumped at 808 nm.

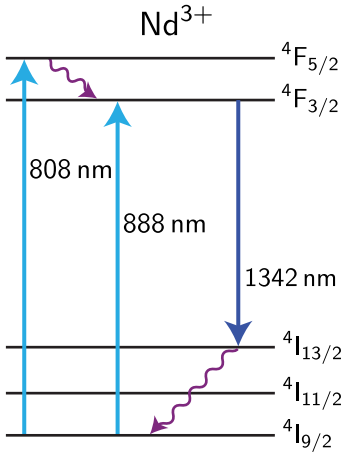

Figure 3.2: Simplified level scheme of the neodymium ion (Nd3+) in the YVO_4 host crystal. The straight and wavy arrows denote photonic- and vibrational transitions, respectively. The laser source operates on the ${}^4F_{3/2} \rightarrow {}^4I_{13/2}$ transition at 1342 nm. The metastable ${}^4F_{3/2}$ level can be pumped with 808 nm or 888 nm. The former transition has a significant higher absorption coefficient (see Fig. 3.4), and higher heating per cycle.

3.2.2 Crystal structure

The crystal structure of YVO_4 is shown in Fig. 3.3. It is of zircon type and hence an optically uniaxial material with a-,a- and c-axis. We utilize an a-cut crystal. Therefore we can access both the a- and c-axis by choosing the polarization orientation of a linearly polarized beam, traversing the crystal.
The neodymium doping denotes the percentage of yttrium ions replaced by neodymium ions and is given in at.%. It determines the pump absorption per unit length for a given wavelength and is an important quantity concerning the thermal management in the gain medium. Typical values range from $0.1 - 3$ at.%.

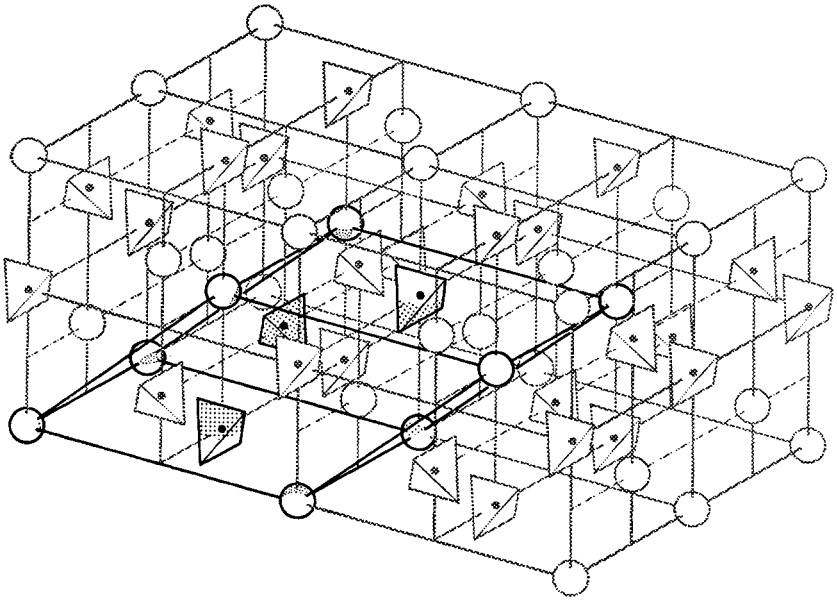

Figure 3.3: Zircon type crystal structure of YVO_4 (from [181]). The unit cell is marked in bold lines. Tetrahedra represent the VO_4^{-3} ions and balls indicate yttrium atoms.

3.2.3 Absorption

In our setup we use laser-diode end pumping to create a population inversion in the gain medium. The pump beam traverses the active medium collinear to the cavity eigenmode. Figure 3.4 shows the absorption spectrum of Nd:YVO_4 for 1 at.% doping. [1] For nearly all wavelengths the absorption is considerably higher for the c-axis. There are several absorption bands close to 808 nm, and two bands at 880 nm and 888 nm. The absorption coefficient has a maximum at 808 nm. Because the absorption feature is quite narrow the temperature of the pump diode stack has to be stabilized to guarantee a fixed emission wavelength.

The 888 nm absorption line has several advantages, in particular for high-power designs. First, the quantum yield is higher than for the 808 nm transition. Because more relative pump photon energy is turned into laser photon energy, the heating of the laser crystal by phonons is reduced. Second, the 888 nm absorption line is quasi-polarization-insensitive. This is convenient, since the output of our laser diode stack is randomly polarized. [2] Finally, the absorption coefficient at 888 nm is significantly smaller. Therefore, the heat input can be distributed over a longer laser-crystal, reducing thermal stress and facili-

[1] For small doping, the absorption coefficient scales linearly with the doping.
[2] Typically laser diode stacks are coupled to non-polarization-maintaining multi-mode fibers.

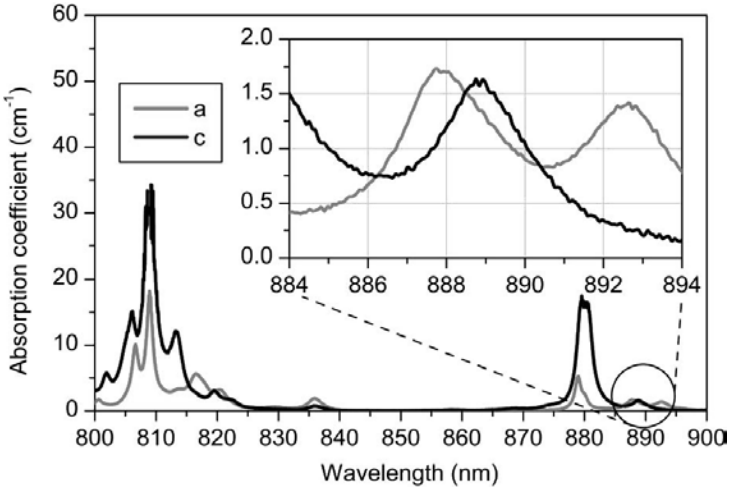

Figure 3.4: Nd:YVO_4 absorption spectrum of both crystal axes for 1 at.% doping concentration (from [182]). Several absorption bands exist at 808 nm, 880 nm and 888 nm. The absorption band at 888 nm is nearly polarization-independent.

tating heat dissipation. The commercially available doping concentration limits the use of 808 nm as pump-wavelength. The heat load is unavoidably distributed over a smaller volume, due to the large absorption coefficient and the minimum available doping. That is why we replaced the 808 nm pump by a 888 nm laser diode stack for the second and third laser generation (see Sections 3.3 and 3.4).

3.2.4 Thermal effects in solid-state lasers

Detrimental thermal effects in the active medium limit the output power of a diode-pumped solid-state laser. To achieve high power outputs, thermal management in the laser crystal is essential.

Pump light locally heats the active medium, since it is partially absorbed by phononic transitions (see Fig. 3.2).[3] The pump-light-induced heating has several detrimental effects. First, the refractive index of the active medium changes locally, causing thermal lensing. The thermal lens changes the laser cavity's eigenmode and can lead to instabilities. Second, the local heating causes stress and strain, effecting the refractive index and thus leading to thermal lensing. Third, the stress bulges the end faces of the laser crystal, again creating thermal lensing. In addition, the stress can excess the breakage threshold and destroy the medium. Finally, thermal lensing leads to aberrations, be-

[3] Thermal effects in laser crystals are reviewed in [183].

cause the phasefront of a passing laser beam is modified non-quadratically, which in turn causes losses.
Therefore, preventing thermal lensing is crucial for power scaling. In our setup the Nd:YVO_4 crystal is wrapped in indium foil and fixed in a solid water-cooled copper mount to efficiently remove heat. We applied several strategies to reduce thermal lensing in the active medium in the newer laser versions. We discuss them in Sections 3.3 and 3.4.

3.2.5 Performance

In the following we present the performance of the first laser generation. For a complete characterisation we refer the reader to [170, 176].
The diode-pumped ND:YVO_4 laser source emits up to 1.3 W at 1342 nm, [4] and can be tuned over 100 GHz.
The resonant buildup cavity for efficient frequency doubling of the 1342 nm Nd:YVO_4 laser uses a ppKTP crystal as nonlinear medium. Spatial mode- and impedance matching lead to a high power-conversion efficiency of 86% and a maximum 671 nm output power of 670 mW. The passive round-trip loss of the doubling cavity is smaller than 0.5%.
The linewidth of the laser is 200^{+400}_{-200} kHz and its relative intensity noise drops to the photon shot noise level above 300 kHz.

3.3 Second generation: Intracavity-frequency-doubling

This section is based on the following manuscript:

2.1-watts intracavity-frequency-doubled all-solid-state light source at 671 nm for laser cooling of lithium
U. Eismann, A. Bergschneider, F. Sievers, N. Kretzschmar, C. Salomon, and F. Chevy
Opt. Express **21**, 9091 (2013)

In this section, we present the second laser generation based on intracavity second-harmonic generation [171]. In this setup, the nonlinear ppKTP-crystal is directly inserted in the infrared laser cavity (see Fig. 3.5). We develop a simple theory for the efficient implementation of intracavity second harmonic generation. Its application to our system allows us to obtain nonlinear conversion efficiencies of up to 88%. Single-mode operation and tuning is established by adding an etalon to the resonator. The second-harmonic wavelength can be tuned over 0.5 nm. The laser can be mode-hop-free scanned over more

[4] We use the maximum output power $P_{\mathrm{pump}} = 42.6\,W$ of the fiber-coupled Coherent FAP-400 diode stack emitted at 808 nm.

than 6 GHz, corresponding to around ten times the laser cavity free spectral range. The output frequency can be locked with respect to the lithium D-line transitions for atomic physics applications. Furthermore, we observe parametric Kerr-lens mode-locking when detuning the phase-matching temperature sufficiently far from the optimum value.

This section is organized as follows: In Section 3.3.1 we present the optimization of the fundamental laser design. [5] In Section 3.3.2, we implement intracavity second harmonic generation. In Section 3.3.3, we report on the course and continuous fine tuning behavior and nonlinear-Kerr-lens mode locking, and we conclude in Section 3.3.4.

3.3.1 The fundamental laser

A first step towards a stable high-power frequency doubled laser source is the availability of an efficient laser system at the fundamental wavelength. To minimize detrimental thermal effects in the gain medium, the following pathway has been chosen: A pump wavelength of 888 nm in contrast to the former 808 nm [176] leads to a lower quantum defect per absorption-emission cycle [182], and thus to lower heating for a given pump rate. In addition, a larger value for the laser crystal length has been chosen in order to spread the heat input over a bigger volume. Therefore, heat transport from the central region to the crystal mount is facilitated. The ND:YVO_4 peak temperature is lower, and thermal issues are less of a concern.

A schematic overview of the laser setup is given in Fig. 3.5. The output of an 888-nm fiber-coupled diode laser bar (NA = 0.22, 400 µm fiber core diameter) is imaged by two lenses L_1 and L_2 [6] into the 1.0% at.-doped ND:YVO_4 crystal. The crystal is a-cut, $4 \times 4 \times 25\,\mathrm{mm}^3$ and anti-reflection coated on both sides for 1342 nm and 888 nm. It is wrapped in indium foil and mounted in a water-cooled copper block. The mirrors M_{1-4} constitute a bow-tie cavity. M_1, M_3 and M_4 are highly reflective at 1342 nm, and M_1 is transmitting at 888 nm. M_3 and M_4 are concave mirrors with a radius of curvature of 100 mm. M_2 is the output coupler for which mirrors with different values of transmission are available. The cavity dimensions are $M_1M_2 \sim 300$ mm, $M_2M_3 \sim M_1M_4 \sim 210$ mm and $M_3M_4 \sim 97$ mm. To force unidirectional operation we use a Faraday rotator consisting of a terbium-gallium-garnet rod-shaped crystal (TGG) of 6 mm length embedded in a strong permanent magnet [184] in combination with a true-zero-order half-wave plate. An uncoated infrared fused silica etalon of 500 μm thickness serves as a wavelength selective element.

[5] The optimization of the fundamental laser is done without the ppKTP crystal in the cavity
[6] $f_1 = 75$ mm, $f_2 = 200$ mm

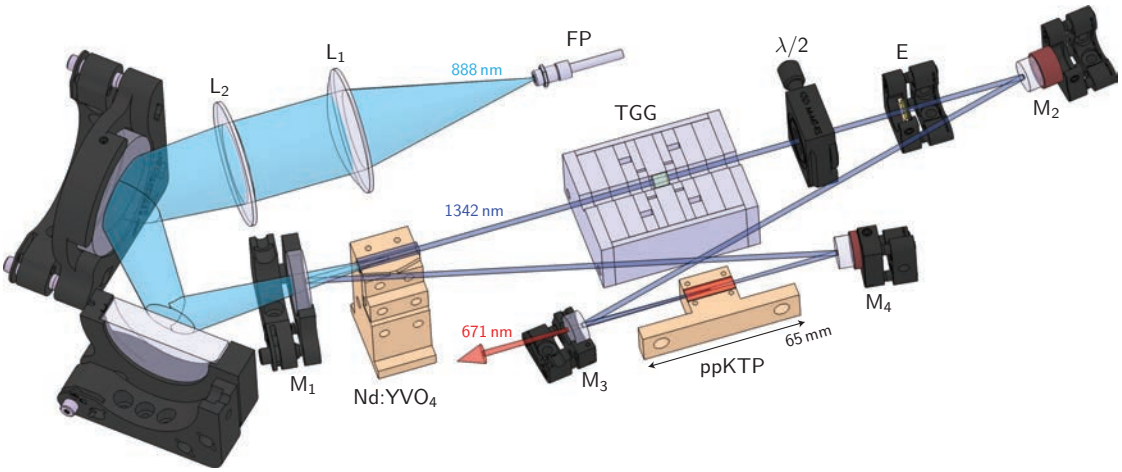

Figure 3.5: Scheme of the second laser generation. The pump source, a fiber-coupled diode laser bar (FP), is imaged into the gain medium by a pair of lenses L_1 and L_2. The Nd:YVO_4 gain medium is placed in a four-mirror bow-tie ring resonator consisting of mirrors M_{1-4}, which are highly reflecting at 1342 nm. Unidirectional operation is forced employing a terbium gallium garnet (TGG)-based Faraday rotator in combination with a half-wave plate ($\lambda/2$). The use of an etalon (E) allows for stable single-longitudinal-mode operation. The nonlinear crystal (ppKTP) is inserted at the tight focus between the curved mirrors M_3 and M_4. The second harmonic output beam (red) is transmitted through M_3. For the measurements presented in Section 3.3.1, the ppKTP was removed and the distance M_3-M_4 adjusted accordingly, and the high-reflectivity mirror M_2 was replaced by a partly transmitting output coupling mirror. The fundamental laser beam (dark blue) is then coupled out through M_2.

For maximum power output, it is crucial to optimize the overlap of the pump beam and the cavity mode [185, 186]. For simplicity, we perform this operation on the empty laser cavity, consisting of M_{1-4} and the ND:YVO_4 only. We use the maximum value of the absorbed pump power $P_{\mathrm{abs,max}} = 32.5\,\mathrm{W}$, and a $\mathcal{T} = 5\%$-transmission output coupler (M_2). By changing the magnification of the pump imaging setup consisting of L_1 and L_2, the top-hat shaped pump spot diameter was altered between 1080 µm and 1400 µm (see Fig. 3.6). The size of the cavity mode in the laser crystal can be changed using the curved mirror distance M_3M_4, and was optimized for each data point. The maximum output power is obtained at a pump diameter of around 1300 µm, where it is kept for the remainder of this section.

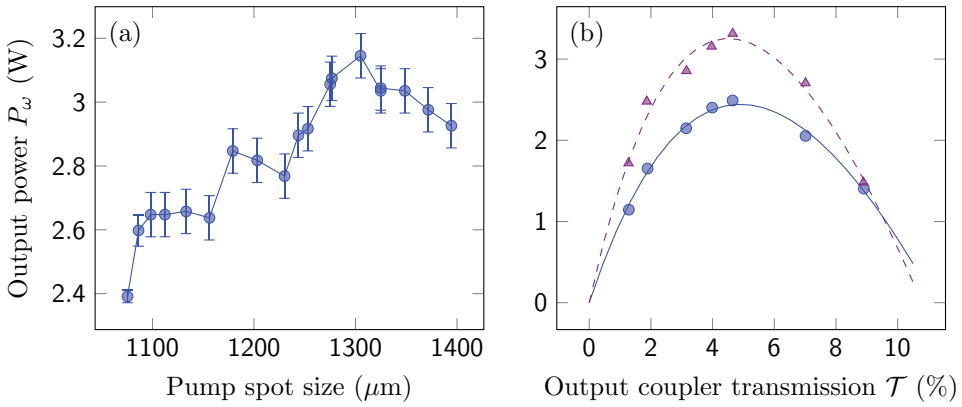

Figure 3.6: (a) Optimization of the output power by changing the pump spot diameter, performed on the laser cavity presented in Fig. 3.5 with all the intracavity elements removed, except for the ND:YVO_4. For a $\mathcal{T} = 5\%$ output coupler (M_2), the mode overlap was optimized for each pump spot diameter by slight adjustments of the curved-mirror distance M_3-M_4. Lines are guides to the eye only. (b) Rigrod analysis. The infrared output power P_ω is measured as a function of the output coupler transmission $\mathcal{T}$ and fitted with the Rigrod model (Eq. (3.1)) for bidirectional (purple triangles, dashed line) and unidirectional (blue circles, solid line) operation at $P_{\mathrm{abs,max}} = 32.5\,\mathrm{W}$ and optimized mode overlap. In both cases the optimum transmission is found at $\mathcal{T} \sim 5\%$. The parasitic roundtrip loss determined from the fits yield 10(4)% for the bidirectional and $\mathcal{L} = 16(6)\%$ for the unidirectional case.

For both the bidirectional (empty cavity only containing ND:YVO_4) and the unidirectional (additional TGG and half-wave plate) operation we measured the maximum output power as a function of the output coupler transmission, see Fig. 3.6b. In both cases a $\mathcal{T} = 5\%$ mirror delivers the maximum fundamental output power P_ω. By equating the single-pass gain with the total round-trip loss $\mathcal{L}_{\mathrm{tot}} = \mathcal{L} + \mathcal{L}_{\mathrm{out}} = \mathcal{L} + \mathcal{T}$ for both the bi-

and unidirectional cases, where $\mathcal{L}$ is the sum of the parasitic round-trip losses, we find

$$P_\omega = P_{\mathrm{sat}}\mathcal{T}\left[\frac{G_0}{\mathcal{T}+\mathcal{L}} - 1\right] \tag{3.1}$$

similarly to [187]. Here P_{sat} is the saturation power, G_0 the small-signal gain and $\mathcal{L}$ the sum of the parasitic round-trip losses. Although this analysis essentially relies on plane waves, it can be mapped to the more realistic case of top-hat pump beams and gaussian laser cavity eigenmodes, as present in diode-pumped solid-state lasers, see [176] and references therein. A least-squares fit to Eq. (3.1) yields $\mathcal{L} = 10(4)\%$ for the parasitic loss in the bidirectional case. In [176] we found the loss in an empty four-mirror bow-tie cavity of mirrors from the same batch to be smaller than 1%. We attribute the remaining 9(4)% mainly to aberrations caused by the thermal lens in the ND:YVO_4.

In the unidirectional case, the fitting procedure yields $\mathcal{L} = 16(6)\%$. Compared to the bidirectional case, the difference of $\mathcal{L}_{\mathrm{Faraday}} = 6(7)\%$ can be attributed to the insertion of the TGG crystal and the waveplate. Indeed, thermal depolarization and the accompanying loss is a well-known effect in TGG. It imposes stringent limits on power scaling of unidirectional ring lasers and Faraday isolators [188]. We observe a dependence of the optimum half-wave plate angle on the circulating intracavity power, which is strong evidence of this effect. From the fit, we furthermore obtain the values $P_{\mathrm{sat}} = 170(50)\,\mathrm{W}$ and $G_0 = 0.27(5)$ for unidirectional operation, which are important for the optimization of intracavity doubling, see Section 3.3.2.

For the now-optimized unidirectional infrared setup, we measure the output power as a function of the absorbed pump power P_{abs} (see Fig. 3.7). As the optimization is performed at the maximum absorbed pump power $P_{\mathrm{abs,max}} \sim 32.5\,\mathrm{W}$, the laser emission only starts at $P_{\mathrm{abs}} \sim 28\,\mathrm{W}$. After reaching threshold, the output power is unstable and displays a hysteresis feature between $P_{\mathrm{abs}} = 29\,\mathrm{W}$ and $30\,\mathrm{W}$. After crossing the hysteresis region, the laser emission is stable and only weakly depends on P_{abs}. This behavior is typical for high-power solid-state laser designs and has been reported in [189]. As discussed before, thermal depolarization in the TGG is significant and can lead to a change of the lasing direction and occasional bistable behavior when increasing the pump power. Thus, the angle of the half-wave plate had to be adjusted for every data point presented here. We keep the pump power constant at $P_{\mathrm{abs,max}} \sim 32.5\,\mathrm{W}$ in the remainder of the section.

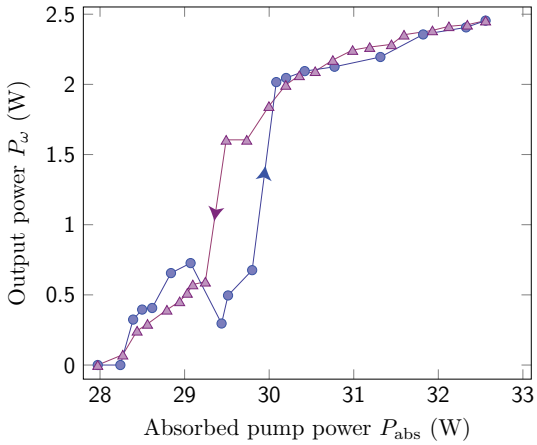

Figure 3.7: Infrared unidirectional output power P_ω as a function of the absorbed pump power P_{abs}. The setup is optimized for the maximal absorbed pump power $P_{\mathrm{abs,max}} = 32.5\,\mathrm{W}$. The oscillation threshold is found at $P_{\mathrm{abs}} \sim 28\,\mathrm{W}$. The data shows hysteresis between $P_{\mathrm{abs}} = 29\,\mathrm{W}$ and 30 W, as indicated by the arrows for increasing or decreasing pump power. This behavior is typical for high-power designs. After a sudden rise the output power increases only slowly until it eventually reaches the maximum of 2.5 W at $P_{\mathrm{abs,max}}$. Lines are guides to the eye only.

3.3.2 Efficient intracavity second-harmonic generation

Efficient frequency doubling of infrared lasers can be established using periodically-poled nonlinear crystals in an external cavity. Using this method at a fundamental wavelength of 1342 nm, a doubling efficiency of $P_{2\omega}/P_\omega = 86\%$ has been obtained in our first-generation setup [176], and serves as a benchmark. However, a more direct approach followed here is intra-cavity second harmonic generation (ICSHG), which requires only one cavity and thus represents an important simplification.

For the analysis of the output power of ICSHG lasers, the output coupling loss $\mathcal{L}_{\mathrm{out}} = \mathcal{T}$ discussed in Section 3.3.1 needs to be replaced by ηP, where η is the single-pass doubling efficiency, and P the circulating intracavity power. Similar to the one found in [190,191], the solution for the SH output power in the unidirectional case reads

$$P_{2\omega} = \frac{P_{\mathrm{sat}} G_0}{\xi} \left[\sqrt{(\xi - \zeta)^2 + \xi} - (\xi + \zeta) \right]^2 , \tag{3.2}$$

where $\xi = \eta P_{\mathrm{sat}} (4G_0)^{-1}$ and $\zeta = \mathcal{L}(4G_0)^{-1}$ are the dimensionless output coupling and loss parameters. As pointed out in [190, 191], it is interesting to note that the value for the optimum output coupling $\mathcal{L}_{\mathrm{out,opt}} = \sqrt{G_0 \mathcal{L}} - \mathcal{L}$ is the same for both linear and non-linear output coupling mechanisms, and delivers the same amount of output power. However, the round-trip parasitic loss $\mathcal{L}$ will contain an additional contribution from

the insertion of the nonlinear medium. Hence, $P_{2\omega}/P_{\omega} < 1$ for any realistic system, but efficiencies close to one can be obtained in practice [192]. Using the fit values from Section 3.3.1, we maximize Eq. (3.2) by choosing an optimum single-pass doubling efficiency $\eta_{\mathrm{opt}} = 0.10(5)\%.\mathrm{W}^{-1}$.

To evaluate η, we refer to the Boyd-Kleinman theory for focused gaussian beams [193],

$$\eta(T) = \frac{2\omega^3 d_{ij}^2 L}{\pi\varepsilon_0 c^4 n_{\omega,i}(T) n_{2\omega,j}(T)} \times h[\alpha, \beta(T)]\,, \tag{3.3}$$

where ε_0 is the vacuum permittivity, c the speed of light in vacuum, d_{ij} is the i,j-th element of the material's nonlinear tensor, $n_{\omega,i}(T)$ the material's refractive index along the i axis at angular frequency ω and temperature T, and L the nonlinear material's length. d_{ij} needs to be replaced by $d_{\mathrm{eff}} = 2d_{ii}\pi^{-1}$ for periodically poled (pp) materials. The function

$$h[\alpha, \alpha_0, \beta(T)] = \frac{1}{4\alpha}\left|\int_{-\alpha-\alpha_0}^{\alpha-\alpha_0} \frac{\mathrm{e}^{\mathrm{i}\beta(T)\tau}}{1+\mathrm{i}\tau}\,\mathrm{d}\tau\right|^2\,, \tag{3.4}$$

is the dimensionless Boyd-Kleinman function [193]. $\alpha = L\,(2z_{\mathrm{R}})^{-1}$ and $\alpha_0 = z_0\,(2z_{\mathrm{R}})^{-1}$ are the focusing and offset parameters, respectively. z_{R} is the Rayleigh length, and z_0 is the offset of the beam focus with respect to the nonlinear medium's center. The phase-matching parameter reads $\beta(T) = 4\pi z_{\mathrm{R}}\lambda^{-1} \times \left\{n_{\omega,i}(T) - n_{2\omega,j}(T) - \lambda[2\Lambda(T)]^{-1}\right\}$, where λ is the vacuum wavelength. The $\Lambda(T)$ term only occurs for periodically poled materials, where $\Lambda(T)$ is the poling period, and the temperature dependence results from thermal expansion.

In the intracavity-doubling setup, we replace the output coupling mirror M_2 by a high-reflectivity mirror, cf. Fig. 3.5. The nonlinear, periodically-poled potassium titanyl phosphate crystal (ppKTP) is inserted between the concave mirrors M_3 and M_4. To account for the ppKTP refractive index, the distance $\mathrm{M}_3\mathrm{M}_4$ is increased to $\sim$106 mm. The nonlinear crystal has outer dimensions of $1 \times 6 \times 18\,\mathrm{mm}^3$ and is antireflection coated at 1342 nm and 671 nm. Its poling period $\Lambda = 17.61\,\mu\mathrm{m}$ is chosen for phase matching at 23.5°C according to the temperature-dependent Sellmeier equations from [194, 195]. However, in a previous study we found the phase-matching temperature at 33.2°C [176]. This deviation can be explained by uncertainties on the reported Sellmeier equations, and the manufacturing tolerance on the ppKTP poling period. The nonlinear coefficient $d_{33} = 14.5\mathrm{pm}.\mathrm{V}^{-1}$ found for the crystal in our preliminary study is 14% lower than the highest literature value reported so far [196], probably due to poling imperfections [176]. Using this crystal for nonlinear output coupling, we can easily obtain a single-pass efficiency

$\eta > \eta_{\mathrm{opt}}$, such that design considerations are relaxed, and we are able to tune to η_{opt} by changing the phase-matching temperature. For temperature stabilization, the crystal is wrapped in indium foil and mounted in a temperature-controlled copper block. The frequency-doubled light is transmitted through mirror M_3.

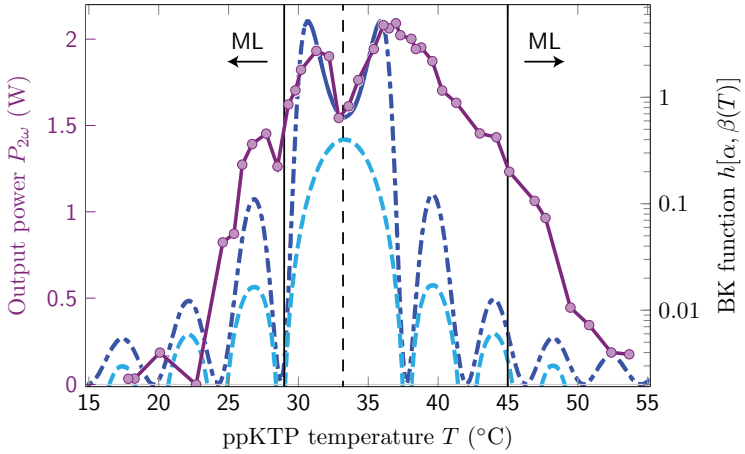

Figure 3.8: Output power as a function of the phase-matching temperature (purple circles, lines are a guide to the eye only). The data shows a double-peak structure of 1.9 W / 2.1 W of output power slightly off of the optimum phase-matching temperature of 33.2°C (central vertical line). A simple theoretical model presented in the text (dash-dotted dark blue line) describes the data well in the central high-conversion region, using the known temperature dependence of the single-pass doubling efficiency, which is proportional to the dimensionless Boyd-Kleinman function $h(T)$ [dashed light blue line, Eq. (3.4)]. The dashed vertical line indicates the perfect phase-matching temperature of $T_{\mathrm{pm}} = 33.2°\mathrm{C}$, where $\beta(T_{\mathrm{pm}}) \simeq 0$, and the nonlinear output coupling is too high to reach maximum output power. The vertical lines with arrows indicate the temperature regions where self-mode locking occurs, cf. Section 3.3.3.

In Fig. 3.8 we present the measurement of the second-harmonic output power as a function of the phase-matching temperature of the ppKTP crystal. We find a maximum of 2.1 W of output power at $T_{\mathrm{pm}} = 36°\mathrm{C}$, and a second maximum of 1.9 W at $T_{\mathrm{pm}} = 31°\mathrm{C}$. As expected from Eq. (3.2), at the perfect phase matching temperature the output power only amounts to 1.6 W because $\eta > \eta_{\mathrm{opt}}$. The FWHM of the temperature-tuning curve is 22 K. As compared to the maximum infrared power presented in the former section, we obtain a maximum doubling efficiency of 88%. The excellent mode quality of the second-harmonic light is confirmed by a single-mode fiber coupling efficiency larger than 80%.

To gain deeper insight in our data, we employ the ICSHG theory (Eqs. (3.2) to (3.4)). We include the additional parasitic intracavity loss caused by the presence of the etalon and the nonlinear crystal, which amounts to $\mathcal{L}_{\mathrm{add}} = 0.6(1)\%$. Thus, the theory predicts a maximum SH output power of 2.1 W, as is found experimentally. The value of $\mathcal{L}_{\mathrm{add}}$

is compatible to the sum of the ppKTP insertion loss measured independently [176] and the calculated walk-off loss for the etalon [170]. From an ABCD-matrix formalism we obtain the cavity eigenmode, yielding $z_R = 11.5\,\text{mm}$ and $z_0 = 3\,\text{mm}$. At perfect phase matching, we obtain $h = 0.40$, yielding a SH output power of 1.6 W, which is in excellent agreement with our findings. This gives us further confidence in our previously measured value of d_{33} [176]. The temperature-dependent KTP refractive indices and the thermal expansion coefficient of the poling period were presented in [194, 195]. We adjust β by an additive constant in order to account for the measured phase matching condition $\beta(T = 33.2°\text{C}) = 0$, as justified before. The theory (solid purple line in Fig. 3.8) describes the data well in the central high conversion region, and yields the characteristic double-peak structure.

Outside of the central region, the circulating intracavity power rises significantly and the power-dependent thermal depolarization loss would need to be accounted for in our simple model. As compared to the theory, the data displays less evidence of dips. This can be explained by a thermal smearing effect due to residual absorption in the ppKTP at large powers, yielding a spatial dependence of the phase-matching parameter $\beta(T)$. Outside of the region indicated by the solid vertical lines, the laser is in mode-locked (pulsed) operation, and we do not expect our model to be applicable.

3.3.3 Tuning behavior and nonlinear-Kerr-lens mode locking

For course tuning and single-longitudinal-mode (SLM) operation, the laser was equipped with an uncoated etalon of 0.5 mm length, yielding a free spectral range of 210 GHz. We note that this single, weakly-selective etalon is sufficient for this purpose due to the self suppression of axial mode hopping in intracavity-frequency-doubled lasers [197, 198].

The tuning range of the frequency-doubled laser is characterized and compared to the infrared laser in Fig. 3.9. Apart from having the same shape and features, it is striking to note that the output power of the frequency-doubled laser amounts to almost the same value as the non-doubled laser over the entire emission spectrum. As discussed in Section 3.3.2, the nonlinear output coupling is close to the optimum level over the entire emission wavelength range. The gain line center, where the output power is maximal, is found at around 671.1 nm, resulting in 2.2 W of fundamental and 2.1 W of second-harmonic output. At the lithium-D line wavelength the output power amounts to ∼1.8 W. Close to the gain line center, this result compares favorably to the value obtained in [175], where the authors used an etalon for tuning which potentially produces significantly higher tilt loss [170, 199]. Comparing the emitted power of the doubled and non-doubled lasers across the emission spectra, we typically obtain more than 80% of

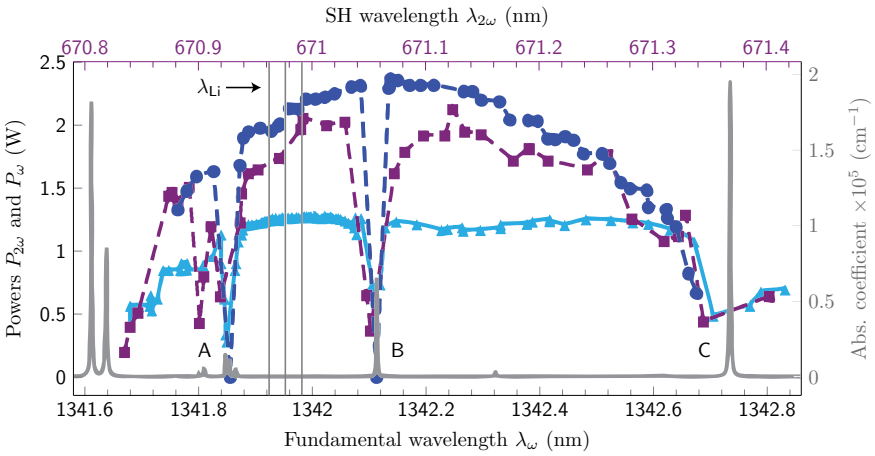

Figure 3.9: (Lines are guides for the eye only) Single-frequency output spectra of the infrared laser presented in Section 3.3.1 (dark blue circles), the intracavity-frequency-doubled laser (purple squares) and the infrared source presented in [176] (light blue triangles). For easy comparison, all wavelengths are given in vacuum values. The vertical lines denote the positions of the lithium-D line resonances. The gray line shows a water vapor absorption spectrum for typical parameters (23 °C, 60% rel. humidity). The wavelength regions marked A,B,C where stable, powerful operation of the lasers can not be established coincide with absorption peaks of water molecules. The level of output power of the infrared laser and the frequency-doubled laser are closely spaced, proving that the nonlinear crystal introduces weak additional passive losses in the laser cavity, whereas the degree of nonlinear output coupling is at its optimum value.

the power at 671 nm, demonstrating a very efficient frequency doubling process. For the absolute maximum values, we obtain $P_{2\omega}/P_\omega = 88\%$. It is even possible to obtain emission further away from resonance, where the non-ICSHG lasers cease to oscillate. Our first-generation source presented in [176] displays an output spectrum that is significantly more plateau-like (light blue triangles in Fig. 3.9), which we attribute to the presence of a second, more selective etalon in the cavity. At the expense of a higher insertion loss baseline, ripples in the emission spectrum have significantly less influence on the tuning behavior of this setup. The identical gaps in all of the emission spectra presented here (A,B,C in Fig. 3.9) can be explained by absorption from water vapor, as we compare the laser spectra to a water vapor absorption spectrum obtained from the HITRAN database [200]. The water absorption peaks coincide with the features A,B and C.

Intracavity-frequency-doubled lasers tend to mode-locked operation when the doubling crystal is mismatched from the optimum phase matching condition [201,202]. This effect, resulting from an intensity-dependent phase shift of the fundamental beam passing the non-matched crystal, is commonly termed nonlinear-Kerr-lens- or $\chi^{(2)}$:$\chi^{(2)}$ mode locking. Although it has been observed in the 1064-nm-Nd:YVO_4-ppKTP system before [203], we

report, to the best of our knowledge, the first observation at 1342 nm. We observe the effect when detuning from the optimum phase-matching temperature to below T_{low} =29°C and above T_{high} =45°C. A scanning Fabry-Perot spectrum analyzer shows no discernible single- or few-mode background once the threshold to mode-locked operation is crossed. We use a fast detector and a spectrum analyzer to measure the beat frequency between neighboring modes. This simple method to determine the laser cavity free spectral range yields a value of 345(1) MHz.

It is remarkable that the mode locking arises when tuning the phase-matching temperature to colder-than-optimal values. In analogy to standard Kerr-lens mode locking, the $\chi^{(2)}$:$\chi^{(2)}$ process requires an additional intracavity element which modifies the round-trip gain or loss as a function of the power-dependent cavity mode size. This can be realized by the gain medium, cf. Fig. 3.5. As we presented in Section 3.3.1, the pump-to-cavity mode overlap has been carefully optimized in the cw regime. However, an ABCD-matrix-based cavity mode calculation reveals that the beam waist in the Nd:YVO_4 only changes monotonously when crossing over from negative to positive focal powers in the ppKTP. Thus, the induced change in gain or loss should be less favorable whenever the lensing departs from the optimized value. We note that Zondy et al. [192] argue that pulsed operation should occur whenever there exists a power-dependent gain-loss mechanism, whichever is the sign of the focal power in the ppKTP. Furthermore, we also note that in our simple analysis, we do not take into account different Kerr-like and thermal lenses that may occur in the intra-cavity elements other than the laser and nonlinear crystals. Using the temperature-dependent Sellmeier equations of [194, 195], we get dephasing parameters of $\beta(T_{\mathrm{low}}) = 8.8(1)$ and $\beta(T_{\mathrm{high}}) = -18.5(1)$, resulting in a single-pass efficiency $\eta(T)$ reduced to less than 5% of the maximum value.

The laser can be tuned continuously using a piezoelectric transducer (PZT), upon which mirror M_2 is glued. This allows mode-hope free scans of the 671-nm output frequency over more than 6 GHz. For the resonated fundamental light this amounts to about ten times the laser cavity free spectral range, a typical behavior of ICSHG lasers with self-suppressed mode hopping [197, 198]. We perform Doppler-free saturated absorption spectroscopy on a lithium vapor cell described previously in [176], see Fig. 3.10. In Fig. 3.10a we show a sample scan over the full Doppler-broadened ^{6}Li D_1 line. The ground-state hyperfine structure is clearly resolved. We phase-modulate the probe beam at 20 MHz using an electro-optic modulator, and use a commercial lock-in amplifier to generate a dispersive error signal as presented in Fig. 3.10b. We can access all D line transitions of both naturally abundant lithium isotopes, and the full ground state hyperfine structure is resolved.

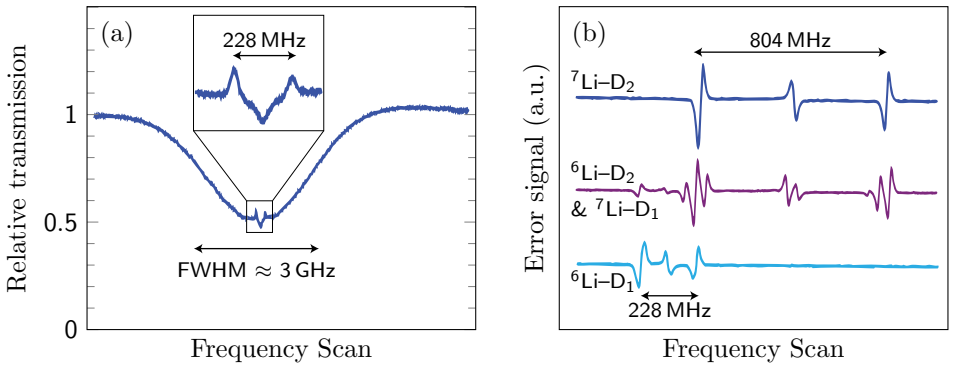

Figure 3.10: Doppler-free saturated absorption spectroscopy of the lithium D-lines. (a) Sample scan over the entire ^{6}Li D_1 Doppler-broadened absorption peak. The inset shows the sub-Doppler features. Similar spectra are obtained for all lithium D lines. (b) Error signals of all lithium D line transitions, generated by phase modulation spectroscopy. These signals provide an excellent reference for frequency-locking of the laser.

The laser linewidth was estimated by slowly scanning the emission frequency over the D_1 line of ^{6}Li. From the observed peak-to-peak noise in the linear part of the error signal we obtain an upper limit of 1 MHz for the laser linewidth. For frequency-locking the laser, we feed the error signal in a home-made proportional-integral controller. The regulator signal is split internally in a low-frequency part, sent to the slow PZT (M_2) used for scanning the laser, and a high-frequency part, sent directly to a fast PZT glued between M_4 and its mount. The system can easily stay locked for a full day, even in presence of significant acoustic noise coupled to the optical table.

3.3.4 Conclusion

In this section we presented the design and the performance of an all-solid-state, intracavity-frequency-doubled single-mode laser source. The ring laser emits up to 2.5 W of unidirectional multifrequency radiation at the fundamental wavelength, and we determine the parameters necessary for efficient ICSHG. Starting from this well-characterized infrared system, the optimized ICSHG yields up to 2.1 W of single-mode, frequency-stabilized output at 671 nm. We discussed a simple theory describing the output power of an intra-cavity frequency-doubled laser. Within the region of efficient nonlinear conversion, the theory describes our experimental findings well. We furthermore presented a measurement of the emission spectrum of both the fundamental and the ICSHG source, displaying around 1.8 W of output power at the lithium D lines. By comparing both emission spectra, we maximally obtain 88% of the fundamental power at 671 nm, and typically more than 80%. This demonstrates a very efficient ICSHG process across the

full emission spectrum. We observe nonlinear-Kerr-lens mode-locked operation when detuning the ppKTP temperature sufficiently far from the phase matching condition. Furthermore, we discussed the fine-tunability of the source by presenting Doppler-free saturated absorption spectra of all lithium D line transitions. The 671-nm output can be mode-hop-free scanned over more than 6 GHz, which corresponds to more than ten times the laser cavity free spectral range. As compared to the most powerful conventional design [176], our laser is an improvement by more than a factor of three in terms of output power. In comparison to commercial semiconductor tapered amplifier designs, we gain a factor of four in terms of output power and keep a beam quality close to the diffraction limit. Compared to vertical external cavity surface emitting laser (VECSELs) designs [204], our laser is five times more powerful together with a linewidth in the 100-kHz range.

The output power of our source is largely sufficient for creating all the laser beams needed for an ultracold atoms experiment. However, for other applications such as atom interferometry, even more power might be helpful and we will briefly discuss how this can possibly be established. An obvious way is to use a different cavity geometry allowing for two-sided pumping of the active medium. Convex pump couplers can compensate the thermal lens close to the laser crystal, which has proved very efficient in high-power resonators, see for instance [189]. A large part of the output power limitations stems from the additional intracavity elements, such as the Faraday rotator. Thus, injection locking of an amplifier consisting of an empty high-power resonator such as presented in [189] could deliver tens of watts of single-frequency fundamental light. At these elevated power levels, efficient single-pass frequency doubling of 1342-nm radiation has been demonstrated [205], the implementation of which considerably relaxes the complexity of multi-cavity designs.

When we started to use the laser for our experiment, we noticed that switching off the laser and turning it on again resulted in a reduced and arbitrary output power. Sometimes the laser would not even start lasing. The re-optimization was often time-consuming and inconvenient for a day-to-day use. We suspect that we operated the laser in a semi-stable regime, probably caused by a too large doping of the laser crystal. The instabilities could be also linked to the self suppression of mode hopping.

3.4 Third generation: Power scaling

In the previous section we showed that intracavity second harmonic generation yields high power output at 671 nm and considerably simplifies the laser- and locking scheme

compared to a setup with an external buildup cavity. However, we were not satisfied with the instable behaviour after turning-on the laser. Therefore we decided to return to the external buildup scheme for the third laser version. In this section, we present a characterization of the third laser generation and compare it to the older generations.

3.4.1 Scheme

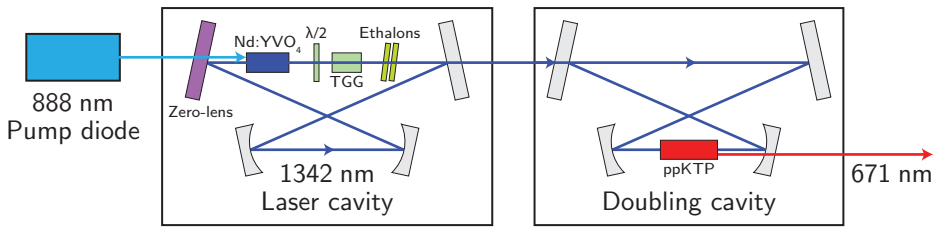

Figure 3.11: Scheme of the third laser version. The laser cavity contains a Nd:YVO_4 laser crystal, a Faraday rotator (TGG) and a $\lambda/2$ waveplate for unidirectional oscillation, and two etalons for frequency selection. The pump diode output is focused in the Nd:YVO_4 crystal. The doubling cavity encloses a nonlinear crystal (ppKTP) for second-harmonic generation.

A comparison between Fig. 3.1 and Fig. 3.11 shows that the schemes of the first and third laser versions are very similar. The laser cavity is pumped by a laser diode stack and injects a doubling cavity for second-harmonic generation. However, an improved thermal management enables infrared power scaling by a factor of ∼5 without considerably changing the laser cavity's geometry. In the following we describe the improvements of the laser design and its performance.

3.4.2 Infrared laser

Three major improvements lead to a large gain in output power. First, we use a pump at 888 nm instead of 808 nm, thereby increasing the quantum yield (see Section 3.2.3). Second, the doping of the Nd:YVO_4 is now 0.5 at.% instead of 1 at.% used for the second laser version. Therefore, the absorbed pump energy is distributed over a larger region in the laser crystal and can be dissipated more easily. Both updates reduce the thermal lensing. Finally, a convex pump coupler[7], also called zero-lens, replaces the flat incoupling mirror of the first laser version, and compensates for the thermal lensing of the cavity mode in the laser crystal. The cavity-surface of the zero-lens is convex, with a radius of curvature of 500 mm. The pump beam is not effected by the zero-lens, because the curvature of the outer surface compensates the effect of the cavity-surface, hence its name.

[7] M_1 in Fig. 3.12

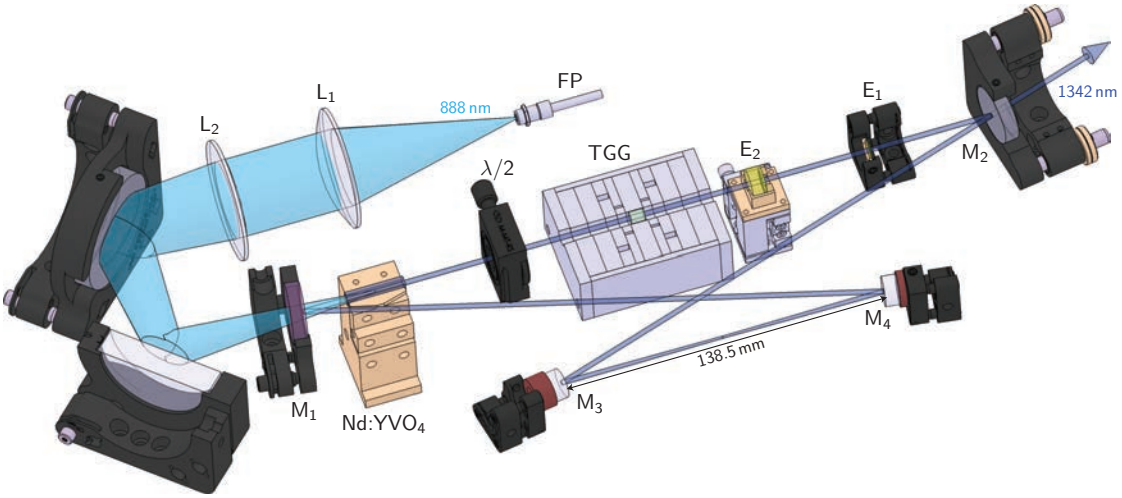

Figure 3.12: Design of the third laser generation. The fiber coupled pump source is labeled FP. Two lenses $L_{1,2}$ focus the pump beam in the Nd:YVO_4 active medium. The zero-lens cavity mirrors M_1 compensates for thermal lensing of the cavity mode in the laser crystal. The $\lambda/2$ wave plate and the TGG Faraday crystal in a magnet force unidirectional operation. Two etalons $E_{1,2}$ enable single-mode operation and tunability. The optical path of the generated laser beam is depicted in green. For some mechanical components (mirror mounts, Nd:YVO_4 mount, TGG magnets and E_2 mount) we show a sectional view to improve visibility of the beam path. The distance between the curved cavity mirrors M_1 and M_2 is 138.5 mm. The output beam is transmitted through M_2 ($\mathcal{T}_{\text{out}} = 7.5\%$). For a schematic drawing of the resonator setup see Fig. 3.11

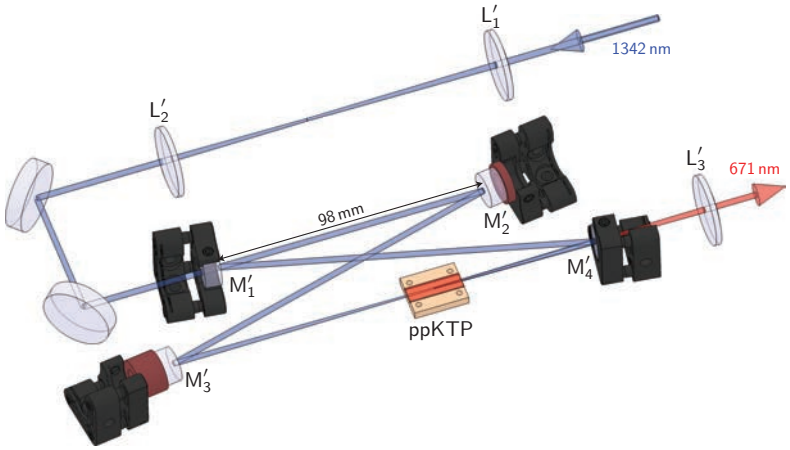

Figure 3.13: Doubling cavity. The laser beam at 1342 nm is depicted in green, the SH beam in red. The four-mirror folded ring cavity houses a ppKTP nonlinear crystal for SH generation. The lenses L'_1 and L'_2 mode match the laser output to the cavity eigenmode. L'_3 collimates the SH output. The nonlinear crystal is placed in the cavity's smallest waist of $\omega_0 \simeq 75\,\mu$m.

The better heat management of the third laser version results in an output power of 6.6 W at 1342 nm. This is a large improvement compared to the output power of 1.3 W of the first laser version (see Section 3.2).
The mechanical design of the third version of the fundamental laser is shown in Fig. 3.12.

3.4.3 Doubling cavity

The doubling cavity scheme equals the one of the first laser generation. However, optimized thermal management improves the performance of the doubling cavity (see Section 3.4.5). In the new setup the cavity's waist, where the ppKTP crystal is placed, is $\omega_0 \simeq 75\,\mu$m instead of $\omega_0 \simeq 55\,\mu$m, as for the first laser generation. Therefore, detrimental thermal effects and gray-tracking at high powers are reduced.
The doubling cavity is a four-mirror folded ring cavity, building up a powerful traveling fundamental wave at 1342 nm (see Fig. 3.13). The reflectivity $\mathcal{R}_C = 90\%$ of the plane coupling mirror M_1' accounts for impedance matching. All other mirrors are highly reflective at 1342 nm. The concave mirrors M_3' and M_4' have a radius of curvature of 150 mm and 100 mm, respectively. Two spherical lenses L_1' and L_2' mode match the laser output to the cavity eigenmode. After M_4' transmits the frequency doubled light, f_3' collimates the SH output beam to a $1/e^2$ radius of 1 mm. The performance of the doubling cavity is characterised in Section 3.4.5.

3.4.4 Locking scheme

The lock system serves to frequency-stabilize the laser system to the lithium D lines. Figure 3.14 shows the locking scheme comprising two feedback loops for the doubling- and laser cavity. First, the doubling cavity's length is stabilized to frequency match its resonance with the Nd:YVO_4 laser frequency. This ensures good second harmonic efficiency and allows us to perform lithium spectroscopy. Then the doubled Nd:YVO_4 output frequency is locked to the desired lithium transition by controlling the length of the laser cavity.
The cavity's resonance frequency changes with its optical length L_{opt}. Therefore, two mirrors per cavity are mounted on piezo-electric transducers (PZTs), one with slow actuation and large range, the other with fast actuation but limited range.

Doubling cavity lock

We frequency-lock the doubling cavity to the laser with a phase/frequency modulation technique. EOM_1 (in Fig. 3.14) phase-modulates the infrared pump light at $\nu_1 =$

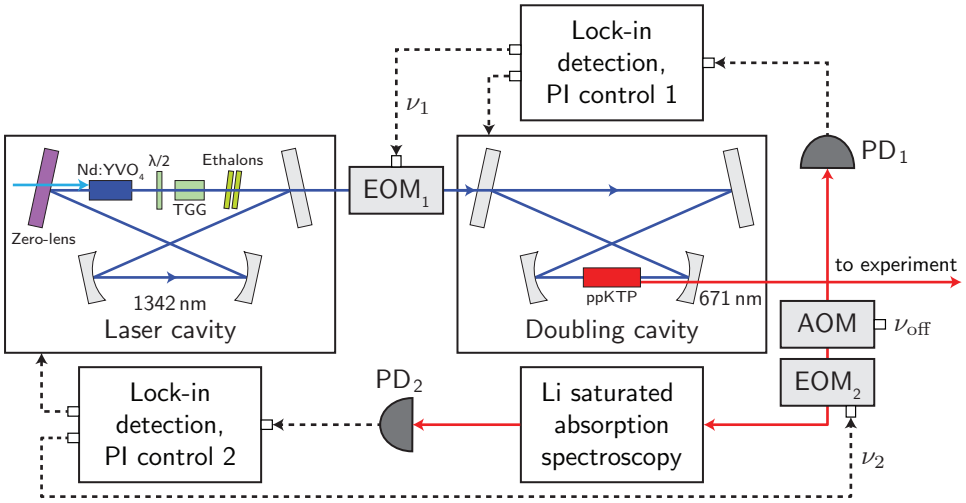

Figure 3.14: Scheme of the lock system. Light paths and electronic signals are illustrated by straight- and dashed lines, respectively. First, the doubling cavities resonance frequency is locked to the free-running Nd:YVO_4 laser using control circuit components indexed 1. A part of the second harmonic light serves for lithium spectroscopy. In a second step this reference serves to lock the doubled Nd:YVO_4 laser output frequency with respect to one of the Lithium resonance frequencies, using control circuit 2. A double pass AOM with driving frequency ν_{off} controls the frequency offset between the atomic resonance and the laser output frequency

0.5 MHz. Hence, the frequency-doubled light is also phase modulated. A fast photodiode detects the frequency-doubled light, leaking out of the doubling cavity, before it is demodulated with a lock-in detection circuit. The resulting error signal is fed into a proportional-integral (PI) controller circuit, that separates the frequency ranges for the two actuator PZTs.

Laser lock

The laser cavity is locked to an atomic transition by means of saturated-absorption frequency modulation spectroscopy [206] in a lithium vapor cell with frequency-doubled light. A double-pass setup with a 200 MHz AOM allows to frequency-shift the spectroscopy light. The probe beam of the saturated absorption is phase-modulated at $\nu_2 = 1.2$ MHz by EOM$_2$, before it passes the spectroscopy cell. A fast photodiode [8] detects the probe light. The error signal is created with a lock-in amplifier. A two-way PI circuit separates the frequency ranges for the two actuator PZTs.
When scanning the laser frequency via the slow PZT (M_4 in Fig. 3.11), an adjustable ramp signal is fed forward to the doubling cavity's lock signal, thus minimizing lock deviations and stabilizing output power.

[8] Newport, ref. 1801

3.4.5 Experimental results

In this section we describe the experimental results, obtained for the third laser generation. The performance of the infrared- and the doubling cavity is compared to the first laser generation. A more detailed discussion of the new laser as well as waveguide-doubling will be presented in the thesis of Norman Kretzschmar [207] and in [172].

Infrared laser

To quantify the performance of the infrared laser, we measured the output power at 1342 nm as a function of the absorbed pump power at 888 nm (see Fig. 3.15a).

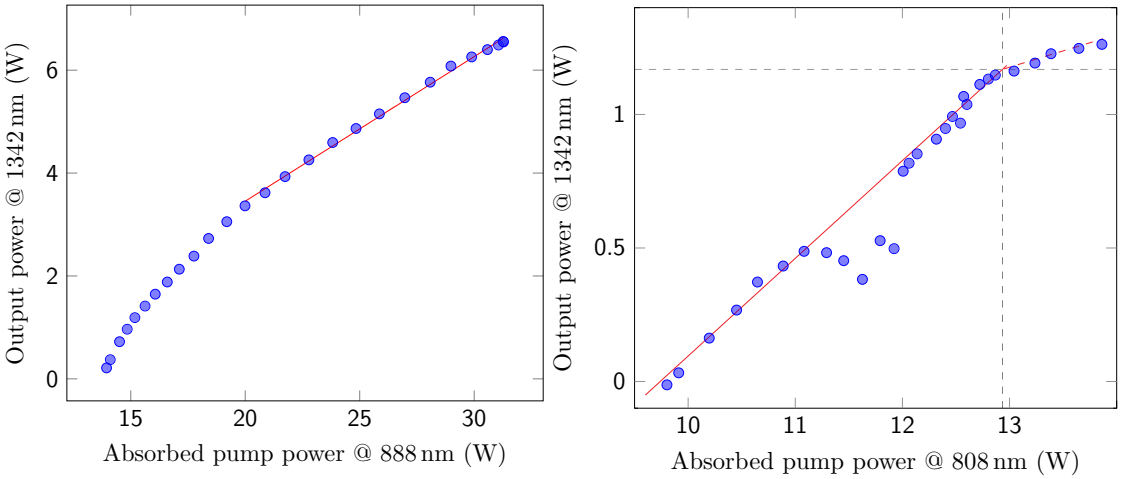

(a) Third laser generation **(b)** First generation (see [176])

Figure 3.15: Single-frequency laser output as a function of the absorbed pump power. (a) 888 nm-pump: $P_{\mathrm{abs,max}} = 31.3\,\mathrm{W}$ corresponds to a pump diode output of ∼42 W. For $P_{\mathrm{abs}} > 20$, a linear fit to the data yields a slope efficiency of ∼0.28. (b) 808 nm-pump: $P_{\mathrm{abs,max}} = 13.8\,\mathrm{W}$ corresponds to a pump diode output of ∼42 W. Note the unstable domain near $P_{\mathrm{abs}} = 11.5\,\mathrm{W}$ and the reduced slope efficiency for $P_{\mathrm{abs}} > 12.9\,\mathrm{W}$. The maximum output power is five times larger for the third laser generation.

The lasing threshold is at $P_{\mathrm{abs}} \sim 13.8\,\mathrm{W}$. For pump powers larger than ∼20 W, the output power increases approximately linear with the pump power, yielding a slope efficiency of ∼0.28. The pump diode emits up to 42 W. Therefore, the absorbed pump power is limited to $P_{\mathrm{abs,max}} = 31.3\,\mathrm{W}$. Until $P_{\mathrm{abs,max}}$ we observe no significant derivation from the linear power scaling. Hence, at this point only the available pump power limits the maximum output power to 6.6 W.
In contrast to the first laser generation (see Fig. 3.15b), we neither observe an unstable domain nor a reduced slope efficiency for high powers. The 808 nm pump diode of the first

laser generation also emits up to 42 W. However, the maximum absorbed pump power at 808 nm, $P_{\mathrm{abs,max}} = 13.8\,\mathrm{W}$, is smaller than the absorbed pump power of the third laser generation. The maximum output power at 1342 nm of the third laser generation, $P_{\mathrm{out,max}} = 6.6\,\mathrm{W}$, is five times larger than that of the first generation.

Doubling cavity

For the performance measurements, the doubling cavity is locked to the infrared laser. Figure 3.16a shows the intra-cavity conversion of the new doubling cavity. The SH output power $P_{2\omega}$ increases quadratically with the intra-cavity power P_ω, the single-pass efficiency being $\eta = 0.22\%/\mathrm{W}$. For a pump power $P_{\mathrm{in}} = 6\,\mathrm{W}$, the intra-cavity power is $\sim$47 W and results in a SH output power of $\sim$5 W.

The intra-cavity conversion of the first doubling cavity generation shows a quadratic behavior only until $P_\omega(P_{2\omega}) = 9\,\mathrm{W}\,(640\,\mathrm{mW})$ (see Fig. 3.16b). Fast intensity-dependent detrimental effects induce a slow linear rise for higher powers. The maximum obtained power is $P_\omega(P_{2\omega}) = 10.7\,\mathrm{W}\,(670\,\mathrm{mW})$.

Comparing the maximum SH output powers of the new and the old doubling cavity yields a gain of $\sim$7.8. Furthermore, at this point only the available pump-power limits the SH output power, as there is no sign of detrimental effects in the measured data.

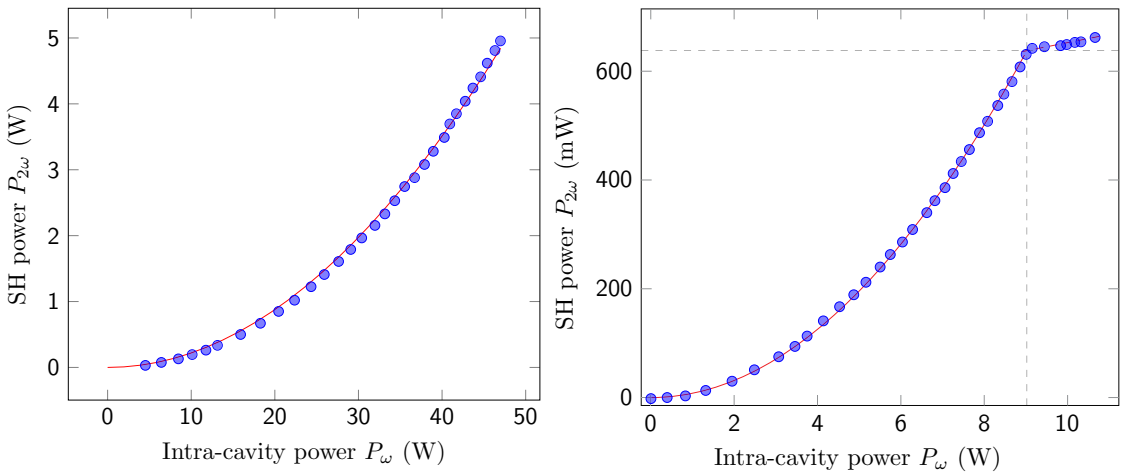

(a) Third laser generation **(b)** First generation (see [176])

Figure 3.16: Intra-cavity conversion of the doubling cavity. SH output power as a function of the intra-cavity power at 1342 nm. The cavity is locked to the infrared laser. (a) Third laser generation: The data (circles) shows no derivation from the parabolic fit (solid line) for the measured range of intra-cavity powers of up to $P_\omega = 47\,\mathrm{W}$. (b) First laser generation: For $P_\omega > 10.7\,\mathrm{W}$ the conversion deviates from the parabolic fit and becomes less efficient.

Figure 3.17 shows the conversion efficiency $\eta = P_{2\omega}/P_{\text{in}}$ as a function of the pump power P_{in}.

The conversion efficiency of the new doubling cavity saturates for high powers. For the highest available pump power $P_{\text{in,max}} = 6\,\text{W}$, the conversion efficiency is $\eta_{\text{max}} = 87\%$ (see Fig. 3.17a).

The old doubling cavity has a maximum conversion efficiency of $\eta_{\text{max}} = 86\%$ at $P_{\text{in}} = 730\,\text{mW}$ (see Fig. 3.17b) before inset of the lock instabilities. The latter reduce the conversion efficiency for higher powers and limit the performance of the old doubling cavity. Therefore, the new doubling cavity presents a major improvement, as it remains stable for high pump powers, enabling single-frequency multi-watt output at 671 nm.

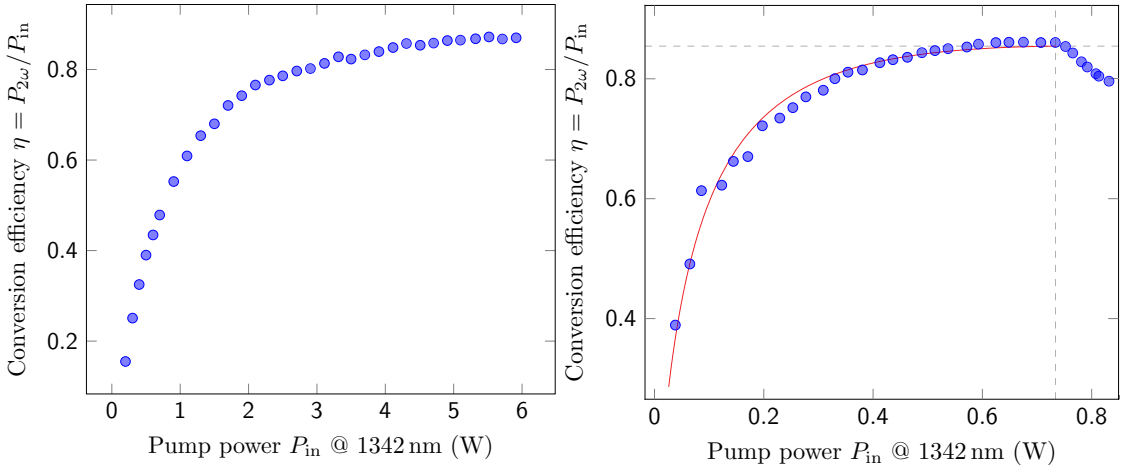

(a) Third laser generation **(b)** First generation (see [170])

Figure 3.17: Conversion efficiency η as a function of the pump power P_{in}. (a) Third laser generation: The conversion efficiency saturates for high powers, reaching its maximum $\eta_{\text{max}} = 87\%$ at $P_{\text{in}} = 6\,\text{W}$. (b) First laser generation: The conversion efficiency rises to $\eta_{\text{max}} = 86\%$ at $P_{\text{in}} = 730\,\text{mW}$. For higher powers, detrimental effects induce lock instabilities, reducing η.

The second harmonic output has an excellent beam quality, with $M^2 \sim 1$. At low power, we are able to couple more than 90% of the red output power through a single-mode optical fiber.

Long-term stability

We used the third laser generation to perform the D_1 molasses measurements for ^{6}Li (see Chapter 4). The laser system stays locked during an entire working day. Because we switch of the laser over night this is only a lower bound to the time the laser stays

locked. The large dynamic range of the PZTs used for locking should allow for a much longer locking time.

In everyday use, we let the system warm-up for one hour. Afterwards, there is no need for power optimization. Furthermore, there is no need to search for the spectroscopy lines on the lock saturated spectroscopy transmission signal, because the high mechanical stability of the laser setup leads to a stable and reproducible cavity length.

For long-term operation, dust is the major reason for the degradation of the laser performance. After three months of every-day operation we retrieved the full output power of the infrared laser and the doubling cavity, simply by cleaning the optics. On the contrary, it was not necessary to touch the alignment. To prevent dust and moisture from reaching the optics, the laser setup is placed in a sealed housing with dry-air atmosphere, yielding long-term stability.

3.5 Conclusion

In this chapter we presented the further development of an all-solid-state laser source at 671 nm for cold-atom experiments with lithium. The first laser generation [176] comprised an infrared laser cavity and a doubling cavity, generating up to 1.3 W and 670 mW of single mode output power at 1342 nm and 671 nm, respectively. The output power was mainly limited by intensity-dependent effects in the doubling crystal. For the second laser generation [171], we followed the approach of intracavity doubling. Furthermore, we replaced the old 808 nm pump source by a new one, operating at 888 nm, to reduce the quantum defect and thus detrimental thermal effects. The optimized intra-cavity second harmonic generation yields up to 2.1 W of single-mode, frequency-stabilized output at 671 nm. However, the mandatory and time-consuming re-optimization after switch-on made the day-to-day use inconvenient. Therefore, we returned to external doubling for the third laser generation. Optimization of the thermal management in the gain medium and a new external doubling cavity result in 6.6 W and 5 W output power at 1342 nm and 671 nm, respectively. Currently, the output power is only limited by the available pump power at 888 nm. The third laser generation constitutes a major improvement compared to the older laser versions, both in output power and stability. Versus commercial tapered amplifier designs, the output power is one order of magnitude larger, while the beam quality is close to the diffraction limit. We might investigate intra-cavity second harmonic generation with the new fundamental laser. The improved thermal management and stability could lead to a stable operation. Alternatively, the laser scheme can be simplified by using a waveguide for frequency doubling. With this approach we obtain output

powers of up to 2.3 W at 671 nm [172]. A detailed characterization of the waveguide-doubling scheme and the current laser setup will be presented in the thesis of Norman Kretzschmar [207].

4 Simultaneous sub-Doppler laser cooling of fermionic ^{6}Li and ^{40}K

This chapter presents a new, three-dimensional optical molasses scheme for simultaneous sub-Doppler cooling of fermionic ^{6}Li and ^{40}K [140, 141]. The cooling scheme is suitable for all alkali atoms, operates on the D_1 line and is based on gray optical molasses cooling. The D_1 molasses is particularly advantageous for atoms whose narrow hyperfine structure of the $P_{3/2}$ excited level compromises efficient sub-Doppler cooling on the D_2 line. In combination with a preceding CMOT phase, that increases the atomic density (see Section 2.7.1), the optical molasses can lead to high phase-space densities on the order of 10^{-4}.

The structure of this chapter is as follows. In Section 4.1 we recall some cooling schemes that are useful to understand the mechanism behind the D_1 molasses.[1] Section 4.2 starts with a description of the D_1 cooling mechanism, followed by the experimental results for ^{40}K and ^{6}Li in single species operation, and ends with the performance of the simultaneous cooling.

4.1 Prelude: Laser cooling

Laser cooling exploits quasi-resonant exchanges of energy and momentum between atoms and laser light to obtain atomic samples at temperatures in the micro- and even nanokelvin range [209–211].

4.1.1 Doppler cooling

Doppler cooling was the first optical mechanism used to cool atoms [212]. The cooling scheme is based on a Doppler induced imbalance between opposite radiation pressure forces. To illustrate the principle of this mechanism, consider a moving two-level atom with groundstate $|g\rangle$ and excited state $|e\rangle$ separated by $\hbar\omega_A$ and velocity v. The atom

[1] A comprehensive overview of different laser cooling schemes and atomic physics in general, can be found in [208].

is illuminated by a counter-propagating laser beam with wave vector $-\mathbf{k}_L$, frequency ω_L and Rabi frequency Ω. The laser beam is red detuned ($\omega_L < \omega_A$) and has a small intensity. The Doppler effect changes the detuning $\delta = \omega_L - \omega_A$ by $k_L v$. The radiative force $\mathcal{F}$ exerted on the atom is therefore velocity dependent:

$$\mathcal{F}(v) = -\hbar k_L \Gamma \frac{\Omega^2/4}{(\delta + k_L v)^2 + (\Gamma^2/4) + (\Omega^2/2)} \tag{4.1}$$

where Γ is the natural width of the exited state. The radiative force is maximum when the Doppler shift compensates the detuning, i.e. when $k_L v = \omega_A - \omega_L$.
If we add a second laser beam with same intensity and frequency propagating in the opposite direction, the Doppler shift has a different sign for the two beams. The resultant total force $\mathcal{F}_D$, of the low intensity standing wave, is the sum of the forces created by the two beams. The two beams create a friction force for small velocities. The cooling is efficient between the two extrema of $\mathcal{F}_D$, where $v = \pm\delta/k_L$.
Doppler cooling works at low laser intensity, the saturation parameter $s = (\Omega^2/2)/(\delta^2 + \Gamma^2/4)$ is hence much smaller than 1. The minimum Doppler cooling temperature

$$k_B T_{\text{Doppler}} = \hbar\Gamma/2 \tag{4.2}$$

is reached when $\delta = -\Gamma/2$. [2]

4.1.2 Bright optical molasses

Testing the Doppler cooling predictions experimentally became possible with the development of suitable laser sources. The first experimental results [39] for sodium were obtained by means of time-of-flight methods and showed that a more efficient cooling mechanism was at work, because the measured temperature was much smaller than predicted by Doppler cooling. In the following we will discuss the basic ingredients of this sub-Doppler cooling. A detailed description can be found in [137, 213]. The two basic ingredients of sub-Doppler cooling are the existence of several sublevels in the ground state and spatial polarization gradients. We consider a 1D laser configuration where the two counter-propagating laser beams have orthogonal linear polarization and low intensities. Figure 4.1 shows how the polarization of the total field varies along the z-direction. The polarization is σ_+ and σ_- in planes separated by a distance $\lambda/4$. In between, it is linear at $\pm 45°$ or elliptical. Sisyphus cooling is based on the existence of several Zeeman sublevels in the ground state. We consider the simplest case of a $F_g = 1/2$ ground state

[2] The D_2 Doppler temperatures of ^{40}K and ^{6}Li are 145 μK and 141 μK, respectively

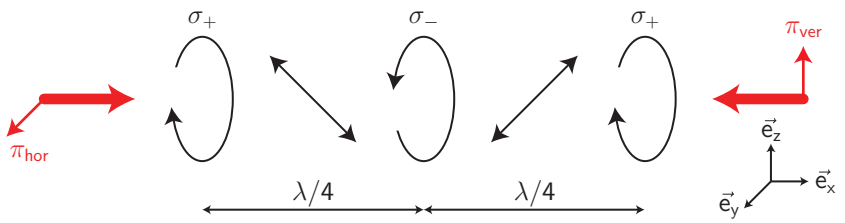

Figure 4.1: Polarization gradients in the lin⊥lin-configuration. Two counter-propagating laser beams with orthogonal polarizations result in a total field with the polarization depending on the x-position.

having only two Zeeman sublevels. As in Doppler cooling, we use an optical transition $F_g \to F_g + 1$, hence $1/2 \to 3/2$, and $\delta = \omega_L - \omega_A < 0$ (red detuning).
The two ground state sublevels are light-shifted, since the laser is not resonant. Polarization gradients spatially modulate these light shifts with a period $\lambda/2$. The modulations are out of phase. For a moving atom in a given Zeeman sublevel the probability to be optically pumped in the other sublevel is highest at the top of the potential hill. The atom is pumped to the bottom of the valley of this sublevel. The repetition of this process makes the atom moving uphill more frequently than downhill. This Sisyphus effect arises because of correlations between the spatial modulations of light shifts and optical pumping rates. Figure 4.2 shows the principle of Sisyphus cooling for bright optical molasses in the lin⊥lin configuration. The energy of the atom decreases step by step until the atom gets trapped in the optical potential wells. The equilibrium temperature is given by

$$k_B T_{\mathrm{sub-Doppler}} \sim \hbar \delta_g \sim \frac{\hbar \Omega^2}{4|\delta| k_B} \propto \frac{\text{laser intensity}}{\text{detuning}}, \tag{4.3}$$

where δ_g is the light shift and where we have assumed a low intensity ($s \ll 1$) and a large detuning ($|\delta| \gg \Gamma$). At low intensity, the light shift of the ground state is much smaller than the natural width Γ of the excited state. Therefore it is possible to obtain temperatures about two orders of magnitude lower than the Doppler limit, which scales as $\hbar\Gamma$ (see Eq. (4.2)).[3] The final temperature of the atomic ensemble results from the competition of two effects. On the one hand, the friction force emerging from Sisyphus cooling damps the atomic momenta. On the other hand the fluctuation of the radiative forces leads to a momentum diffusion. These fluctuations occur because of the random atomic recoils related to spontaneous emission processes. Therefore, the semi-classical approximation breaks down in the small temperature limit, because the steady-state rms atomic momentum δp cannot be smaller than the single photon recoil $p_{\mathrm{Recoil}} = \hbar k$.

[3] The predictions concerning the equilibrium temperature have been experimentally verified [214].

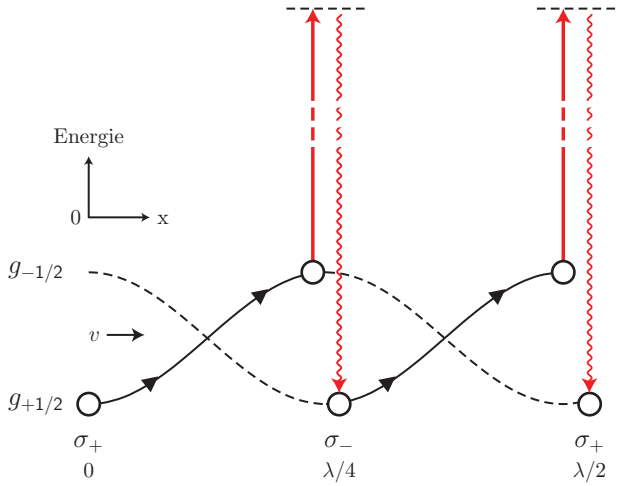

Figure 4.2: Principle of Sisyphus cooling for bright optical molasses in the lin⊥lin configuration. The time lag τ_p of the optical pumping time allows a moving atom, initially in the $g_{+1/2}$ Zeeman sublevel, to go from the potential valley to the potential maximum. Here the probability to be optically pumped to the other sublevel $g_{-1/2}$ is large and the atom is pumped to the bottom of the corresponding potential valley. From here the cycle is repeated. The energy of the atom thus decreases step by step.

Hence, the recoil temperature T_{Recoil} is a fundamental limit for bright molasses cooling:

$$k_B T_{\text{Recoil}} = \frac{h^2}{2M\lambda^2}, \tag{4.4}$$

where M is the atomic mass and λ the wavelength of the spontaneously emitted photon. [4]

4.1.3 Sub-recoil laser cooling

However, sub-recoil laser cooling is possible with an approach, not based on friction forces, where the single photon recoil no longer appears as a fundamental limit. Figure 4.3 illustrates the sub-recoil cooling mechanism. During a random walk in momentum space, an atom can get trapped in a small volume around zero, $\mathbf{p} = \mathbf{0}$, and stay there for a very long time, because the photon scattering rate $R(\mathbf{p})$ vanishes for $\mathbf{p} \to \mathbf{0}$. The random walk slows down when $\mathbf{p}$ decreases and stops when $\mathbf{p} = \mathbf{0}$, where the atom is trapped in a velocity dark state, that cannot absorb light. A fluorescence rate $R(\mathbf{p})$ varying with $\mathbf{p}$ as in Fig. 4.3a can be achieved by velocity selective coherent population trapping (VSCPT) [215] or by velocity selective Raman processes [216]. Sub-recoil cooling has

[4] The D_1 recoil temperatures of ^{40}K and ^{6}Li are 400 nK and 3.45 μK, respectively

no lower temperature limit, because there is no steady-state value of the momentum distribution. The longer the interaction time, the lower the temperature.

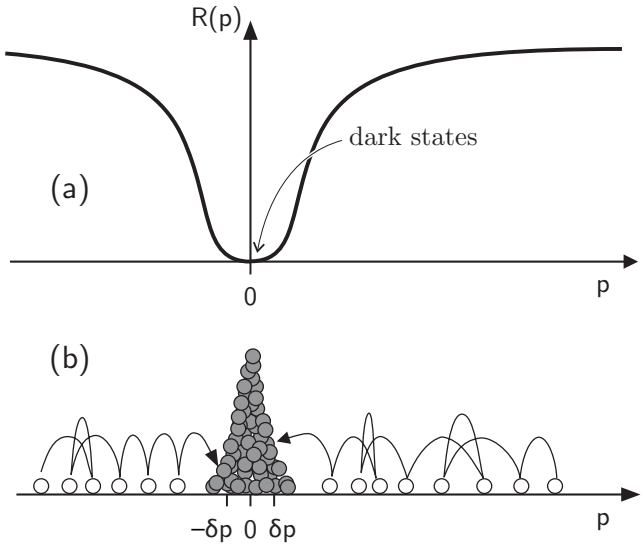

Figure 4.3: Principle of sub-recoil cooling. (a) The fluorescence rate $R(\mathbf{p})$ vanishes at momentum $\mathbf{p} = \mathbf{0}$. (b) The atoms perform a random walk in p-space and accumulate in the vicinity of $\mathbf{p} = \mathbf{0}$. The random walk slows down when $\mathbf{p}$ decreases and stops when $\mathbf{p} = \mathbf{0}$. (from [217])

4.1.4 Velocity selective Coherent population trapping (VSCPT)

Dark resonances and coherent population trapping

Dark resonances play a major role in VSCPT and are known since 1976 [218, 219]. Figure 4.4 sketches the basic concept. In Fig. 4.4a a three-level atom $\{e, g_1, g_2\}$, with one excited- and two ground states, interacts with two laser beams. $\mathbf{E}_1 \exp[i(\mathbf{k}_1 \cdot \mathbf{r} - \omega_1 t)]$ excites the transition $g_1 \rightarrow e$ and $\mathbf{E}_2 \exp[i(\mathbf{k}_2 \cdot \mathbf{r} - \omega_2 t)]$ the $g_2 \rightarrow e$. When the Raman-detuning Δ is zero [5] , the excited state population σ_{ee} vanishes. Because σ_{ee} is proportional to the fluorescence rate R_F, there is no fluorescence for $\Delta = 0$. At the same time the atoms occupy a linear combination of the two ground states which does not absorb light. In other words, the atomic population is trapped in a coherent superposition of g_1 and g_2, hence the name *coherent population trapping* (CPT). Figure 4.4(b) shows the fluorescence rate R_F as a function of the detuning Δ from the Raman resonance condition, where ω_1 is resonant to the transition $g_1 \rightarrow e$. The width Γ' of the R_F-dip around

[5] $\Delta = (\omega_1 - \omega_2) - (E_{g_2} - E_{g_1})/\hbar$

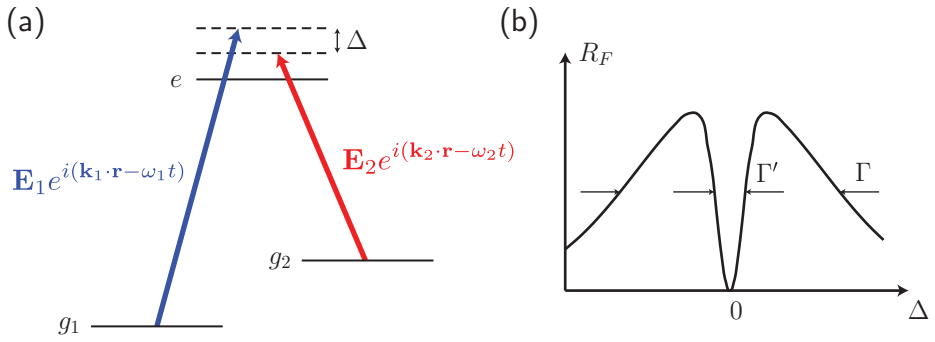

Figure 4.4: Dark resonance in a Λ-type atomic system. (a) Interaction between a three-level atom $\{g_1, g_2, e\}$ and two laser beams, exciting the two transitions $g_1 \to e$ and $g_1 \to e$, respectively. (b) Fluorescence rate R_F as a function of the detuning Δ from the Raman resonance condition. Here ω_1 is resonant to the transition $g_1 \to e$.

the Raman resonance condition depends on the relaxation time in the ground state. Γ' is much smaller than the width Γ of the excited state.

The dark state can be written as

$$|\psi_\mathrm{NC}\rangle = c_1 |g_1\rangle + c_2 |g_2\rangle \,. \tag{4.5}$$

Here c_1 (c_2) is the probability amplitude for the atom being in state g_1 (g_2). The field-atom interaction is characterized by the Rabi frequencies

$$\Omega_i = -\mathbf{D}_{eg_i} \cdot \mathbf{E}_i/\hbar, \qquad i = 1, 2 \tag{4.6}$$

where $\mathbf{D}_{eg_i}$ is the matrix element of the dipole moment operator between e and g_i. For a dark state, the absorption amplitudes interfere destructively:

$$c_1\Omega_1 + c_2\Omega_2 = 0. \tag{4.7}$$

An atom remains in the dark state as long as the Raman resonance condition

$$E_{g_2} - E_{g_1} = \hbar\omega_1 - \hbar\omega_2 \tag{4.8}$$

is fulfilled. Furthermore, the dark resonance exists only if the two laser fields are coherent.

Velocity selective coherent population trapping

For a moving atom with velocity $\mathbf{v}$, the laser frequencies are Doppler shifted by $\mathbf{k}_1 \cdot \mathbf{v}$ and $\mathbf{k}_2 \cdot \mathbf{v}$, respectively. If $\mathbf{k}_1 \cdot \mathbf{v} \neq \mathbf{k}_2 \cdot \mathbf{v}$, $\psi_{\mathrm{NC}}(\mathbf{v})$ is no longer dark for $\mathbf{v} \neq \mathbf{0}$. Because a moving atom can absorb photons, coherent population trapping becomes velocity selective. As explained in Section 4.1.3 the atoms perform a random walk in momentum space and get trapped and accumulate in a small region near $\mathbf{p} = \mathbf{0}$.

4.1.5 Gray optical molasses

Sub-Doppler laser cooling using gray molasses was proposed in ref. [220–222] and realized in the mid '90s on the D_2 atomic transition of cesium and rubidium. Temperatures close to six times the single photon recoil energy [223–225] were reached. The scheme combines polarization-gradient cooling (see Section 4.1.2) with velocity-selective coherent population trapping (see Section 4.1.4). For an atomic ground state with angular momentum F, gray molasses operate on the $F \to F' = F$ ($F \to F' = F - 1$) optical transition. For any polarization of the local electromagnetic field, the ground state manifold possesses one (two) dark states which are not optically coupled to the excited state by the incident light [222, 226]. When the laser is detuned to the blue side of the resonance ($\omega_L > \omega_A$), the ground state manifold splits into dark states which are not affected by light and bright states which are light-shifted to positive energies by an amount which depends on the actual polarization and intensity of the laser field (see Fig. 4.6).

Dark states

In Section 4.1.2 we described how a bright molasses can reduce the temperature of an atomic sample below the Doppler- and even close to the recoil-limit. However, the cooling is accompanied by a reduction of the atomic density because of photon-exchange and resonant dipole-dipole interactions between the atoms [227, 228]. This limitation can be mitigated by using dark states [6] to reduce the atom-atom interactions. Dark states exist on any $F \to F$ or $F \to F - 1$ transition. [7] For simplicity, we consider the transition $1 \to 1$ in one dimension (see Fig. 4.5a). Suppose that the polarization of the light is σ_+. Then the state $|+1\rangle$ cannot be excited by the light. The same is true for the state $|-1\rangle$ for σ_- polarization and for the state $|0\rangle$ if the polarization is linear. For the latter case the Clebsch-Gordan coefficient is zero. We note that the light-polarization decides

[6] see Section 4.1.4 and [218]

[7] For an atom with transition $F \to F$ (F is integer) or $F \to F - 1$ in an arbitrary three-dimensional light field, at least one polarization independent dark state exists [229]

wether a state is a dark state or not. In general, there is always a linear combination of the lower states resulting in a dark state for a given light-polarization.

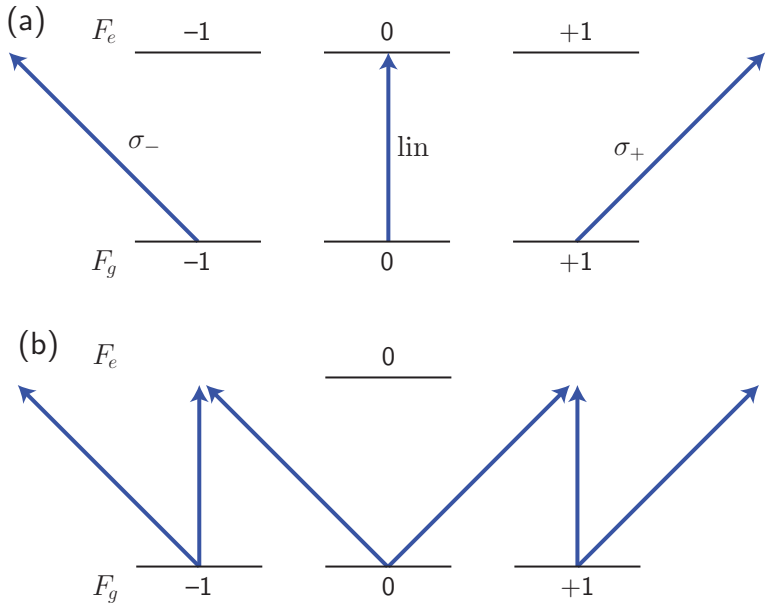

Figure 4.5: Dark states for a $F \to F$ and $F \to F-1$ transition. (a) $F \to F$: The atom interacts with σ_+, σ_- and π polarized light. In each case a pure state exists that can not be excited by the light. For an arbitrary polarization there always exists a linear combination of the lower states forming a dark state. (b) $F \to F-1$: For any polarization two dark states are present.

Cooling mechanism

Gray optical molasses combine Sisyphus cooling (see Section 4.1.2) and velocity selective coherent population trapping (see Section 4.1.4).

Figure 4.6 shows a scheme of the Sisyphus cooling mechanism in gray molasses. We consider an atom with two ground states, one bright state $|\Psi_{\mathrm{C}}\rangle$ and one dark state $|\Psi_{\mathrm{NC}}\rangle$, propagating in a one dimensional lin$\perp$lin laser configuration with low intensity. For blue laser detuning the light shift $\delta_C^{'}$ of $|\Psi_{\mathrm{C}}\rangle$ is positive. $\delta_C^{'}$ is proportional to the total intensity of the light field and hence spatially modulated. An atom in $|\Psi_{\mathrm{C}}\rangle$ is optically pumped to $|\Psi_{\mathrm{NC}}\rangle$, with the highest probability at the top of the light shift potential. The Sisyphus cycle is closed by motional coupling from $|\Psi_{\mathrm{NC}}\rangle$ to $|\Psi_{\mathrm{C}}\rangle$. An atom in $|\Psi_{\mathrm{NC}}\rangle$ is primarily transferred into the bright state in the valleys of the light shift potential, where the difference in energy between the two states is smallest [221]. On average the atom moves more uphill than downhill in the light shift potential of

$|\Psi_C\rangle$. Therefore, repetition of the optical pumping and motional coupling cycle reduces the kinetic energy of the atom.

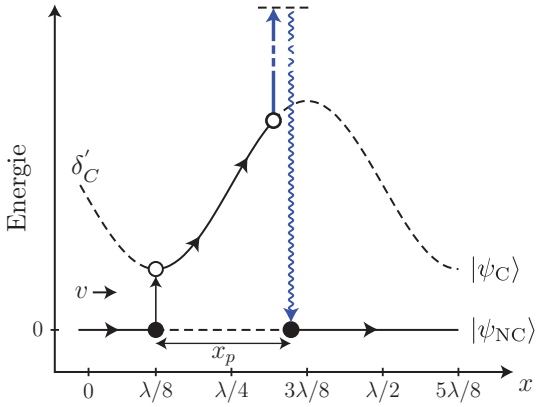

Figure 4.6: Sisyphus cooling in gray optical molasses. An atom with two ground states, one bright state $|\Psi_C\rangle$ and one dark state $|\Psi_{NC}\rangle$, propagates in a blue detuned one dimensional lin⊥lin laser configuration with low intensity. The light shift δ'_C of $|\Psi_C\rangle$ is positive and varies along x. An atom in $|\psi_{NC}\rangle$ is transferred to $|\psi_C\rangle$ by motional coupling, which is maximal at the potential minimum of $|\psi_C\rangle$. After propagating a distance x_p in the bright state, the atom is optically pumped back to $|\psi_{NC}\rangle$, with the highest probability at the potential hill. Repetition leads to cooling, because on average the atom moves more uphill than downhill.

The departure rate from $|\Psi_{NC}\rangle$, induced by motional coupling, varies with the square of the atom velocity [221]. Therefore, during the Sisyphus cooling, slow atoms get trapped in $|\Psi_{NC}\rangle$, which leads to a diminished fluorescence rate (see Section 4.1.4). The accumulation of atoms in dark states is favorable because it reduces the photon-exchange and resonant dipole-dipole interactions between the atoms and enables the production of cold and dense atomic samples [223–225].

4.2 D_1 sub-Doppler laser cooling

Parts of this section are based on the following manuscripts:

Sub-Doppler laser cooling of fermionic ^{40}K atoms in three-dimensional gray optical molasses
D. R. Fernandes [a], F. Sievers [a], N. Kretzschmar, S. Wu, C. Salomon, and F. Chevy
EPL (Europhysics Letters) **100**, 63001 (2012)

[a] These authors contributed equally to this work.

Simultaneous D_1 line sub-Doppler laser cooling of fermionic ^{6}Li and ^{40}K
F. Sievers, N. Kretzschmar, S. Wu, D. R. Fernandes, D. Suchet, M. Rabinovic, L. Khaykovich, C. Salomon, and F. Chevy
To be published

Sub-Doppler cooling has proven to be a powerful technique to increase the phase-space density of atomic samples [137]. However, cooling lithium and potassium using optical transitions is difficult compared to the other alkali-metal atoms. The small separation of the excited-state structure of the D_2 transition, compromises the efficiency of standard sub-Doppler cooling techniques such as polarization gradient cooling [137–139].
The excited-state hyperfine splitting on the D_1 transition is large compared to the D_2 transition (see Fig. 2.2). Therefore, we developed a sub-Doppler cooling mechanism, operating on the D_1 transition, to simultaneous cool fermionic ^{6}Li and ^{40}K [140, 141]. In the following we make use of the simple pictures of laser cooling mechanisms introduced in the previous section to develop an intuitive picture of the D_1 sub-Doppler cooling mechanism.

4.2.1 ^{40}K D_1 molasses

We restrict the discussion of the cooling mechanism to the case of ^{40}K. The same picture is valid for ^{6}Li.

D_1 sub-Doppler laser cooling scheme

We implement 3D gray molasses cooling in ^{40}K on the D_1 transition (see Fig. 4.7). In alkali atoms, the $P_{1/2}$ excited level manifold has only two hyperfine states, which are better resolved than their $P_{3/2}$ counterparts (see Fig. 2.2). These facts allow for less off-resonant excitation and a good control of the cooling mechanism. A first laser beam (cooling beam) is tuned to the $\left|4^2S_{1/2}, F = 9/2\right\rangle \rightarrow \left|4^2P_{1/2}, F' = 7/2\right\rangle$ transi-

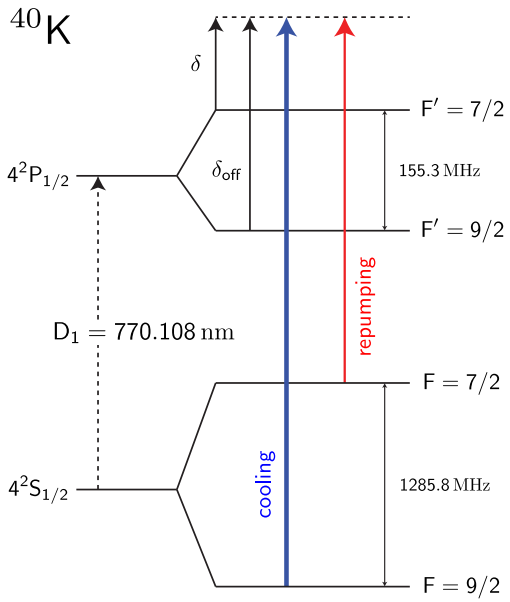

Figure 4.7: Level scheme for the D_1 transition of ^{40}K and transitions used for gray molasses cooling. The laser detuning from the cooling/repumping transitions is δ and the detuning from the off-resonant excited hyperfine state $F' = 9/2$ is δ_{off}.

tion with a detuning $\delta > 0$. A second laser beam (repumping beam) is tuned to the $\left|4^2S_{1/2}, F = 7/2\right\rangle \rightarrow \left|4^2P_{1/2}, F' = 7/2\right\rangle$ transition with the same detuning δ, hence fulfilling the Raman-condition (see Section 4.1.4).

The cooling transition and the blue detuned cooling beam fulfill the condition for gray molasses cooling, described in Section 4.1.5. Furthermore the repumping beam coherently couples the $\left|4^2S_{1/2}, F = 9/2\right\rangle$ and the $\left|4^2S_{1/2}, F = 7/2\right\rangle$ ground state manifolds. The formed Λ-system $\{g_1 = |F = 9/2\rangle,\ g_2 = |F = 7/2\rangle,\ e = |F' = 7/2\rangle\}$, leads to a second class of dark states (see Section 4.1.4), enhancing the cooling efficiency.

In Section 4.1.5 the Sisyphus cycle in gray molasses is established by optically pumping atoms from a bright- in a dark state, $|\psi_{\text{C}}\rangle \rightarrow |\psi_{\text{NC}}\rangle$, whose departure rate is induced by motional coupling V_{mot}. In motional coupling, polarization- and intensity gradients lead to a spatial variation of the dark state's internal wave-function and mix a part of the radiative instability of $|\psi_{\text{C}}\rangle$ to $|\psi_{\text{NC}}\rangle$.

On the D_1 transition of alkali atoms a second mechanism leads to the departure from the dark state: The dipolar coupling V_{off} via the off-resonant excited hyperfine state (see Fig. 4.7). Therefore, the total departure rate becomes $\left|\langle\psi_{\text{C}}| V_{\text{mot}} + V_{\text{off}} |\psi_{\text{NC}}\rangle\right|^2$. A rough estimate shows that $V_{\text{mot}} \simeq \hbar k v$, where v is the velocity of the atom and k the wave-vector of the cooling light, while $V_{\text{off}} \simeq \hbar\Gamma\left(\Gamma/\delta_{\text{off}}\right) I/I_{\text{sat}}$, where Γ^{-1} is the lifetime of

the excited state, I the light intensity, I_{sat} the saturation intensity and δ_{off} the detuning to off-resonant excited states. Comparing the two couplings, we see that the motional coupling is significant in the high velocity regime $v \gtrsim \Gamma/k\,(\Gamma/\delta_{\mathrm{off}})\,I/I_{\mathrm{sat}}$. In our case, the off-resonant level $F' = 9/2$ (see Fig. 4.7) is detuned by $\delta_{\mathrm{off}} = 155.3\,\mathrm{MHz} + \delta$ from the cooling transition $\left|^2S_{1/2}, F = 9/2\right\rangle \rightarrow \left|^2P_{1/2}, F' = 7/2\right\rangle$. For $I \simeq I_{\mathrm{sat}}$, motional coupling dominates for $T \gtrsim 50\,\mu\mathrm{K}$. In general, the transition rate between $|\psi_{\mathrm{NC}}\rangle$ and $|\psi_{\mathrm{C}}\rangle$ induced by motional coupling V_{mot} and the off-resonant coupling V_{off} are both maximal when the distance between the dark and bright manifolds is smallest, which favors transitions near the bottom of the wells of the optical lattice.

In ^{40}K, the simplified discussion presented so far must be generalized to the case involving many hyperfine states $(10 + 8)$. However, the essential picture remains valid. By numerically solving the optical Bloch equations for the ^{40}K system in the presence of the cooling and repumping laser fields, we obtain the light shifts ϵ and the total optical pumping rates γ of all the dressed states for an atom at rest (see Fig. 4.8). This is done for the particular case of a one-dimensional optical lattice in the lin$\perp$lin configuration and with a low repumping intensity (1/8 of the cooling beam intensity, typical for our experiments). [8] In Fig. 4.8a we see 8 bright states, 2 weakly coupled states and 8 nearly dark states combining both ground-state hyperfine manifolds. In Fig. 4.8b we plot the optical pumping rates γ of the corresponding dressed states. We find that the optical pumping rate is low for the weakly coupled states and it practically vanishes for the long-lived dark states. In Fig. 4.8c the optical pumping rates display a good correlation with the light shift magnitude, which favors efficient sub-Doppler cooling. This correlation shows that the gray molasses picture remains valid for this more complex level scheme. Note, that in contrast to the simplified gray optical molasses scheme, there is no polarization independent dark state for an atom at rest, due to off-resonant couplings. Instead we only find local dark states, emerging for specific polarizations. This leads to reduced dark periods, and therefore VSCPT is compromised. However, VSCPT is just a bonus to minimize the density dependent heating. The key to efficient sub-Doppler cooling is the establishment of a correlation between population and light shifts for atoms traveling with a velocity $kv \lesssim \gamma$. The establishment of a correlation is favored on the D_1 line, because in contrast to the D_2 line that contains "closed" transitions, the optical transitions are all "open". When subjected to off-resonant D_1 laser couplings, atoms tend to leave a particular dressed ground-state quicker if the particular dressed state is coupled

[8] The code has been developed by Saijun Wu, Department of Physics, College of Science, Swansea University, Swansea SA2 8PP, United Kingdom

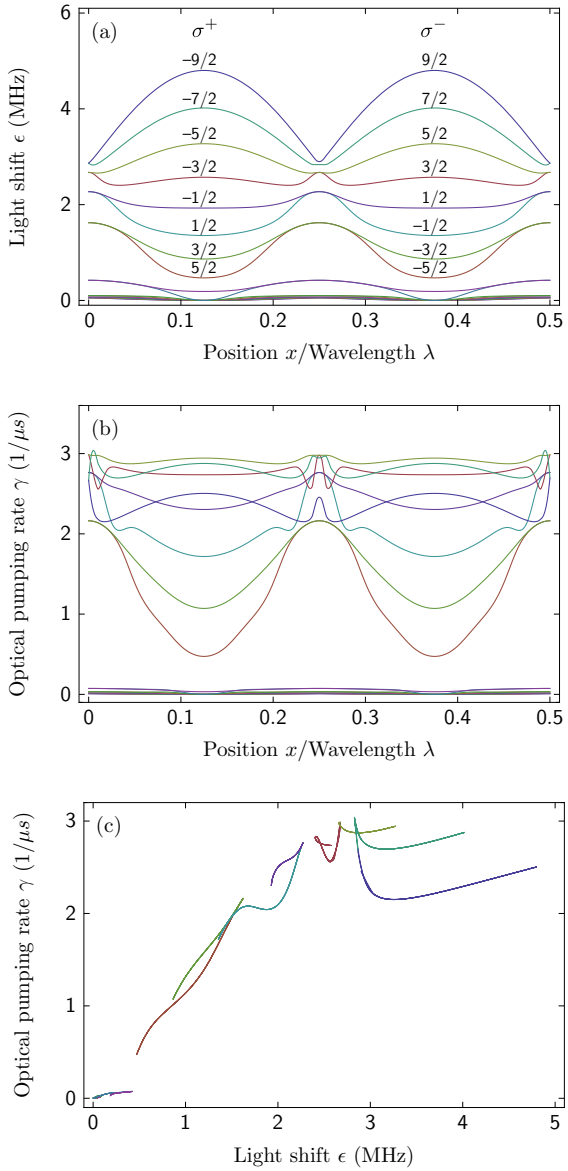

Figure 4.8: Semi-classical calculation of the effect of dual frequency counter-propagating laser beams in a 1D lin⊥lin configuration on a ^{40}K atom at rest. (a) Light shifts ϵ versus position. (b) Optical pumping rates γ versus position. (c) Optical pumping rates versus light shifts. The laser intensities are $I_{\text{cool}} = 20I_{\text{sat}}$ and $I_{\text{rep}} = I_{\text{cool}}/8$ per beam, with $\delta = +3\Gamma$. The different lines correspond to the 18 dressed states of the $\left|^2S_{1/2}\right\rangle$ ground-state. At $z = \lambda/8$ the local polarization is σ^+ and here each curve corresponds to a pure m_F state. At this position the light shift increases with $-m_F$. The $\left|^2S_{1/2}, F = 7/2\right\rangle$ manifold interacts only weakly with light since the repumping beam is kept at low intensity. Consequently, the light shifts and optical pumping rates are small.

more strongly to the laser field. This explains the robustness and efficiency of the D_1 sub-Doppler cooling.

We now turn to the question of the capture velocity of the gray molasses scheme. The atom is pumped efficiently towards dark states if it stays a time $\tau \gtrsim \gamma^{-1}$ near the top of the hill. If the atom moves at a velocity v in the lattice, then $\tau \simeq 1/kv$ and the optical pumping to dark states is efficient when $kv \lesssim \gamma$. $v_c \simeq \gamma/k$ thus defines the capture velocity of the gray molasses. For a beam with detuning δ to the main cooling transition, $\gamma \propto I/\delta^2$ and thus v_c increases with laser intensity. On the other hand, the cooling efficiency is reduced when the atom cannot climb the potential hill anymore, which leads to an equilibrium temperature that scales as $k_B T \propto I/\delta$, when $T \gg T_{\mathrm{Recoil}} = \hbar^2 k^2/2mk_{\mathrm{B}}$ [137, 230].

Experimental results

In the experiments presented here, 6.5×10^8 ^{40}K atoms are loaded from a 2D-MOT (see Section 2.5) into a three-dimensional MOT operating on the D_2 line (see Section 2.6). The initial temperature of the cloud is $240\,\mu$K, not far from the Doppler temperature $T_D = \hbar\Gamma/2k_{\mathrm{B}} = 145\,\mu$K, with $\Gamma/2\pi \approx 6.035\,$MHz. In the MOT, the cooling and repumping laser intensities are $I_{\mathrm{cool}} = 13 I_{\mathrm{sat}}$ and $I_{\mathrm{rep}} = I_{\mathrm{cool}}/20$ per beam, with $I_{\mathrm{sat}} = 1.75\,\mathrm{mW/cm^2}$. The detuning of the cooling and repumping light is $\delta\omega_{\mathrm{cool}} = -3\,\Gamma$ and $\delta\omega_{\mathrm{rep}} = -5\,\Gamma$, respectively. After the loading phase, we ramp the magnetic field gradient from $9\,\mathrm{G{\cdot}cm^{-1}}$ to $60\,\mathrm{G{\cdot}cm^{-1}}$ in 5 ms without changing the laser detunings in order to compress the cloud. This process yields a cloud with high density, but with a much higher temperature of $\sim 4\,$mK. At this point the magnetic field is switched off in $\simeq 100\,\mu s$ and the D_1 molasses beams are switched on for a time τ_{m}.

The D_1 cooling and repumping beams are detuned by the same amount δ in the range of $2\Gamma - 5\Gamma$ as shown in Fig. 4.7. The repumping beam is detuned from the main cooling beam by 1285.8 MHz using an electro-optical modulator (see Fig. 2.11). Its intensity is typically 1/8 of the cooling beam intensity. After propagation through an optical fiber, the total D_1 optical power is 240 mW and the beam is magnified to a $1/e^2$-diameter of 17.8 mm. We then split the beam into two vertical beams and two retro-reflected horizontal beams in a three-dimensional σ^+/σ^- configuration (see Fig. 2.12). The maximum D_1 cooling intensity per beam attained in our experiments is $25\,\mathrm{mW/cm^2}$ or $I = 14.7 I_{\mathrm{sat}}$.

We first measure the atom number and temperature of the D_1 molasses as a functions of the cooling beam duration τ_{m} (Fig. 4.9). The temperature is determined by time-of-flight measurements. At high intensity $I_{\mathrm{cool}} = 14.7 I_{\mathrm{sat}}$ and detuning $\delta = 2.3\Gamma$, all 4.5×10^8 compressed MOT atoms are cooled to a temperature of $30\,\mu$K in 6 ms. For

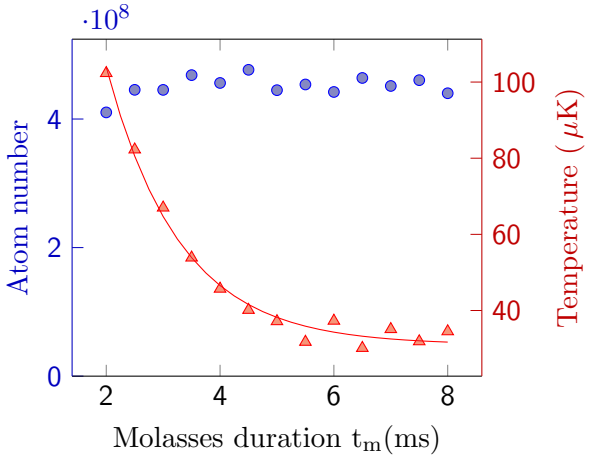

Figure 4.9: Number of atoms captured in the ^{40}K D_1 molasses (circles) and their temperature (triangles) as functions of molasses duration. All 4.5×10^8 compressed MOT atoms are cooled from 4 mK to a temperature of 30 μK in 6 ms. $I_{\text{cool}} = 14.7 I_{\text{sat}}$, $\delta = 2.3\Gamma$ and $I_{\text{rep}} = I_{\text{cool}}/8$.

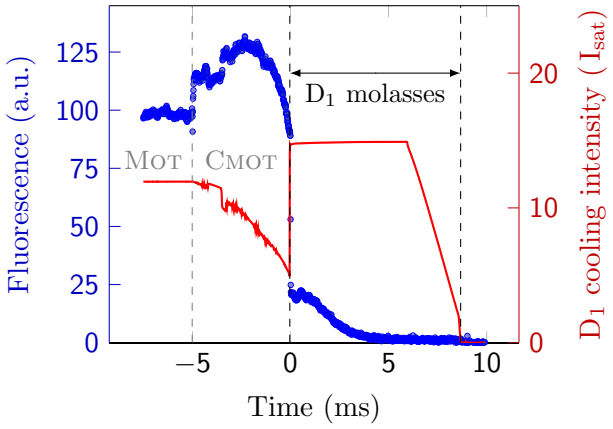

Figure 4.10: Measured fluorescence during the MOT, CMOT and the D_1 molasses phases (blue) for ^{40}K. The D_1 cooling intensity (Time>0, red) stays constant for 6 ms, $I_{\text{cool}} = 14.7 I_{\text{sat}}$, and is linearly ramped to $0.8\, I_{\text{sat}}$ in 3 ms. $\delta = 2.3\Gamma$ and $I_{\text{rep}} = I_{\text{cool}}/8$.

these parameters we measure a D_1 molasses lifetime of 500 ms. Although the initial temperature of the compressed MOT is rather high, D_1 cooling occurs rapidly. The temperature drops from ~ 4 mK to 100 μK in 2 ms, and reaches 30 μK in about 6 ms. This dynamics is confirmed by direct measurement of the fluorescence light emitted during the D_1 molasses phase (see Fig. 4.10. The fluorescence exhibits a fast decay in $\sim 3\,\mu$s to about 20% of the MOT fluorescence followed by a slower decay in ~ 4 ms to $\sim 1\%$, which indicates the accumulation of atoms in weakly coupled states. When repeating

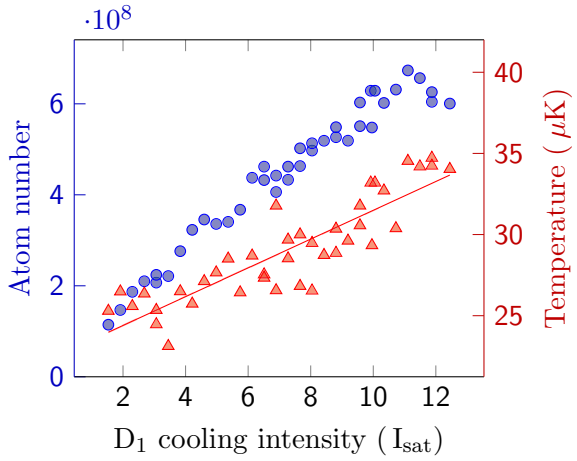

Figure 4.11: Number of atoms captured in the D_1 molasses (circles) and their temperature (triangles) as a function of the ^{40}K D_1 cooling beam intensity for $\delta = 2.3\Gamma$ and $I_{\mathrm{rep}} = I_{\mathrm{cool}}/8$. The number of atoms in the compressed MOT was 6.5×10^8 and the capture efficiency reaches $\sim 100\%$ for $I \geq 11 I_{\mathrm{sat}}$

the experiment for lower D_1 laser intensities for a fixed time of 6 ms, we observe both a decrease of the number of atoms cooled by gray molasses and a further lowering of the temperature down to 24 μK (Fig. 4.11). The number of atoms is measured after a time of flight of 20 ms, after which we would not detect any atoms in the absence of D_1 molasses. The capture efficiency increases with the cooling intensity indicating a higher capture velocity at higher laser intensity and it reaches $\sim$ 100% for $I \geq 11 I_{\mathrm{sat}}$. Similarly, the equilibrium temperature increases with laser intensity in the explored range in agreement with Sisyphus-type cooling mechanisms. The results of Fig. 4.9 and Fig. 4.11 suggest implementing a cooling sequence with two successive phases. A first phase lasting 6 ms at high D_1 cooling intensity takes advantage of the high capture velocity. This phase is followed by a 3 ms stage in which the intensity is linearly reduced by an adjustable amount to further lower the temperature. As illustrated in Fig. 4.12, this supplementary cooling phase allows the sample to reach a temperature of 20 μK by reducing the intensity

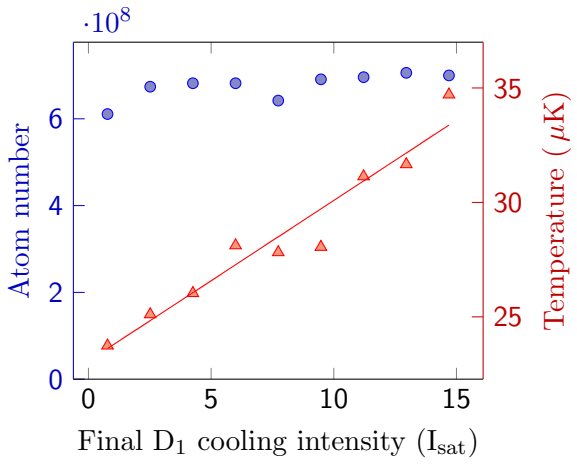

Figure 4.12: Number of atoms captured in the ^{40}K D_1 molasses (circles) and their temperature (triangles) after a 6 ms capture phase at high intensity $I_{\text{cool}} = 14.7 I_{\text{sat}}$ followed by a 3 ms linear intensity ramp to adjustable value. The detuning is fixed to $\delta = 2.3\Gamma$. We find the minimum temperature for $I_{\text{cool,final}} = 0.8 I_{\text{sat}}$.

by one order of magnitude and without any atom loss. No significant change of the atomic cloud volume was observed during this 9 ms sequence. In Fig. 4.13, we show the number of atoms captured in the D_1 molasses and their temperature as a function of the laser detuning δ for the complete 9 ms sequence. For $\delta \in [0.5\Gamma, 2\Gamma]$, we observe a steep decrease of the temperature from 100 μK to 30 μK, as expected from Sisyphus cooling, followed by a plateau near 30 μK for detunings above 2Γ. The capture efficiency raises sharply to $\sim 100\%$ at $\delta \sim 2.3\Gamma$, displays a broad maximum and slowly decreases above 4Γ, indicating a decrease of the capture velocity.

We have also scanned the intensity and the detuning of the repumping laser. We observe a very weak dependence of the molasses temperature and capture fraction upon repumping intensity. On the other hand, when scanning the repumping detuning, we observe that cooling is optimal within 300 kHz from the exact Raman-condition. This points to the existence of long-lived coherences between the two hyperfine manifolds $\left|^2S_{1/2}, F = 9/2\right\rangle$ and $\left|^2S_{1/2}, F = 7/2\right\rangle$, resulting in the formation of new inter-manifold dark states and is investigated in Section 4.2.3. Finally, optimal parameters for ^{40}K gray molasses are summarized in Table 4.1.

We also searched for a density dependent temperature limitation. Figure 4.14 shows the temperature of the D_1 molasses as a function of the peak atomic density for a linear intensity ramp to $I_{\text{cool,final}} = 4 I_{\text{sat}}$. The temperature increases linearly with the peak atomic density , $\Delta T \approx 4.6\,\mu\text{K} \times 10^{10}\,\text{at./cm}^3$.

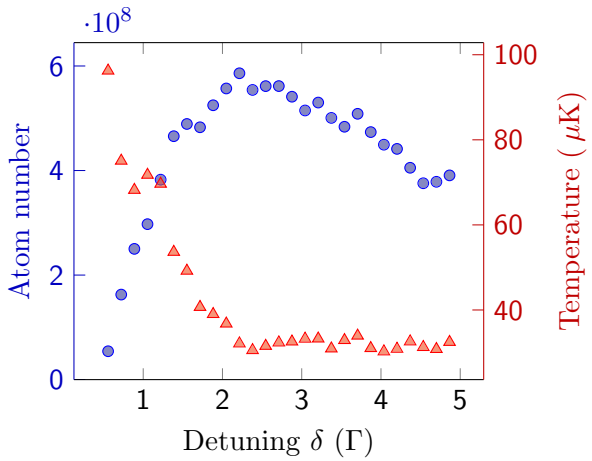

Figure 4.13: Number of atoms captured in the ^{40}K D_1 molasses (circles) and their temperature (triangles) for the dynamic 9 ms cooling sequence as a function of the detuning δ. The number of atoms in the compressed MOT is 6×10^8.

	Duration (ms)	$I_{\mathrm{cool}}(I_{\mathrm{sat}})$	$\delta(\Gamma)$
Capture phase	6	14.7	+2.3
Cooling phase	3	14.7→0.8	+2.3

Table 4.1: Optimized parameters for ^{40}K D_1 gray molasses. Using these parameters, all the 6.5×10^8 atoms from a compressed MOT are cooled to 20 μK in D_1 gray molasses.

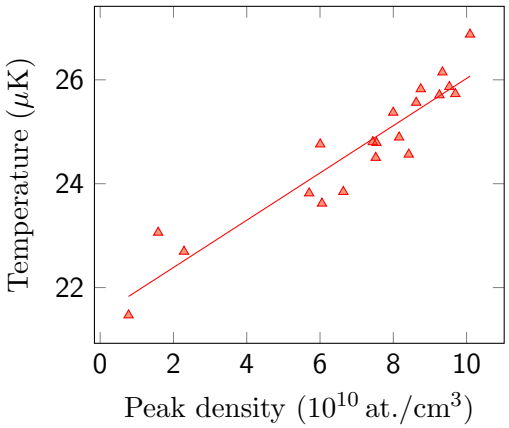

Figure 4.14: ^{40}K D_1 molasses temperature as a function of the peak atomic density for $I_{\mathrm{cool,final}} = 4I_{\mathrm{sat}}$ and $\delta = 2.3\Gamma$

.

The residual magnetic fields during the D_1 molasses have to be compensated to minimize the temperature. For the presented results we used nearby coils for this purpose, namely the anti Zeeman slower coil, the pushing coil for the magnetic transport and the spin-polarization coils. After installing new compensation coils that provide a more homogeneous field we were able to cool 3.2×10^9 ^{40}K atoms to a temperature of $\sim 11\,\mu$K. Figure 4.15 shows the ^{40}K molasses temperature as a function of a vertical magnetic field bias B_z. The D_1 molasses temperature increases quadratically as $\Delta T \approx 56\,\mathrm{B}^2\mu\mathrm{K/G}^2$.

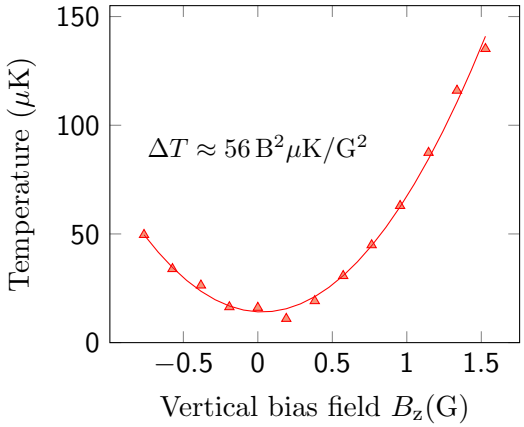

Figure 4.15: ^{40}K D_1 molasses temperature as a function of a vertical magnetic field bias B_z. The temperature has a minimum of $\sim 11\,\mu$K and increases quadratically with $\Delta T \approx 56\,\mathrm{B}^2\mu\mathrm{K/G}^2$. The number of atoms in the molasses is 3.2×10^9.

Summary

We have shown that gray molasses operating on the D_1 optical transition is a very simple and powerful method to increase the phase space density of laser-cooled ^{40}K alkali gases to $\sim 10^{-4}$. This phase space density leads to excellent starting conditions for evaporative cooling in magnetic or optical dipole traps. For ^{40}K, this is particularly useful as the low temperature allows direct transfer into an optical trap and magnetic tuning to a Feshbach resonance for efficient evaporation. In the next section, we present the D_1 molasses cooling of ^{6}Li in single-species operation.

4.2.2 ^{6}Li D_1 molasses

The bichromatic D_1 cooling scheme for ^{6}Li is depicted in Fig. 4.16. Similar to ^{40}K, the cooling scheme involves three-dimensional standing waves in a Λ-configuration. The cooling beam is tuned to the $\left|2^2S_{1/2}, F = 3/2\right\rangle \rightarrow \left|2^2P_{1/2}, F' = 3/2\right\rangle$ transition with a detun-

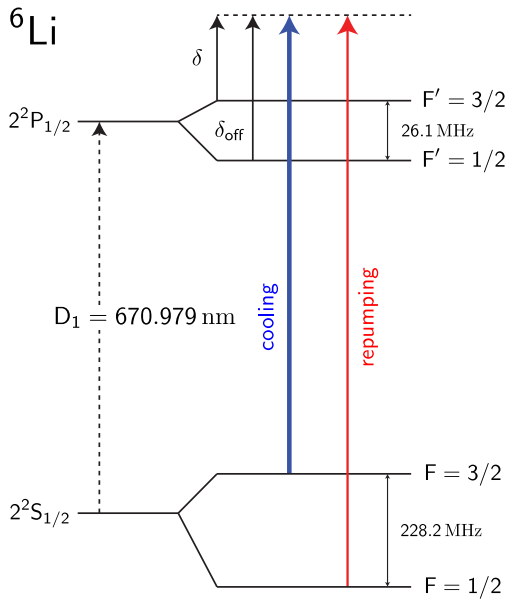

Figure 4.16: D_1 cooling scheme for ^{6}Li. The laser detuning from the cooling/repumping transitions is δ and the detuning from the off-resonant excited hyperfine state $F' = 1/2$ is δ_{off}.

ing $\delta > 0$. The repumping beam is tuned to the $\left|2^2S_{1/2}, F = 1/2\right\rangle \rightarrow \left|2^2P_{1/2}, F' = 3/2\right\rangle$ transition with the same detuning δ, fulfilling the Raman-condition.

Here we describe the D_1 cooling of ^{6}Li in single species operation. We set the peak intensity of the molasses to 14.6 I_{sat} per beam, the cooling/repumping ratio to $I_{\text{cool}}/I_{\text{rep}} = 20$ and fix the global detuning to $\delta = 4\,\Gamma$. $I_{\text{sat}} = 2.54\,\text{mW/cm}^2$ is the saturation intensity of the D_2 cycling transition and $\Gamma = 2\pi \times 5.87\,\text{MHz}$ the D_1 line natural linewidth for ^{6}Li. The molasses beams are switched on after the CMOT phase with a delay of 200μs, to make sure that the magnetic field of the MOT coils is zero.

Fig. 4.17 shows the atom number and temperature of the D_1 molasses as functions of the molasses duration t_{m}. The temperature is determined through time of flight measurements. We capture 60 % of the 8×10^8 CMOT atoms. Within 3 ms the atoms are cooled from 800 μK to the asymptotic temperature of 120 μK with a $1/e$ cooling time constant $\tau_{\text{cool}} = 0.6\,\text{ms}$. We find the 1/e-lifetime of the D_1 molasses atom number for these parameters to be $\tau_{\text{D1}} = 90\,\text{ms}$.

Figure 4.18 shows the direct measurement of the fluorescence. The fluorescence signal on the photodiode decays from 40 mV to 12.5 mV in 2 ms at full D_1 cooling intensity, followed by a further decrease to 7.5 mV in 1 ms while the D_1 cooling intensity is linearly ramped to a final value of 10 I_{sat}. This indicates that the atoms are accumulated in dark

states during the cooling process. However, the accumulation in dark states is not as efficient as for ^{40}K (see Fig. 4.10).

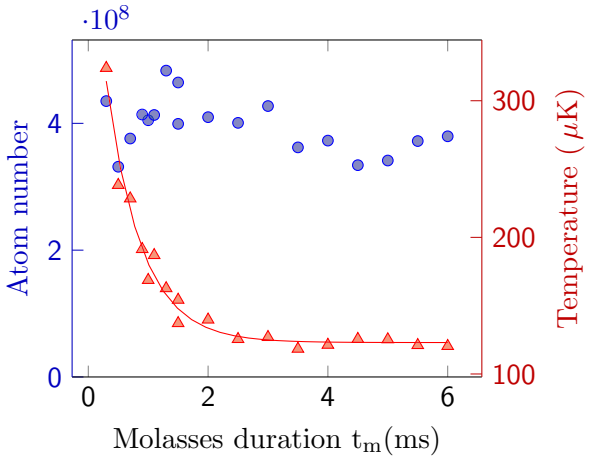

Figure 4.17: Number of atoms captured in the ^{6}Li D_1 molasses (circles) and their temperature (triangles) as functions of molasses duration, with a $1/e$ cooling time constant $\tau_{\text{cool}} = 0.6\,\text{ms}$. The number of atoms in the compressed MOT is 8×10^8.

The molasses atom number and temperature as functions of the global detuning δ is shown in Fig. 4.19. We observe a decrease of the temperature from 188 μK to 100 μK for $\delta = 2 \ldots 7$. The capture efficiency raises sharply until $4\,\Gamma$ and stays constant until $7\,\Gamma$.

We now study the influence of the D_1 light intensity. When increasing the cooling intensity, while keeping the molasses time fixed to 3 ms, we observe both an increase of the capture efficiency and of the temperature (see Fig. 4.20).

As for ^{40}K, we use two successive phases in the cooling sequence. During the first 3 ms we capture the atoms at high intensity, yielding the highest capture efficiency. Then the intensity is linearly ramped within 2 ms to an adjustable final intensity to further lower the temperature. Fig. 4.21 shows that the intensity ramp reduces the final temperature from 115 μK to 44 μK without a significant atom loss for a final intensity $I_{\text{cool,final}} = 2.5 I_{\text{sat}}$. For lower intensities we observe heating and atom loss. The cooling/repumping intensity-ratio influences the atom number and the temperature. We find an optimal temperature for $I_{\text{cool}}/I_{\text{rep}} = 20$. For a smaller ratio the temperature increases slightly and the atom number starts to drop at around $I_{\text{cool}}/I_{\text{rep}} = 7$. For $I_{\text{cool}}/I_{\text{rep}} > 33$ the cooling mechanism becomes inefficient, leading to atom loss and heating.

Measuring the atom cloud size at the end of the CMOT and molasses phases we see no significant change, proving that the diffusion during the molasses phase is small. In

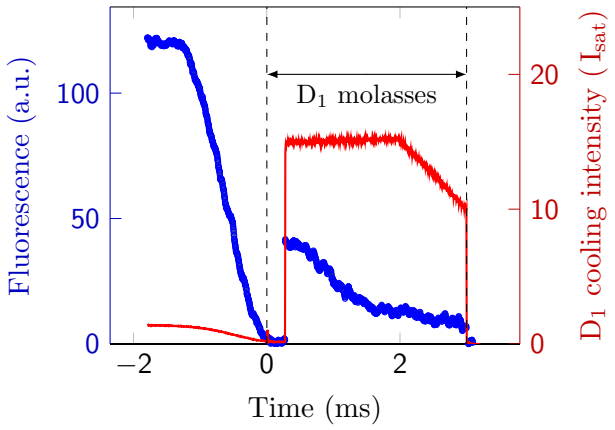

Figure 4.18: Measured fluorescence during the CMOT and the D_1 molasses phases (blue) for ^{6}Li. The D_1 cooling intensity (red) stays constant for 2 ms $I_{cool} = 14.6\, I_{sat}$, and is linearly ramped to $10\, I_{sat}$ in 1 ms. $\delta = 4\Gamma$ and $I_{rep} = I_{cool}/8$.

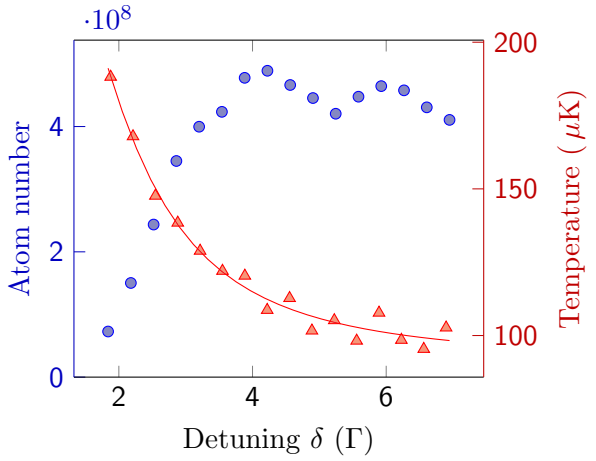

Figure 4.19: Number of atoms captured in the ^{6}Li D_1 molasses (circles) and their temperature (triangles) after a 3 ms capture phase at high intensity $I_{cool} = 14.6\, I_{sat}$ as functions of the global detuning $\delta = \delta = \delta_{rep}$. The number of atoms in the compressed MOT is 8×10^8.

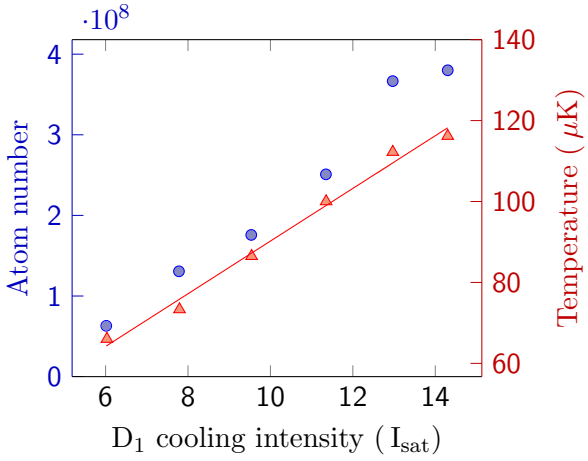

Figure 4.20: Number of atoms captured in the ^{6}Li D_1 molasses (circles) and their temperature (triangles) as functions of the D_1 cooling beam intensity for $\delta = 4\,\Gamma$ and $I_{\mathrm{rep}} = I_{\mathrm{cool}}/20$. The number of atoms in the compressed MOT is 8×10^8. The atom number (temperature) increases linearly with a slope of 4×10^7 atoms/$\mathrm{I_{sat}}$ ($6.5\,\mu\mathrm{K}/\mathrm{I_{sat}}$).

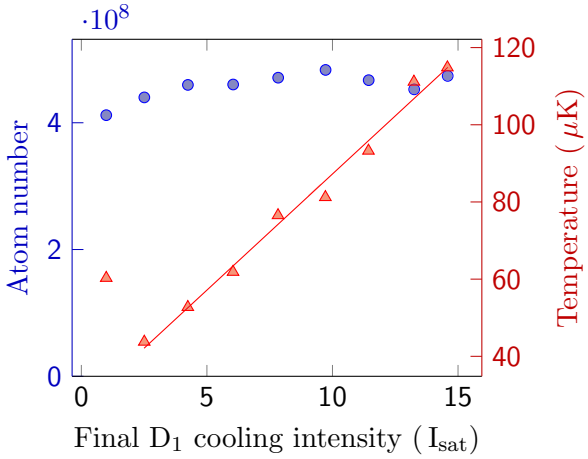

Figure 4.21: Number of atoms captured in the ^{6}Li D_1 molasses (circles) and their temperature (triangles) after a 3 ms capture phase at high intensity $I_{\mathrm{cool}} = 14.6 I_{\mathrm{sat}}$ followed by a 2ms linear intensity ramp to an adjustable value. The temperature increases linearly for larger intensity with a slope of $\sim 6\,\mu\mathrm{K}/\mathrm{I_{sat}}$ The detuning is fixed to $\delta = 4\,\Gamma$. The number of atoms in the compressed MOT is 8×10^8.

terms of phase-space density the atom loss is largely overcompensated by the 14 times reduction in temperature.

4.2.3 Raman-detuning dependance

So far our studies were limited to the case of zero Raman-detuning. When the Raman-resonance condition is fulfilled, the relative detuning of the cooling and repumping frequencies with respect to the highest excited hyperfine level is zero. In this section we investigate the influence of the Raman-detuning $\Delta = \delta_{\mathrm{rep}} - \delta_{\mathrm{cool}}$ on the cooling dynamics. The cooling schemes for both ^{6}Li and ^{40}K, including the Raman-detuning are shown in Fig. 4.22.

We compare the experimental data with numerical simulation, developed by Saijun Wu [9], that are based on a semi-classical MonteCarlo wavefunction method. The simulation takes into account the three dimensional optical molasses setup and the vectorial interaction between the polarized light and single atoms at the D_1 manifold spanned by the $4(2I+1)$ hyperfine Zeeman sub-levels ($I > 0$ is the nuclear spin). To mimic the experimental situation, we fix the relative phases for all six cooling and repumping laser beams at randomized values for each simulation trial. We record the evolution of the 3D atomic velocity as well as time-stamped fluorescence events, corresponding to quantum jumps. These quantities are then averaged over multiple simulation trials for comparison with the experiment.

Raman-detuning dependance for ^{6}Li

We begin the study of the Raman-detuning dependence with ^{6}Li. In the following we investigate the Raman-detuning dependent molasses temperature and fluorescence rate at various cooling and repumping laser intensities.

In the simulation we set the initial velocity of lithium to 0.2 m/s ($T \sim 30\ \mu$K) and the simulation time to 200 μs. For the last 100 μs we record the velocity $\mathbf{v}(t)$ as well as the time-stamped quantum jump events for calculating the fluorescence rate. At each Raman-detuning we average over 25 trajectories. The simulation results for two different intensities $I_{\mathrm{cool}} = 2.7\, I_{\mathrm{sat}}$, $I_{\mathrm{rep}} = 0.13\, I_{\mathrm{sat}}$ and $I_{\mathrm{cool}} = 9\, I_{\mathrm{sat}}$, $I_{\mathrm{rep}} = 0.46\, I_{\mathrm{sat}}$ are shown in Fig. 4.23c and Fig. 4.23d respectively.

The first measurements we performed, showed that the ^{6}Li D_1 molasses only worked for small Raman-detunings, if the repumping frequency was detuned during the complete molasses phase. At $|\Delta| \sim 0.2\,\Gamma$ the observed detrimental heating was already so pronounced that all the atoms were lost after a D_1 molasses duration of 5 ms. Therefore,

[9] Department of Physics, College of Science, Swansea University, Swansea SA2 8PP, United Kingdom

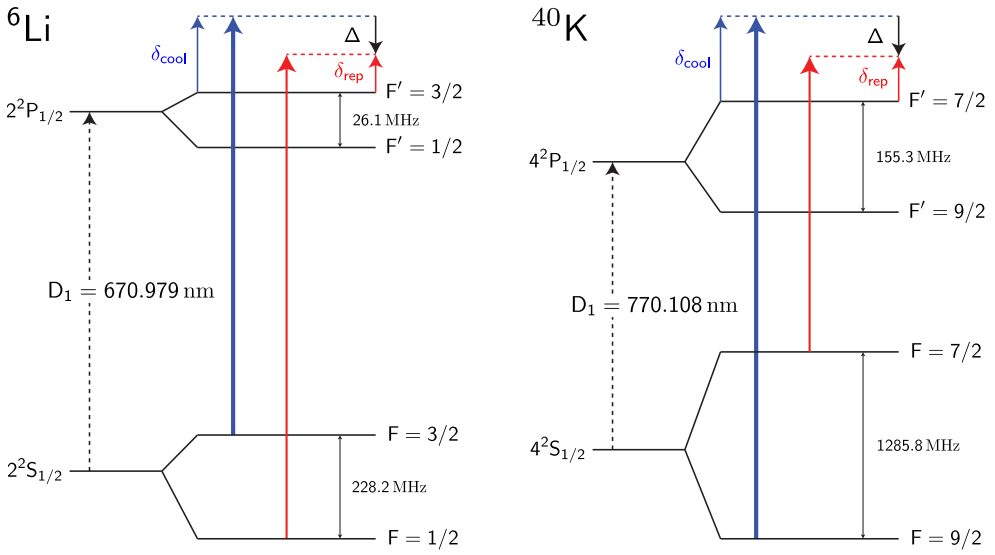

Figure 4.22: Cooling scheme on the ^{6}Li and ^{40}K D_1 line including the detuning from the Raman-condition, denoted by $\Delta = \delta_{rep} - \delta_{cool}$.

we implemented a D_1 pre-cooling phase, where we performed standard D_1 cooling with $\Delta = 0$, before performing the actual measurement with a Raman-detuning different from zero.

In the corresponding experiments we apply a 100 μs D_1 molasses pulse with variable Δ to an atomic cloud precooled to 100 μK. This allow us to measure the heating rate induced by the molasses pulse with Raman-detuned repumping frequency.

Fig. 4.23a,b show the fluorescence rate and the temperature after the pulse as functions of the Raman-detuning Δ for the intensities used in the simulation. We observe a temperature dip at zero Raman-detuning and a heating/fluorescence peak at positive Δ with its position and amplitude correlated to the molasses intensity.

The simulated heating/fluorescence peak positions for low and high intensities (Fig. 4.23) agree with the experimental findings. Also the shift between the heating and fluorescence peak, which increases with intensity, is numerically reproduced. However the simulation clearly underestimates the temperature particularly near the Raman-resonance $\Delta = 0$. This is expected, because in the semi-classical simulation there are multiple local dark states within an unit-cell of the bi-chromatic gray molasses that easily trap very slow ^{6}Li atoms. This leads to very low temperatures particularly for $\Delta \sim 0$. However, the wave nature of external motion reduces the lifetime of these dark periods due to the wave packet spreading and therefore significantly increases the achievable lowest temperatures from the classical particle limit.

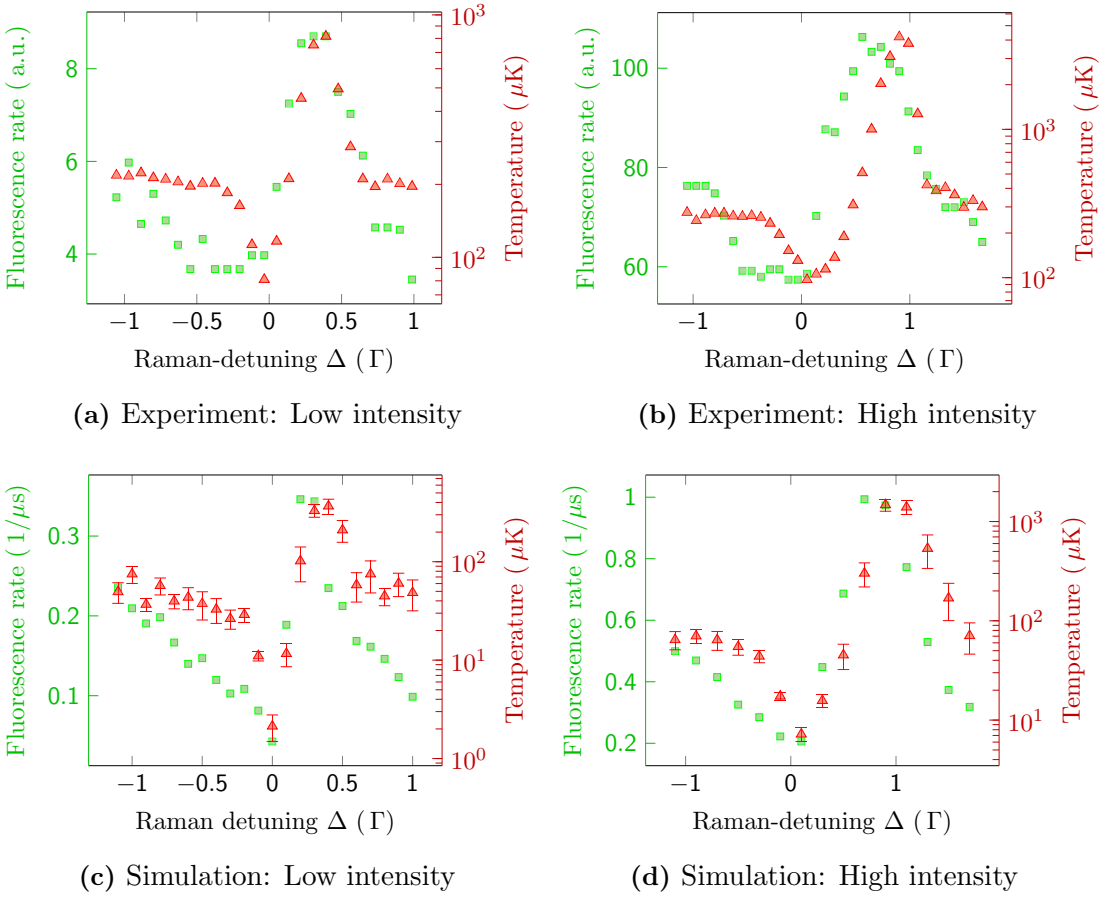

(a) Experiment: Low intensity

(b) Experiment: High intensity

(c) Simulation: Low intensity

(d) Simulation: High intensity

Figure 4.23: Fluorescence (squares) and temperature (triangles) of the ^{6}Li atomic cloud after a 100 μs pulse of D_1 light with variable Raman-detuning Δ. (a) and (c) show the experimental and simulation results for $I_{\mathrm{cool}} = 2.7\, I_{\mathrm{sat}}$, $I_{\mathrm{rep}} = 0.13\, I_{\mathrm{sat}}$, (b) and (d) for $I_{\mathrm{cool}} = 9\, I_{\mathrm{sat}}$, $I_{\mathrm{rep}} = 0.46\, I_{\mathrm{sat}}$ per beam.

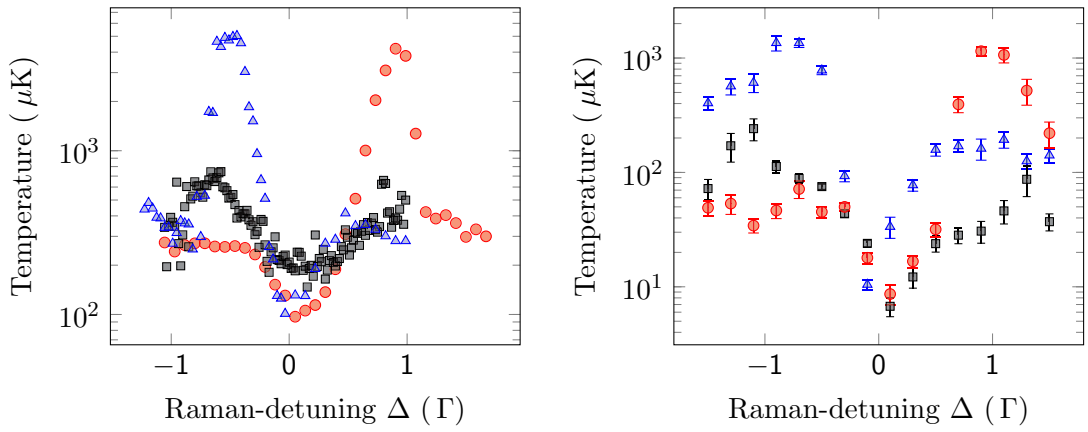

(a) Experiment **(b)** Simulation

Figure 4.24: Temperature of the ^{6}Li D_1 molasses after a 100 μs pulse with variable Raman-detuning Δ for different cooling and repumping intensities. Standard intensities (red circles): $I_{\text{cool}} = 9\, I_{\text{sat}}$, $I_{\text{rep}} = 0.46\, I_{\text{sat}}$. Black squares: $I_{\text{cool}} = I_{\text{rep}} = 9\, I_{\text{sat}}$. Inverted cooling/repumping ratio (blue triangles): $I_{\text{cool}} = 0.18\, I_{\text{sat}}$, $I_{\text{rep}} = 1.2\, I_{\text{sat}}$.

The results for different cooling/repumping ratios are shown in Fig. 4.24. The simulation parameters are chosen according to the experimental values. In the usual configuration $I_{\text{cool}}/I_{\text{rep}} > 1$, with $I_{\text{cool}} = 9I_{\text{sat}}$ and $I_{\text{rep}} = 0.45I_{\text{sat}}$, we observe the heating peak for positive Raman-detuning. When inverting the roles of the cooling and repumping light, $I_{\text{cool}}/I_{\text{rep}} < 1$, with $I_{\text{cool}} = 0.18I_{\text{sat}}$ and $I_{\text{rep}} = 1.2I_{\text{sat}}$, the heating peak appears for negative Raman-detuning instead of positive detuning. For $I_{\text{cool}}/I_{\text{rep}} = 1$, with $I_{\text{cool}} = 9I_{\text{sat}}$, we observe moderate heating for both blue and red detuning. Here again simulations and experiments are in good qualitative agreement.

Raman-detuning dependance for ^{40}K

Typical simulation results for ^{40}K are shown in Fig. 4.25b. Compared to ^{6}Li, simulations for ^{40}K require significant higher computation power due to larger internal state dimensions as well as larger atomic mass and therefore slower cooling dynamics. To save computation time, we start at a velocity of 0.2 m/s ($T \sim 50$ μK), and set the simulation time to 2 ms. We record the velocity $\mathbf{v}(t)$ as well as the time-stamped quantum jump events for $t > 1$ ms to calculate the fluorescence rate. For each Raman-detuning Δ 13 trajectories are simulated.

For ^{40}K we use a 2D$^+$-MOT to load the three-dimensional MOT. The rest of the experimental setup is similar to ^{6}Li. Experimental results are presented in Fig. 4.25a, showing temperature and atom number of the D_1 molasses as functions of the Raman-detuning

Δ. The molasses duration is $t_{\mathrm{Molasses}} = 5\,\mathrm{ms}$ with a linear intensity ramp after 3 ms, with parameters given in the caption of Fig. 4.25a. We observe a sharp temperature drop at the Raman-condition, a heating resonance at $\sim 0.7\,\Gamma$ and a flat cooling region below $-0.1\,\Gamma$ and above $2\,\Gamma$. For the flat cooling region the temperature $T \sim 45\,\mu$K is small compared to the Doppler-temperature $T_{\mathrm{Doppler,K}} = 145\,\mu$K. On the Raman-condition the temperature decreases to $23\,\mu$K.

A comparison between Fig. 4.25a and Fig. 4.25b again demonstrates the qualitative agreement between the simulation and the experimental results and that the heating peak position is reproduced by the simulation. Yet, the simulation underestimates the temperature particularly near the Raman-resonance $\Delta = 0$. A full quantum treatment might resolve this temperature discrepancy. However, it is more complicated to implement and would exceed our available computing capacity. It is also possible that other aspects in the experiment reduce the lifetime of the slow atoms trapped in dark states. Re-absorption of photons emitted by other atoms interrupts the dark period and might play an important role. It is well known that such photon re-scattering process is enhanced by the electro-magnetic induced absorption (EIA) effect, and the absorption crosssection for the off-resonant photons can approach a significant fraction of the resonant value. For atomic samples with a size larger than the re-scattered photon mean free path, dark periods can be interrupted at a rate much larger than the spontaneous scattering rate. While the evidence of optical depth dependent temperature is seen experimentally (see Fig. 4.14), a careful simulation of cooling including the photon re-absorption needs significantly higher computation capacity.

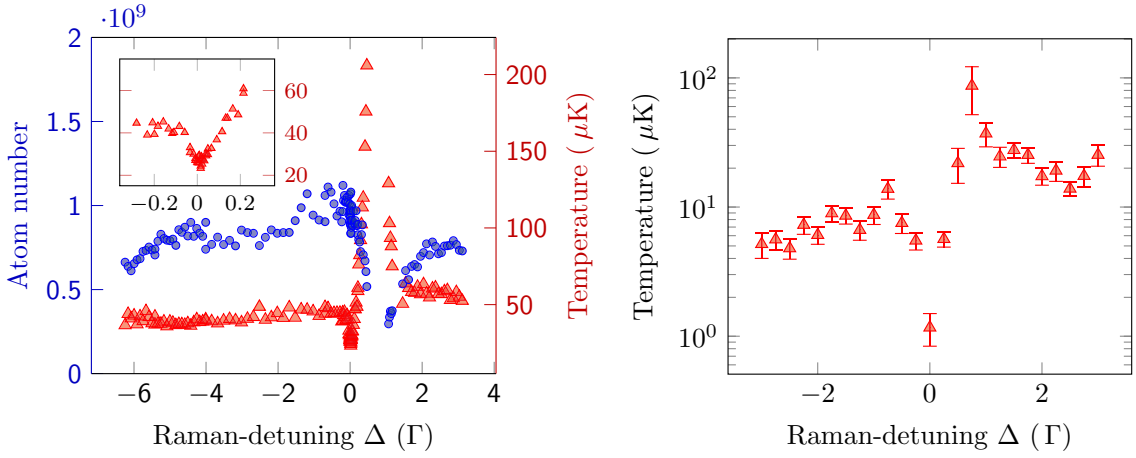

(a) Experiment **(b)** Simulation

Figure 4.25: Equilibrium temperature of the ^{40}K D_1 molasses as a function of Raman-detuning Δ. $\delta_{\mathrm{cool}} = 3\,\Gamma$, $I_{\mathrm{cool}} = 6\,I_{\mathrm{sat}}$, $I_{\mathrm{rep}}/I_{\mathrm{cool}} = 7.6\,\%$. (a) Atom number and temperature as functions of the Raman-detuning Δ. $t_{\mathrm{Molasses}} = 5\,\mathrm{ms}$. Note the narrow cooling zone near the Raman-condition lowering the temperature (red triangles) to $20\,\mu$K and a flat cooling region below $-0.1\,\Gamma$ and above $2\,\Gamma$ resulting from gray molasses cooling without hyperfine coherence effects. (b) $t_{\mathrm{Simulation}} = 2\,\mathrm{ms}$.

4.2.4 Simultaneous D_1 cooling of ^{6}Li and ^{40}K

In the following we discuss the simultaneous operation of the ^{6}Li- and ^{40}K D_1 molasses. The timing sequence and parameters are the same as for single species-operation. The D_1 molasses phase is composed of a 3 ms capture phase and a 2 ms cooling phase. Table 4.2 summarizes the optimal parameters of the dual-species molasses.

	Potassium	Lithium
P_{fiber} (mW)	230	300
δ_{cool} (Γ)	2.3	4
δ_{rep} (Γ)	2.3	4
I_{cool} per beam (I_{sat})	14	14
$I_{\mathrm{cool}}/I_{\mathrm{rep}}$	8	20
D-line properties	^{40}K	^{6}Li
$\Gamma/(2\pi)$ (MHz)	6.04	5.87
I_{sat} (mW/cm^2)	1.75	2.54

Table 4.2: Parameters of the ^{6}Li-^{40}K dual-species molasses.

The presence of the other species reduces the atom numbers in the MOTs by 4 % for ^{6}Li and by 10 % for ^{40}K. However, we observe no mutual influence during the CMOT and the D_1 molasses phase. The temperatures and relative atom numbers in dual-species operation do not differ from single-species operation. The short duration of the CMOT and the molasses phases, being on the order of some milliseconds, and the large detuning between the two D_1 transitions of ^{6}Li and ^{40}K, prevent a distinct mutual influence of the two molasses. Table 4.3 summarizes the performance of the different experimental phases in dual species-operation. For both ^{6}Li and ^{40}K the D_1 molasses phase largely reduces the temperature while the cloud-size after the CMOT phase is conserved. For both species this leads to a phase-space density close to 10^{-4}. These conditions are well suited to directly load an optical dipole trap [144] or magnetic traps.

	T (μK)	N ($\times 10^8$)	n ($\times 10^{10}$ cm^{-3})	ϕ [a] ($\times 10^{-5}$)
LITHIUM				
Mot	1000	20	2.6	0.03
CMot	800	20	18	0.29
Molasses	48	12	7.6	8.2
POTASSIUM				
Mot	240	32	7	0.02
CMot	2000	32	37	0.06
Molasses	11	32	30	10.7

Table 4.3: Performance of the different experimental phases for ^{6}Li and ^{40}K, in dual species operation. We show the optimum temperature T, the atom number N, the density n and the phase-space density ϕ.

[a] The given phase-space density does not take into account the different internal states and is calculated as $\phi = n\lambda_B^3$, where λ_B is the thermal de Broglie wavelength.

4.3 Conclusion

In this chapter, we have shown that simultaneous sub-Doppler laser cooling of ^{6}Li and ^{40}K atoms is a simple and robust technique, resulting in a phase space density close to 10^{-4} for both atomic species. We observe no mutual effect of the two molasses. This cooling scheme enables efficient direct loading of magnetic- and optical dipole traps. The large gain in temperature offers a promising route for fast evaporation to quantum degeneracy.

We studied the Raman-detuning dependence of the final temperature of the atomic cloud and the photon scattering rate, revealing the importance of the Raman-resonance condition. For zero Raman-detuning, a new class of dark states emerges, due to long lived coherences between hyperfine states. This Λ-enhancement, leads to efficient cooling forces near the Raman-condition, resulting in an improved cooling efficiency. We compared the experimental findings to a semiclassical MonteCarlo Wavefunction simulation, that takes into account all relevant Zeeman levels and the three dimensional σ^+–σ^- counter-propagating beam configuration, and we find a good qualitative agreement between the experimental results and the simulations.

Moreover, we used the D_1 molasses scheme to cool bosonic ^{41}K. We cooled all 5×10^9 ^{41}K atoms from a CMOT to a final temperature of $20\,\mu$K leading to a phase-space density of 1.1×10^{-4}. To date, several other research groups implemented our D_1 cooling scheme to improve the performance of their experiments [142–145] [10].

[10] and ^{7}Li by Ketterle at MIT, Cambridge, United States (private communication) and ^{40}K by Kuhr, University of Strathclyde, Glasgow, United Kingdom (private communication).

5 Magnetic trapping, transport and evaporation

In the previous chapter we showed that sub-Doppler cooling is a powerful technique to increase the phase-space density of the atomic sample. However, the phase-space density needs to be increased by another four orders of magnitude to reach the quantum degenerate regime. Therefore, the atoms, captured and cooled by the MOT and molasses, are transferred to a non-dissipative trap for evaporative cooling. Conventional conservative traps used to achieve quantum degeneracy are magnetic traps and optical dipole traps. In our setup, we load the atoms from the molasses into a magnetic quadrupole trap. Then a magnetic transport transfers the cloud from the MOT- to the science chamber. In the science cell, we perform evaporative cooling. The evaporation is initiated in a plugged magnetic quadrupole trap and continued in an optical dipole trap.

This chapter starts with the basic concepts of magnetic trapping and the transfer to the magnetic trap (Section 5.1). Then, we present thermalization experiments in the quadrupole magnetic trap(Section 5.2). In Section 5.3, the magnetic transport to the science cell is characterized. Finally, Section 5.4 describes the evaporative cooling in the optically plugged magnetic quadrupole trap and further evaporation in an optical dipole trap.

5.1 Magnetic trapping

5.1.1 Principles of magnetic trapping

The unpaired electron of neutral alkali atoms gives rise to a magnetic dipole moment on the order of the Bohr magneton μ_B, enabling magnetic trapping [231]. The magnetic moment $\boldsymbol{\mu}_\mathrm{m}$ of an atom in an external magnetic field $\boldsymbol{B}(\boldsymbol{r})$ has the interaction energy

$$E(\boldsymbol{r}) = \boldsymbol{\mu}_\mathrm{m} \cdot \boldsymbol{B}(\boldsymbol{r}). \tag{5.1}$$

The resulting force drives the atom towards the extremum of the magnetic field. The orientation of $\boldsymbol{\mu}_\mathrm{m}$ with respect to the field direction decides weather this is a minimum or maximum. In free space no static magnetic field maximum exists [232]. Therefore, only low field seeking states with a magnetic moment antiparallel to the field direction can be trapped.

For weak magnetic fields the Zeeman interaction is linear. In this regime the magnetic moment of the atom

$$\boldsymbol{\mu}_\mathrm{m} = -g_\mathrm{F}\mu_\mathrm{B}\boldsymbol{F} \tag{5.2}$$

depends on the Landé g-factor g_F and the total angular momentum $\boldsymbol{F}$ of the atomic state, with $\mu_\mathrm{B} \approx h \times 1.4\,\mathrm{MHz/G}$. The projection of $\boldsymbol{F}$ to the field direction z is quantized, yielding the atomic energy levels

$$E(m_\mathrm{F}) = g_\mathrm{F} m_\mathrm{F} \mu_\mathrm{B} B, \tag{5.3}$$

where m_F is the quantum number of the z-component of $\boldsymbol{F}$. The states with $g_\mathrm{F} m_\mathrm{F} > 0$ are trappable low field seekers.

For arbitrary magnetic fields the energy levels can be calculated with the Breit-Rabi formula [233]. Figure 5.1 shows the hyperfine ground states of ^{40}K and ^{6}Li. The linear Zeeman regime for ^{40}K extends to $\sim 357\,\mathrm{G}$ and for ^{6}Li to $\sim 27\,\mathrm{G}$. [1]

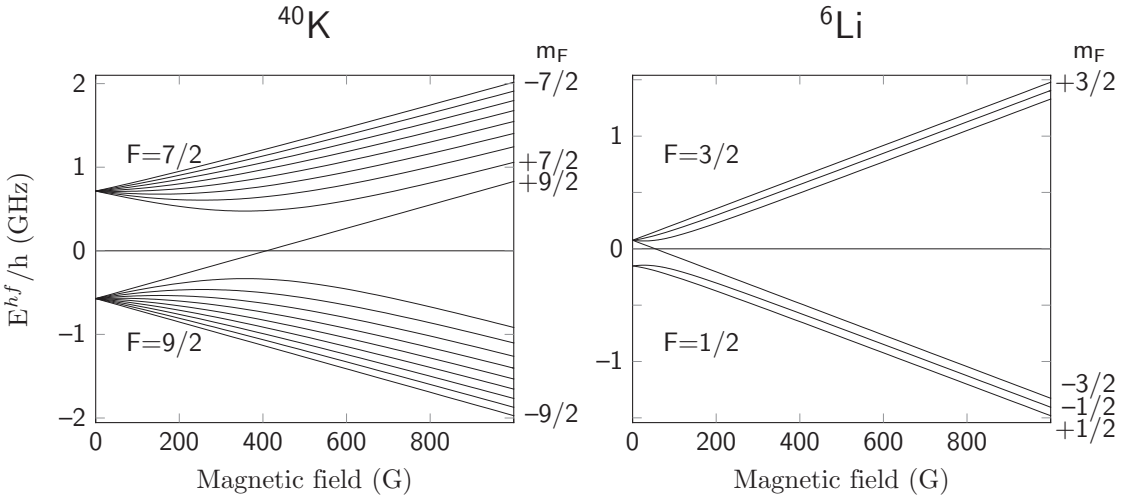

Figure 5.1: Energy levels of ^{40}K and ^{6}Li in a magnetic field. Note that the hyperfine structure of ^{40}K is inverted, $|F = 9/2\rangle$ is lower in energy than $|F = 7/2\rangle$. This particularity of ^{40}K allows *stable* magnetic trapping of two different spin states. The low field seeking states have a positive slope.

[1] For the stretched states $m_\mathrm{F} = \pm\max(F)$ it extends to large magnetic fields.

Quadrupole potential

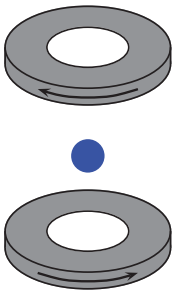

Figure 5.2: Atomic cloud trapped at the center of a coil pair in anti-Helmholtz configuration, creating a quadrupole potential. The arrows on the coils denominate the direction of the current, flowing through the coils. The magnetic field at the trap center is zero.

We use a magnetic quadrupole trap [2] in both the MOT chamber and the science cell (see Fig. 5.2). The magnetic quadrupole field is of the form

$$\boldsymbol{B}(\boldsymbol{r}) = \frac{1}{2}\begin{pmatrix} -B'x \\ -B'y \\ 2B'z \end{pmatrix}, \tag{5.4}$$

with the magnetic field gradient in axial direction B'. Together with Eqs. (5.1) to (5.3) the quadrupole field yields an adiabatic potential

$$V(\boldsymbol{r}) = \frac{1}{2} g_{\mathrm{F}} m_{\mathrm{F}} \mu_{\mathrm{B}} B' \sqrt{x^2 + y^2 + 4z^2}. \tag{5.5}$$

$V(\boldsymbol{r})$ traps atoms in low field seeking states around its minimum $V(0) = 0$ and is linear in r along the coordinate axes.

Majorana losses

An atom remains trapped as long as the magnetic moment adiabatically follows the magnetic field. The magnetic moment precesses around $\boldsymbol{B}(\boldsymbol{r})$ with the Larmor frequency

$$\omega_{\mathrm{L}} = \frac{\mu_{\mathrm{m}} B}{\hbar}. \tag{5.6}$$

[2] A coil pair in anti-Helmholtz configuration

If the rate of change of the magnetic field direction is small compared to the Larmor frequency, the atom stays trapped. We get the adiabaticity condition

$$\left|\frac{d}{dt}\frac{\boldsymbol{B}}{B}\right| = \left|(\boldsymbol{v}\cdot\boldsymbol{\nabla})\frac{\boldsymbol{B}}{B}\right| \ll \omega_{\mathrm{L}}, \tag{5.7}$$

where $\boldsymbol{v}$ is the atom velocity. When violating the adiabaticity condition, the atom

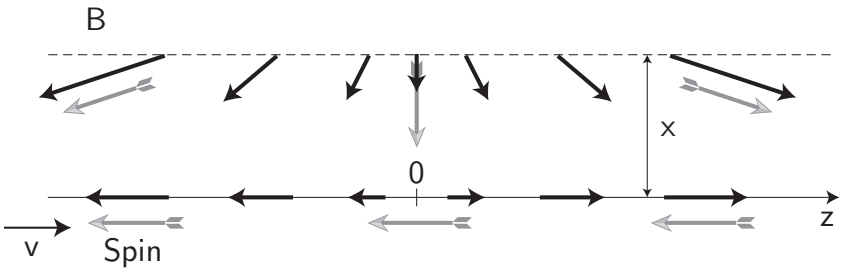

Figure 5.3: Majorana spin-flips: Losses induced by non-adiabatic transitions in a quadrupole trap. An atom which passes the center with a large enough distance x follows the field adiabatically. Its magnetic moment $\boldsymbol{\mu}_{\mathrm{m}}$ stays aligned with the magnetic field $\boldsymbol{B}$. When directly crossing the center of the quadrupole trap the magnetic moment can not adiabatically follow the direction of the magnetic field. The atom changes its internal state eventually to a high field seeking state and is repelled from the trap.

can change its internal state and become a high field seeker. Hence it is repelled from the trap. These "Majorana spin-flips" occur generally near the center of the quadrupole magnetic trap, where the magnetic field changes direction (see Fig. 5.3). The trap center can be seen as a "hole"[3] with an effective size depending on the atomic velocity v. The adiabaticity condition (Eq. (5.7)) yields an effective hole size in z-direction [7] of

$$z_0 = \sqrt{\frac{\hbar v}{\mu_{\mathrm{m}} B'}}. \tag{5.8}$$

The Majorana losses are negligible when we load the magnetic trap from the molasses but become important for evaporative cooling. During the cooling process the relative size of the hole with respect to the cloud size increases and will ultimately stop the evaporation. Therefore the hole has to be plugged, e.g. with an additional bias magnetic field [234, 235] or with a blue detuned laser beam, repelling the atoms from the trap center [2]. We chose the optically plugged magnetic trap because of the large optical access and the tight confinement. The latter enables efficient evaporative cooling.

[3] Because atoms can spin-flip to untrapped states and are lost.

Spin-relaxation

Another loss mechanism in a magnetic trap is spin-relaxation. Figure 5.1 shows that ^{6}Li atoms can only be magnetically trapped in the $|F = 3/2\rangle$ ground state because all m_F states in $|F = 1/2\rangle$ are high field seekers. Moreover, $|F = 3/2\rangle$ lies above $|F = 1/2\rangle$ in energy. Thus collisions between trappable atoms in $|F = 3/2, m_F = 3/2\rangle$ and $|3/2, 1/2\rangle$ can end up in $|F = 1/2\rangle$ [164]. The energy difference between the two hyperfine levels [4] is converted to kinetic energy. The latter is $\sim 10\,\mathrm{mK}$ and suffice to remove the colliding atoms from the trap. Therefore a stable ^{6}Li magnetic trap only contains atoms in the $|3/2, 3/2\rangle$ state. This is also the reason why ^{6}Li can not be evaporated alone in a magnetic trap [236]. There are no collisions in a spin-polarized fermionic lithium gas below $T \sim 6\,\mathrm{mK}$ [7].
On the contrary, the level structure of ^{40}K is inverted. Figure 5.1 shows that $|F = 9/2\rangle$ lies below $|F = 7/2\rangle$. Therefore spin-relaxation is suppressed, enabling sympathetic cooling between $|F = 9/2, m_F = 9/2\rangle$ and $|9/2, 7/2\rangle$ [124].

5.1.2 Transfer from the D_1 molasses to the magnetic quadrupole trap

After the D_1 molasses has cooled the atom cloud, the atoms are optically pumped to low field seeking states before transferring them to the magnetic quadrupole trap [5].

Optical pumping

We optically pump the atoms to stretched states [6] by illuminating them with a resonant circular light beam. For both ^{40}K and ^{6}Li we use bichromatic beams with a cooling and repumping frequency. A small bias magnetic field of 2 G along the beam direction defines the quantization axis.
The ^{40}K spinpol beam operates on the D_2 line with its cooling (repumping) frequency on the $|F = 9/2\rangle \rightarrow |F' = 11/2\rangle$ ($|F = 7/2\rangle \rightarrow |F' = 9/2\rangle$) transition. The beam has a $1/e^2$-diameter of $\sim 5.1\,\mathrm{mm}$, a peak intensity of $\sim 1.5\,I_{sat}$, a cooling/repumping ratio of ~ 10 and the light pulse has a duration of $\sim 70\,\mu s$.
The ^{6}Li spinpol beam operates on the D_1 line with its cooling (repumping) frequency on the $|F = 3/2\rangle \rightarrow |F' = 3/2\rangle$ ($|F = 1/2\rangle \rightarrow |F' = 3/2\rangle$) transition. The beam has a $1/e^2$-diameter of $\sim 5.1\,\mathrm{mm}$, a peak intensity of $\sim 2\,I_{sat}$, a cooling/repumping ratio of ~ 8 and the light pulse has a duration of $\sim 50\,\mu s$.

[4] $\sim 230\,\mathrm{MHz}$ see Fig. 2.10
[5] We use the same coil pair for the MOT and the magnetic trap
[6] $|9/2, +9/2\rangle$ for ^{40}K and $|3/2, +3/2\rangle$ for ^{6}Li.

During the optical pumping the atomic clouds are heated by $\sim 30\,\mu$K and $\sim 50\,\mu$K for ^{40}K and ^{6}Li, respectively.

Switching on the magnetic trap

After the optical pumping phase, the magnetic trap current is switched on. The cloud shape in the magnetic trap depends on the temperature of the atoms and on the magnetic field gradient B'_z. During the transfer, non-adiabatic heating is minimized when the cloud shape induced by the gradient, matches the cloud shape after the molasses and spinpol phase.
It takes 3 ms to reach the matched magnetic field gradient of $B'_z = 40\,$G/cm, experimentally optimized for ^{40}K. Then, we linearly ramp B'_z to its transport value of 135 G/cm in 450 ms. We achieve transfer efficiencies close to 100% for ^{40}K and $\sim 75\%$ for ^{6}Li. The final temperatures at 135 G/cm are $260\,\mu$K for ^{40}K and $275\,\mu$K for ^{6}Li.

Stray light

Once in the magnetic trap it is important to avoid stray light. Optical excitation and spontaneous emission can spin-flip the atoms to untrapped states. In contrast to ^{40}K only the stretched state can be stably trapped for ^{6}Li. Therefore depolarizing events more likely lead to trap loss. In our experiment we constructed an encasement around the main experimental table, shielding it from stray light originating from the other optical tables. Furthermore we switch off all near-resonant light beams during magnetic trapping and detune the unused light frequencies far from resonance. For this purpose we use AOMs and mechanical shutters. AOMs have fast switching times, on the order of 100 ns, but attenuate the light only by a factor of $\sim 10^{-4}$. For complete extinction we place mechanical shutters in front of the optical fibers, that transfer the light beams to the experimental table. Placed in the focus of a laser beam a shutter has a closing time of $\sim 100\,\mu$s.

5.2 Thermalization and non-ergodicity

In this section we study the thermalization of ^{6}Li atoms in the magnetic quadrupole trap. Applying a too strong spin-polarization pulse heats the ^{6}Li atoms in the vertical direction and creates a distinct, initial temperature anisotropy in the magnetic trap.
Because of spin-relaxation, the magnetic trap only contains ^{6}Li atoms in the $|F = 3/2, m_F = 3/2\rangle$ state (see Section 5.1.1). For a spin polarized, fermionic ^{6}Li gas, there are no collisions below $\sim 6\,$mK [7]. Hence, only collisions between ^{6}Li and ^{40}K

atoms contribute to the thermalization, equilibrating the temperatures in vertical and horizontal direction of the ^{6}Li cloud.

5.2.1 Thermalization experiment

In the experiment the magnetic field gradient B'_z is ramped from its initial value, 40 G/cm, [7] to its final value of 135 G/cm in 450 ms. Figure 5.4 shows the vertical and horizontal temperatures of the ^{6}Li cloud as a function of the holding time in the magnetic trap.

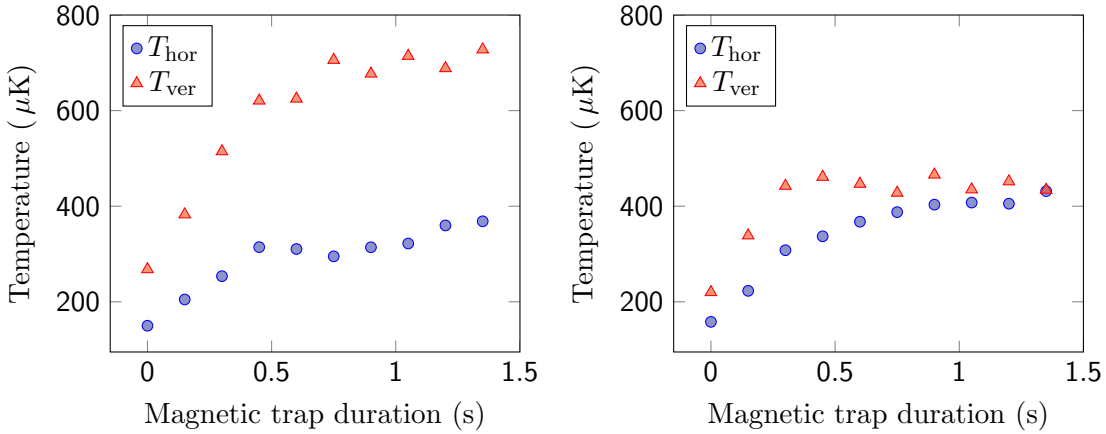

(a) ^{6}Li alone **(b)** ^{6}Li with ^{40}K

Figure 5.4: Thermalization experiment: Temperature of the ^{6}Li atoms as a function of the magnetic trap duration. The magnetic gradient B'_z linearly increases from 40 G/cm to its final value of 135 G/cm in 450 ms. Red triangles represent the vertical temperature, blue circles the temperature in horizontal direction. (a) Spin polarized, fermionic ^{6}Li in the quadrupole magnetic trap. Intra-species collisions are suppressed and the vertical and horizontal temperatures can not thermalize. (b) ^{6}Li is trapped together with ^{40}K. Inter-species collisions enable thermalization of the vertical and horizontal temperatures. The experiment reveals the non-ergodicity in the quadrupole magnetic trap for suppressed collisions.

In Fig. 5.4a, only ^{6}Li is present in the magnetic trap. The initial temperature in vertical direction $T_{ver,0} \sim 270\,\mu$K is significantly larger than the temperature in horizontal direction $T_{hor,0} \sim 150\,\mu$K. During the compression to 135 G/cm, T_{ver} and T_{hor} rise to $\sim 620\,\mu$K and $\sim 315\,\mu$K, respectively. The distinct anisotropy in temperature persists for longer trapping times without a sign of thermalization or ergodicity.

Fig. 5.4b shows the results of the same experimental sequence, with ^{40}K present in the magnetic trap. Here, collisions between ^{6}Li and ^{40}K lead to a thermalization of the

[7] reached in 3 ms after switching on the magnetic trap current

vertical and horizontal temperature of the ^{6}Li cloud. Thermal equilibrium is reached after $\sim 1.4\,\mathrm{s}$.

We also performed thermalization experiments, before we implemented the D_1 cooling for ^{6}Li. During the molasses phase, the D_1 molasses cooled potassium to sub-Doppler temperature, whereas a D_2 molasses decelerated the expansion of lithium without a cooling effect. As a consequence, the temperatures of the two species in the magnetic trap were very different. In a linear trap this leads to a pronounced difference in the occupied volume of the two gases. In fact, the overlap of the two clouds was so small, that we did not observe any thermalization between lithium and potassium. Therefore, we decided to implement a simultaneous D_1 sub-Doppler cooling phase for ^{6}Li and ^{40}K in our experiment.

5.2.2 Non-ergodicity

In the following, we investigate why the observed anisotropy in temperature of a spin polarized ^{6}Li gas in a magnetic quadrupole trap persists (see Fig. 5.4a), even though the quadrupole potential

$$V(\boldsymbol{r}) = \frac{1}{2} g_\mathrm{F} m_\mathrm{F} \mu_\mathrm{B} B' \sqrt{x^2 + y^2 + 4z^2} \tag{5.5}$$

couples the vertical and horizontal directions.

We start with a three-dimensional simulation, using the Boltzmann equation, to compute how the vertical and horizontal temperature evolve with time. Finally, we present a simplified, two-dimensional model in order to illustrate the non-ergodicity.

Simulation

To simulate the ^{6}Li cloud in the magnetic trap, we use the Boltzmann equation

$$\frac{\partial f}{\partial t} + \frac{\mathbf{p}}{m} \cdot \nabla_\mathrm{r} f - \nabla_\mathrm{r} V \cdot \nabla_\mathrm{p} f = \left(\frac{\partial f}{\partial t} \right)_\mathrm{coll} . \tag{5.9}$$

We consider spin-polarized ^{6}Li without ^{40}K. Because of the fermionic nature of ^{6}Li, s-wave collisions are suppressed. Furthermore, at temperatures below $T \sim 6\,\mathrm{mK}$ the angular momentum barrier suppresses p-wave collisions. Consequently, the collision term $\left(\frac{\partial f}{\partial t}\right)_\mathrm{coll}$ is zero. The dynamics simulation is based on the velocity-Verlet algorithm, and determines the position and momentum of the particles after discrete time steps. First, one calculates

$$\mathbf{p}(t + \frac{1}{2}\Delta t) = \mathbf{p}(t) + \frac{1}{2}\mathbf{F}(t)\Delta t \tag{5.10}$$

and

$$\mathbf{r}(t+\Delta t) = \mathbf{r}(t) + \mathbf{p}(t+\frac{1}{2}\Delta t)\frac{\Delta t}{m}. \tag{5.11}$$

Using Eq. (5.11), $\mathbf{F}(t+\Delta t)$ is derived form the quadrupole potential (Eq. (5.5)). This yields

$$\mathbf{p}(t+\Delta t) = \mathbf{p}(t+\frac{1}{2}\Delta t) + \frac{1}{2}\mathbf{F}(t+\Delta t)\Delta t. \tag{5.12}$$

The simulation starts with an anisotropy in temperature.

Results After a sufficiently long evolution in the trap, the potential and kinetic energy of the gas are equipartitioned,

$$\langle V_{\mathrm{tot}}\rangle = 2\,\langle T\rangle \tag{5.13}$$

according to the Virial theorem. However, we find

$$\frac{\left\langle p_{\mathrm{x}}^2\right\rangle}{2m} \neq \frac{\left\langle p_{\mathrm{z}}^2\right\rangle}{2m}, \tag{5.14}$$

in agreement with the persisting anisotropy in temperature observed in Fig. 5.4a.

Simple model

For a collisionless gas, each particle moves independently. In the following, we compute the classical trajectory of a single particle in the quadrupole potential. Reducing the problem to two dimensions, the Hamiltonian is

$$H = \frac{1}{2m}\left(p_{\mathrm{x}}^2 + p_{\mathrm{y}}^2\right) + C\sqrt{x^2+4z^2}, \tag{5.15}$$

with $C = \frac{1}{2}g_{\mathrm{F}}m_{\mathrm{F}}\mu_{\mathrm{B}}B'$.[8] Partial derivation yields the equations of motion

$$\begin{aligned} m\ddot{x} &= -\frac{Cx}{\sqrt{x^2+4z^2}} \\ m\ddot{z} &= -\frac{4\,Cx}{\sqrt{x^2+4z^2}}. \end{aligned} \tag{5.16}$$

Figure 5.5 shows the solution of the equations of motion for the initial conditions, $x(0) = 1\,\mathrm{mm}$, $z(0) = 0.5\,\mathrm{mm}$, $p_{\mathrm{x}}(0) = p_{\mathrm{z}}(0) = 0$. The trajectory is fairly periodic and proves the existence of closed orbits in the quadrupole potential.

[8] For atoms in the stretched state $g_{\mathrm{F}}m_{\mathrm{F}} \sim 1$.

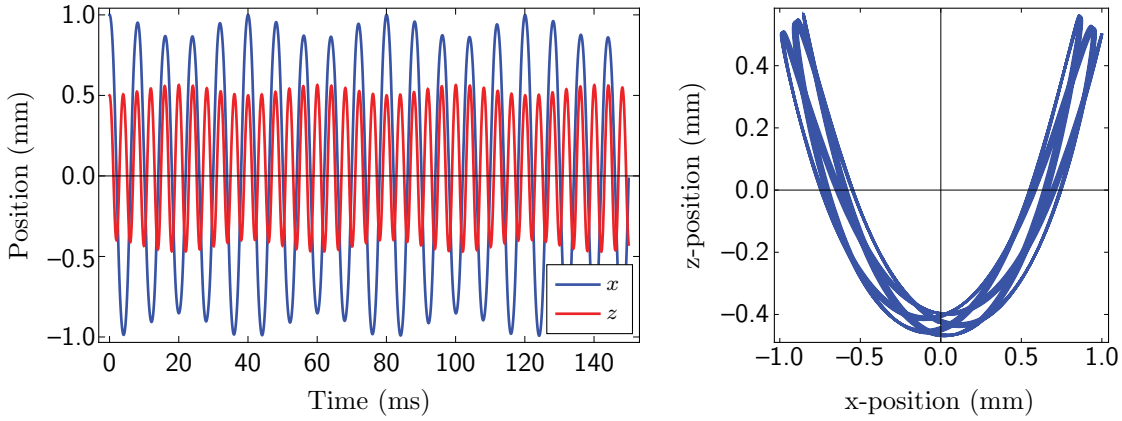

(a) Time evolution **(b)** x-z plot

Figure 5.5: Classical trajectory of a single ^{6}Li particle in a simplified, two-dimensional quadrupole potential (Eq. (5.15)) with initial conditions, $x(0) = 1\,\mathrm{mm}$, $z(0) = 0.5\,\mathrm{mm}$, $p_\mathrm{x}(0) = p_\mathrm{z}(0) = 0$. (a) Note the periodicity of the trajectory. (b) The closed orbit illustrates how an anisotropy in temperature along x and z, as observed in Fig. 5.4a, can persist for a noninteracting gas.

5.3 Magnetic transport

The magnetic transport conveys the atoms from the magnetic trap in the MOT chamber into the science cell (see Fig. 5.7). This brings several advantages: First, we can perform the time consuming evaporative cooling stage in the improved vacuum environment of the science cell. Second, the quadrupole coils can be placed close to the atoms, creating a steep confinement which leads to an efficient evaporation. Third, the small size of the science cell, ensures an excellent optical access. Finally, the 90° corner ("elbow") of the transport creates an additional optical access along the transport axis, and prevents trap loss due to ballistic atoms from the MOT chamber.

The magnetic transport is realized by moving the magnetic trap center from the MOT- to the science chamber, such that the atomic cloud follows. Two different strategies exist. In the first one the trap coils are physically displaced [237]. The second is based on time-varying currents in a static ensemble of overlapping quadrupole coil pairs [153]. We decided on the latter approach because the geometric constraints are less stringent and it excludes mechanical vibrations, therefore yielding a high reproducibility. Furthermore the system is very reliable and low-maintenance. For more details see the thesis of Thomas Salez [149].

In the following we describe the calculation of the transport-currents. The first step is to compute the transport-currents as functions of the trap center position and constraints that determine the magnetic gradients around the trap center.

5.3.1 Algorithm – Keynote

During transport the atoms experience a magnetic field, low enough to assume a linear Zeeman shift (Eq. (5.3)). Furthermore, we use Eq. (5.4), describing the magnetic quadrupole field. We label the transport direction as x-axis, keeping this denomination as well after the elbow. The vertical direction is labeled z-axis and the one completing the orthogonal basis is called y-axis (see Fig. 5.6). Four parameters fix the trap properties: The trap center position in transport direction (x-axis) and the three gradients, defining the trap shape. Because the gradients are coupled by the Maxwell equation $\boldsymbol{\nabla} \cdot \boldsymbol{B} = 0$, we only need three parameters to define the trap shape and position, namely the currents of three successive coil pairs. Figure 5.6 illustrates how such a triplet configuration can move the trap center from the first- towards the third coil pair by diminishing the current in the first pair while increasing it in the third one. When the first current reaches zero a fourth coil pair is switched on and the process is repeated with the new triplet. Repetition enables transport over a long distance. The three currents are independent variables and can be calculated to keep the trap shape constant during the transfer, thus avoiding detrimental heating of the trapped atoms.

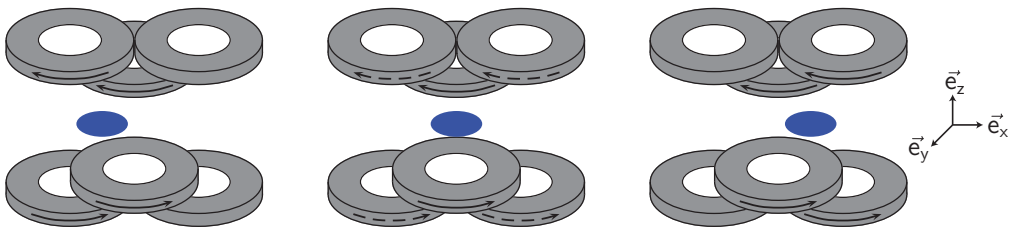

Figure 5.6: Concept of a magnetic transport with a fixed coil assembly and time-varying currents. The arrows on the coils indicate the strength and direction of the electric current. When decreasing the current in the first pair of coils while ramping up the current in the third one, the center of the trap moves towards the latter.

To calculate the currents, we impose the trap center position $x^* = (x^*, 0, 0)$, the y-gradient B'^*_{y} and the aspect ratio $A^* = B'_{\mathrm{x}}/B'_{\mathrm{z}}(x^*)$ and obtain the following system of

equations

$$\begin{aligned} \boldsymbol{B}(x^*) &= \mathbf{0}, && \text{impose trap center,} \\ B'_{\mathrm{y}}(x^*) &= B'^*_{\mathrm{y}}(x^*), && \text{impose y-gradient,} \\ A(x^*) &= A^*(x^*). && \text{impose aspect ratio.} \end{aligned} \tag{5.17}$$

For a triplet configuration with pair index $i = 0, 1, 2$ and currents I_{i} the system of equations reads

$$\begin{aligned} 0 &= \sum_{i=0}^{2} \tilde{B}_{\mathrm{i,x}}(x^*) I_{\mathrm{i}}, \\ -B'^*_{\mathrm{y}}(x^*) &= \sum_{i=0}^{2} (\tilde{B'}_{\mathrm{i,x}}(x^*) + \tilde{B'}_{\mathrm{i,z}}(x^*)) I_{\mathrm{i}}, \\ 0 &= \sum_{i=0}^{2} (\tilde{B'}_{\mathrm{i,x}}(x^*) - A^*(x^*) \cdot \tilde{B'}_{\mathrm{i,z}}(x^*)) I_{\mathrm{i}}, \end{aligned} \tag{5.18}$$

with $\tilde{B}_{\mathrm{i}}$ and $\tilde{B'}_{\mathrm{i}}$ in current-units. We increment the pair index at each switching points. How the switching points are calculated is described in Section 5.3.2

5.3.2 Algorithm – Calculating the time-dependent transport currents

In the following, we describe the code, used to calculate the time-dependent transport currents. The Mathematica programm is structured as follows:

1. Coil parameters
2. Magnetic field calculation
3. Switching points
4. Constraints
5. Currents
6. Dynamics

Master file

The master file contains the description of the transport program version and the date the program has been written. It is used to assign created files to the project and to automatize saving and loading of files.

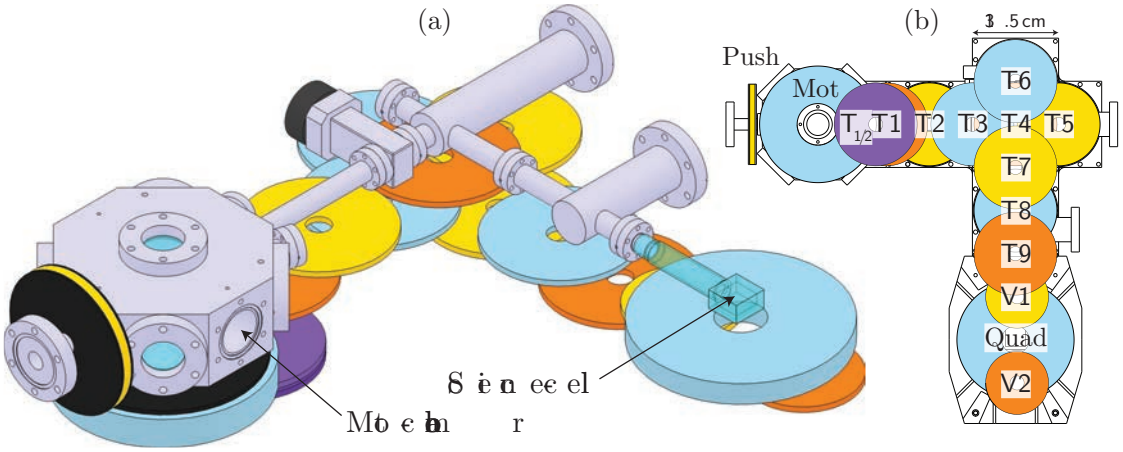

Figure 5.7: Three-dimensional model of the transport coil- and vacuum assembly. (a) Isometric projection. The upper transport coils are hidden to make the vacuum assembly visible (b) Top view of the assembly, including the coil mounts of the lower coils. The coil colors define the power supplies, used for the respective coil. A more detailed scheme of the transport coil- and vacuum assembly is shown in Fig. 5.8.

Coil parameters

The first sub-routine of our Mathematica code defines the transport-coil parameters, such as coil geometry and position. The transport consists of coil pairs in anti-Helmholtz configuration. The only exception is the pushing coil (see Fig. 5.7). Figure 5.8 shows the position and dimensions of the coils used for the transport. The atoms are transported along the x-axis (z=y=0). Because T_4 is the only active coil at the elbow, the transport-currents do not depend on the elbow angle. Therefore we keep x as the transport direction for the second arm. The coil parameters are saved to a file, used to calculate the magnetic fields.

Magnetic field calculation

The magnetic field created by a current loop can be exactly calculated using elliptic integrals [149]. We simulate the transport assembly by adding up individual current loops, using the coil parameters described in the previous section. Then we define functions to calculate the magnetic field and gradients, with the coil currents as input parameters.

Switching points

During the transport, the variation of the aspect ratio $A = B'_x/B'_z$ should be small to minimize heating. When three coil pairs are active the aspect ratio can be chosen as one

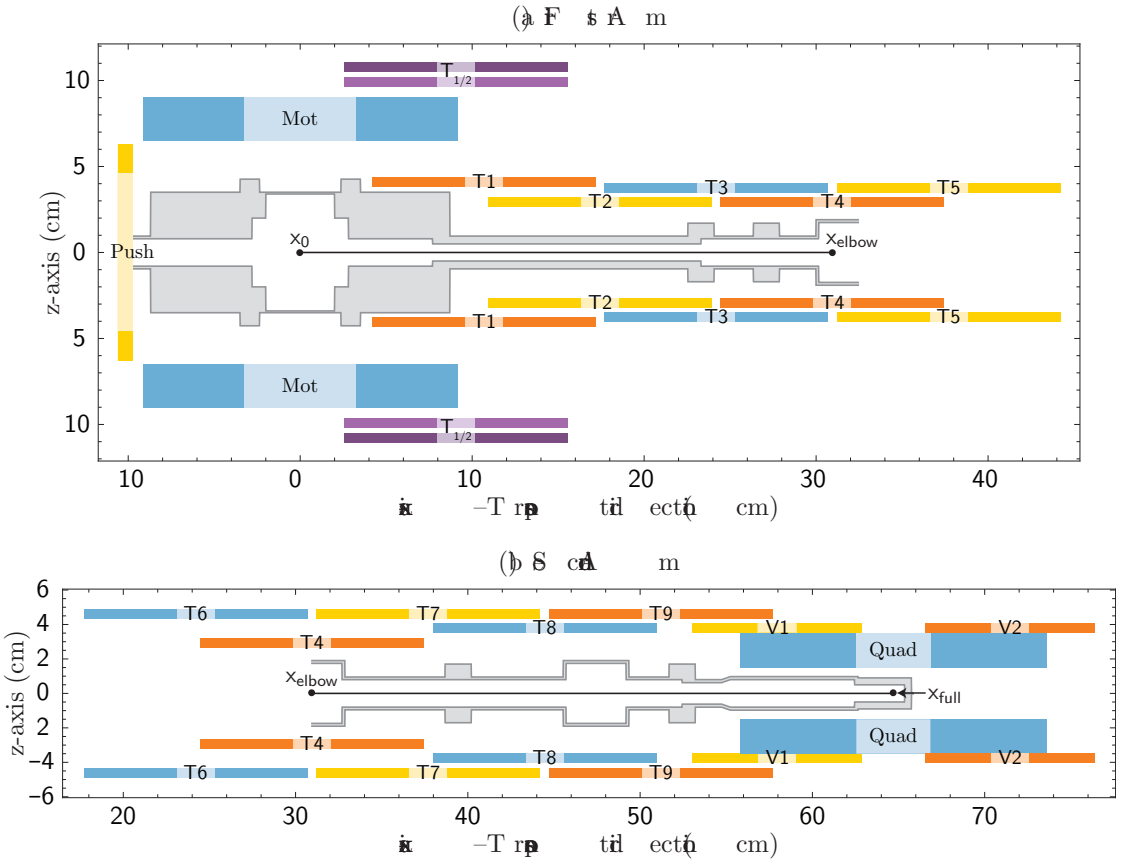

Figure 5.8: Scheme of the transport coil- and vacuum assembly. (a) and (b) show the coils used for the first- and second arm of the transport, respectively. The different coil colors identify the power supply used for the respective coil. The pushing coil P and the $T_{1/2}$-coils compensate for the small overlap between the MOT and the T_1 coils. The "neighbor coils" (V_1 and V_2) have smaller dimensions as the transport coils $T_{1...9}$ to yield vertical optical access in the science cell. Note the differential pumping tube from 7.7 cm to 23.3 cm with a diameter of 1 cm. A three-dimensional model of the transport is shown in Fig. 5.7

of the three free parameters (see Section 5.3.1). However, at the switching point x_{switch} from one triplet-configuration to the next, only two coil pairs are active.[9] Therefore, $A(x_{\text{switch}})$ is given by the geometry of these two coil pairs. In the following we explain how the imposed switching point and the corresponding aspect ratio are calculated to ensure that only two coil pairs are active during the switching.

We consider the switching between the T_1,T_2,T_3-triplet and the T_2,T_3,T_4-triplet, other switching points are calculated in the same way. When we transport atoms from T_2 to T_3 by only using these two coil pairs, we have two free parameters, we can impose the trap position and the y-gradient. However, the aspect ratio is fixed by the trap position and can not be controlled. To calculate the aspect ratio we use

$$\begin{pmatrix} 0 \\ 0 \end{pmatrix} = \begin{pmatrix} B_{\mathrm{x,T_2}} & B_{\mathrm{x,T_3}} \\ B'_{\mathrm{x,T_1}} - A\,B'_{\mathrm{z,T_1}} & B'_{\mathrm{x,T_2}} - A\,B'_{\mathrm{z,T_2}} \end{pmatrix}\Bigg|_{x=x^*} \cdot \begin{pmatrix} I_{\mathrm{T_2}} \\ I_{\mathrm{T_3}} \end{pmatrix}. \tag{5.19}$$

Elimination of the currents gives

$$\frac{B'_{\mathrm{x,T_2}}(x^*) - A(x^*)\,B'_{\mathrm{z,T_2}}(x^*)}{B_{\mathrm{x,T_2}}(x^*)} \stackrel{!}{=} \frac{B'_{\mathrm{x,T_3}}(x^*) - A(x^*)\,B'_{\mathrm{z,T_3}}(x^*)}{B_{\mathrm{x,T_3}}(x^*)}, \tag{5.20}$$

showing that $A(x^*)$ only depends on the geometry of T_2 and T_3 and not on the currents. Equation (5.20) can be solved numerically. Figure 5.9 shows the norm of the aspect ratio $|A|$ as a function of the transport distance. $|A|$ has a minimum at $x_{\text{switch}} = 20.8\,\text{cm}$, Δx_2 and Δx_3 away from the T_2 and T_3 coils, respectively ($x_{\mathrm{T_2}} = 17.45\,\text{cm}$ and $x_{\mathrm{T_3}} = 24.2\,\text{cm}$). $\Delta x_2 > \Delta x_3$ because the separation of the T_2 coils is slightly smaller than that of the T_3 pair.

To understand why x_{switch} is the ideal switching point from the T_1,T_2,T_3-triplet to the T_2,T_3,T_4-triplet, we need the systems of equations to calculate the coil currents for the respective triplet:

$$\begin{pmatrix} 0 \\ 0 \\ -B'^*_{\mathrm{y}} \end{pmatrix} = \begin{pmatrix} B_{\mathrm{x,T_1}} & B_{\mathrm{x,T_2}} & B_{\mathrm{x,T_3}} \\ B'_{\mathrm{x,T_1}} - A^*\,B'_{\mathrm{z,T_1}} & B'_{\mathrm{x,T_2}} - A^*\,B'_{\mathrm{z,T_2}} & B'_{\mathrm{x,T_3}} - A^*\,B'_{\mathrm{z,T_3}} \\ B'_{\mathrm{x,T_1}} + B'_{\mathrm{z,T_1}} & B'_{\mathrm{x,T_2}} + B'_{\mathrm{z,T_2}} & B'_{\mathrm{x,T_3}} + B'_{\mathrm{z,T_3}} \end{pmatrix}\Bigg|_{x=x^*} \cdot \begin{pmatrix} I_{\mathrm{T_1}} \\ I_{\mathrm{T_2}} \\ I_{\mathrm{T_3}} \end{pmatrix} \tag{5.21}$$

[9] Because we use three power supplies, one coil pair of the old and one of the new triplet share the same power supply. Therefore, their currents have to be zero when switching.

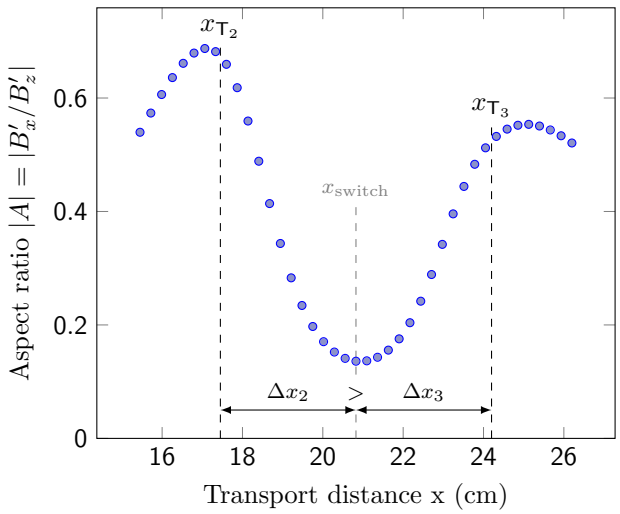

Figure 5.9: Aspect ratio $|A|$ of the magnetic trapping potential created by the coil pairs T_2 and T_3 as a function of the transport distance x. $|A|$ is obtained by numerically solving Eq. (5.20), and has a minimum at x_{switch}. Figure 5.10 explains why x_{switch} is the ideal switching point from one triplet-configuration to the next. $\Delta x_2 > \Delta x_3$ because the separation of the T_2 coils is slightly smaller than that of the T_3 pair.

$$\begin{pmatrix} 0 \\ 0 \\ -B'^{*}_{\text{y}} \end{pmatrix} = \begin{pmatrix} B_{\text{x,T}_2} & B_{\text{x,T}_3} & B_{\text{x,T}_4} \\ B'_{\text{x,T}_2} - A^* B'_{\text{z,T}_2} & B'_{\text{x,T}_3} - A^* B'_{\text{z,T}_3} & B'_{\text{x,T}_4} - A^* B'_{\text{z,T}_4} \\ B'_{\text{x,T}_2} + B'_{\text{z,T}_2} & B'_{\text{x,T}_3} + B'_{\text{z,T}_3} & B'_{\text{x,T}_4} + B'_{\text{z,T}_4} \end{pmatrix} \Bigg|_{x=x^*} \cdot \begin{pmatrix} I_{\text{T}_2} \\ I_{\text{T}_3} \\ I_{\text{T}_4} \end{pmatrix}. \tag{5.22}$$

Imposing the position x^*, the gradient B'^{*}_{y} and the aspect ratio A^*, yields a single unique solution.

Figure 5.10 shows the calculated currents of the transport coils T_1 to T_4 as functions of the transport distance for three different imposed aspect ratios using Eqs. (5.21) and (5.22). The imposed y-gradient is $B'_{\text{y}} = -160\,\text{G/cm}$. The switching point is fixed to x_{switch} from Fig. 5.9. Here, the $|A|$ has a minimum when only T_2 and T_3 are active.

If the imposed aspect ratio matches the one calculate at x_{switch} for the T_2-T_3 configuration (see Fig. 5.10a), the currents in T_1 and T_4 are zero at x_{switch}. This is essential, because we use the same power supply for both coil pairs.

Imposing a too large or too small $|A|$ (see Fig. 5.10b,c), the currents in T_1 and T_4 are non-zero at x_{switch}, which is unfavorable for switching. Furthermore, the position shift induced by the non-zero currents of T_1 and T_4 at x_{switch} causes a discontinuity in the

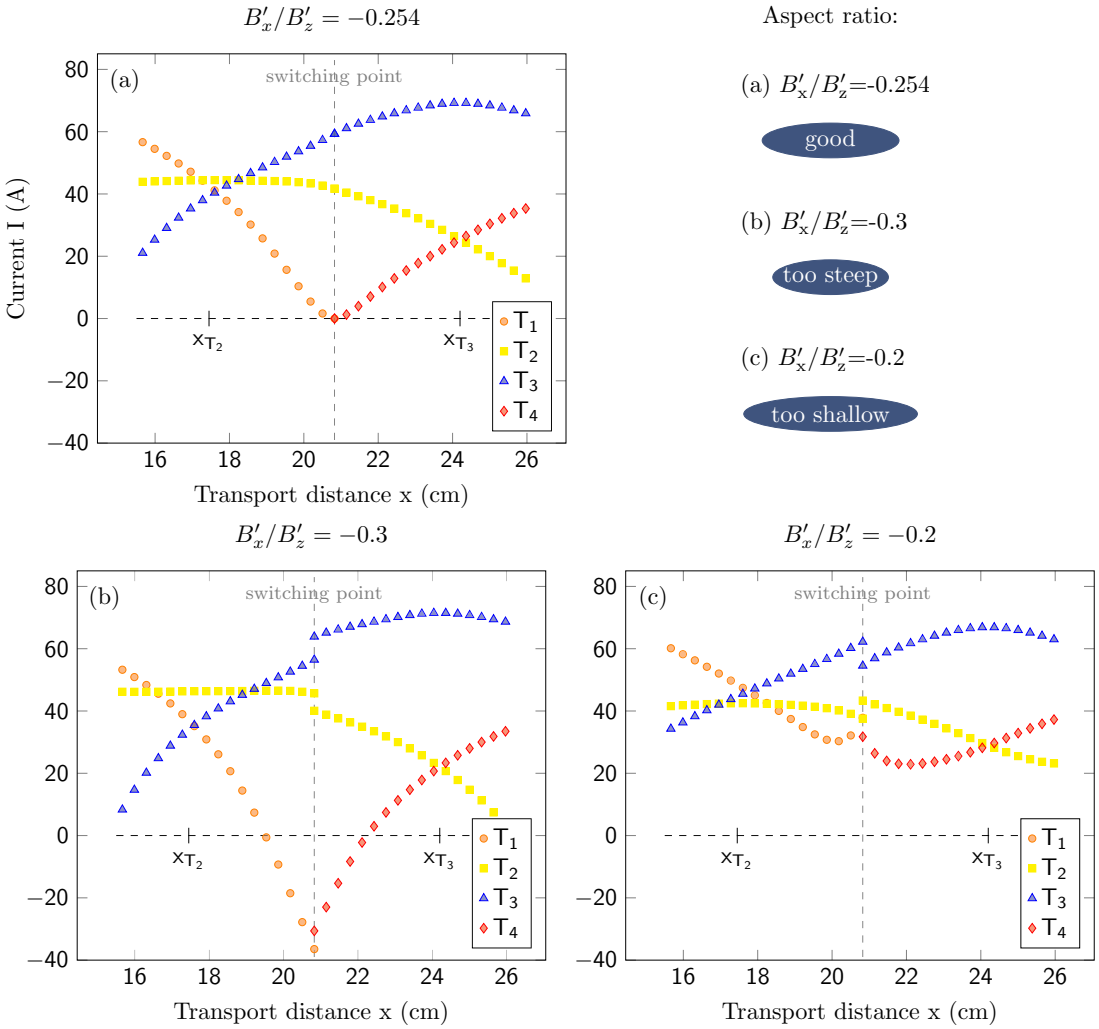

Figure 5.10: Imposing the correct aspect ratio at the switching point. The graphs show the calculated currents of the transport coils T_1 to T_4 as functions of the transport distance for three imposed aspect ratios ((a),(b) and (c)). Until the switching point $x_{\text{switch}} \sim 20.8\,\text{cm}$, the coil pairs T_1, T_2 and T_3 create the magnetic field. At x_{switch} T_1 is switched of whereas T_4 is turned on. The imposed y-gradient is $B'_y = -160\,\text{G/cm}$. Because T_1 and T_4 share the same power supply, both currents have to be zero at x_{switch}. (a) The imposed aspect ratio at x_{switch} is realized with only T_2 and T_3. Therefore the currents in T_1 and T_4 are zero and switching is possible. (b) Too steep relative confinement in x-direction. Negative currents in T_1 and T_4 around x_{switch} are necessary. (c) Too shallow relative confinement in x-direction. T_1 and T_4 run positive currents at x_{switch}, which is unfavourable for switching. The correct switching point and the corresponding aspect ratio are determined by searching the position, where $|A|$ is minimal when only T_2 and T_3 are used (see Fig. 5.9), using Eq. (5.20).

currents of T_2 and T_3. For a too large $|A|$, the currents of T_1 and T_4 become even negative around x_{switch}, creating problems for unipolar power supplies.
Therefore, it is important to use the correct switching point and the corresponding aspect ratio. The geometry of the T_2-T_3 configuration defines the optimal aspect ratio (Eq. (5.20)). At the correct switching point, $|A|$ is minimal. We use a mathematica subroutine to automatically calculate all the switching points for the transport sequence in the same way as exemplified here.

Constrains

We define the transport constraints by imposing the aspect ratio and the y-gradient as functions of the transport-distance. Figure 5.11 shows the constrains we use in our experimental sequence. We impose the constrains at important positions and interpolate between these points to obtain continuous functions. In the previous section we calculated the switching points between successive triplet-configurations, fixing the aspect ratio at these position. At positions where only one coil is active, $|A|$ has to be 0.5. The other important aspect ratio positions as well as the imposed y-gradient are experimentally optimized. We obtain the aspect ratio and the y-gradient as functions of the transport-distance by interpolating between the important points.
There are three critical regions in our transport scheme, that need a special treatment. The transfer from the MOT coils to the first transport coil pair ("injection"), the 90° angle where the transport direction changes ("elbow") and the "out-coupling" from the last transport pair into the quadrupole trap of the science cell.

Injection Two difficulties are linked with the initialization of the transport. First, the transition from the MOT magnetic trap to the transport triplet configuration (see Fig. 5.6) changes the aspect ratio $|A|$ from 0.5 to ∼0.3. Second, the octagonal MOT chamber limits the overlap of the MOT coils (M) with the first transport coils (T_1) (see Fig. 5.7). The small overlap is compensated by the pushing coil (P) and the pulling pair ($T_{1/2}$) to allow for an efficient transfer of the atomic cloud to the transport region. We achieve the best performance when we transport the atoms to the pair T_1 and change the aspect ration back to 0.5. This means that T_1 is the only active coil pair at this position. Then we start transporting from T_1 by going from a single pair to the standard triplet situation.

Elbow The distance between the center of the MOT magnetic trap and the elbow is $L_1 = 31\,\text{cm}$. Here the transport direction changes by 90° (see Fig. 5.7). Therefore $|A|$

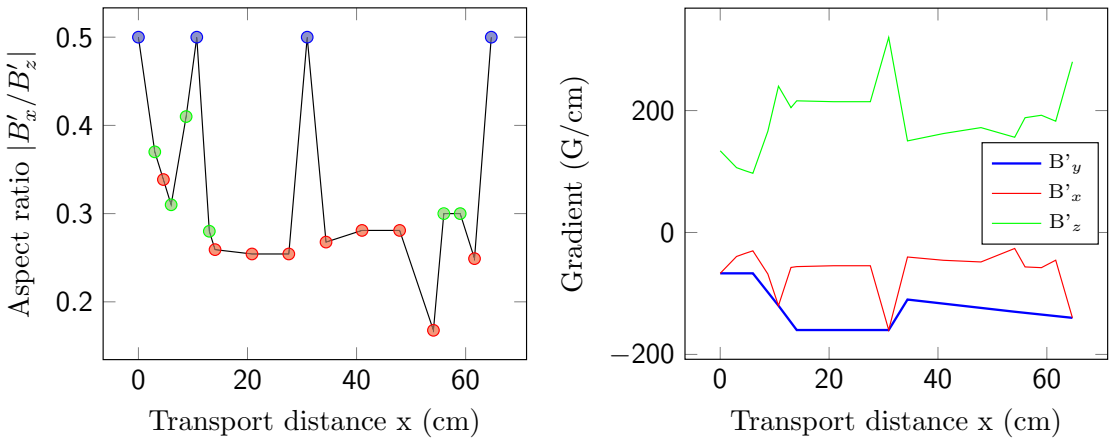

(a) Imposing the aspect ratio

(b) Imposing the y-gradient B'_y

Figure 5.11: Imposing the magnetic transport constraints. (a) Aspect ratio as a function of the transport distance. We impose the aspect ratio at important positions (dots) and interpolate between these points. Blue dots mark positions where only one coil-pair is active. The red dots represent the calculated switching points from one triplet-configuration to the next (see Fig. 5.10). The green dots are optimized experimentally to minimize atom loss and heating during the transport. (b) Gradients as functions of the transport distance. The y-gradient is imposed and optimized experimentally to minimize atom loss and heating. B'_x and B'_z are fixed by B'_y and the aspect ratio.

has to be increased to 0.5 before continuing the transport in the new direction. The elbow is in the center of the fourth transport pair (T_4). Because (T_4) is the only active coil at the elbow, the transport-currents do not depend on the elbow angle. Therefore we keep x as the transport direction for the second arm.

Out-coupling The atoms arrive in the science cell after a total transport distance of $L_2 = 64.7\,\text{cm}$ where they are transferred into the final quadrupole trap. Here again, $|A|$ has to be 0.5. The different geometry of the quadrupole coils as well as the neighbor pairs ($V_{1,2}$), compared to the transport coils, demand for an adjustment of the gradients during the out-coupling (see green dots for $x \sim 58$ in Fig. 5.11a).

Currents

Having imposed the aspect ratio, the y-gradient and the switching points (see Fig. 5.11), we can now calculate the transport currents as functions of the position. Between the positions, where we imposed the aspect ratio, we determine the currents for 25 equidistant points using Eq. (5.18). Interpolation yields continuous current-functions for each coil pair.

During the transport sequence, one power supply drives several coils. IGBTs or Mosfets control which coils are active at a given transport distance. To properly switch the coils during transport, we generate a list of digital-commands that control the IGBTs/Mosfets of the switching circuit. Figure 5.12 shows the transport-currents and the switching-commands as functions of the transport distance.

Current calibration We run the power supplies in voltage control mode during the transport. Therefore, we have to calibrate each coil to obtain the desired output current. For this, we define a master coil pair for each power supply. The other coil pairs, driven by the same power supply are the slave coils.
The master coil-calibrations are implemented in Cicero and are programmed such, that the input parameter of the control-voltage of the power supply's voltage-control corresponds to the output current of the power supply in ampere. The MOT-coils are the master-coils of the blue power supply. The diodes in the circuit create an offset voltage at $I = 0\,\mathrm{A}$. To make sure that the control-voltage V_{CV} is zero when the asked master-current I_{Master} goes to zero, we use the calibration function

$$V_{\mathrm{CV}}(I_{\mathrm{Master}}) = \frac{b \cdot I_{\mathrm{Master}} + c \cdot I_{\mathrm{Master}}^2}{I_{\mathrm{Master}} + a}, \tag{5.23}$$

with the three fit parameters a, b and c. Cicero only excepts a positive input. Therefore, the singularity of Eq. (5.23) at negative I_{Master} is not a problem. Because the blue power supply is calibrated to the MOT-coils, the calculated MOT transport current can be directly imported in Cicero. On the other hand, the slave coils [10] have to be pre-calibrated in the transport-algorithm. This is done by plugging the slave calibration function

$$V_{\mathrm{CV,Sl}}(I_{\mathrm{Slave}}) = \frac{b_1 \cdot I_{\mathrm{Slave}} + c_1 \cdot I_{\mathrm{Slave}}^2}{I_{\mathrm{Slave}} + a_1}, \tag{5.24}$$

into the inverse of the master-calibration (Eq. (5.23))

$$I_{\mathrm{Slave,calib}} = V_{\mathrm{CV}}^{-1}(V_{\mathrm{CV,Sl}}) = \frac{-b + V_{\mathrm{CV,Sl}} - \sqrt{b^2 - 2bV_{\mathrm{CV,Sl}} + 4acV_{\mathrm{CV,Sl}} + V_{\mathrm{CV,Sl}}^2}}{2c}. \tag{5.25}$$

Here I_{slave} is the calculated transport current and $I_{\mathrm{slave,calib}}$ the calibrated input-current for Cicero, ensuring that the real output-current of the blue power supply equals I_{slave}. For the other power supplies the calibration procedure is identical.

[10] T_3, T_6, T_8 and Quad (see Fig. 5.8)

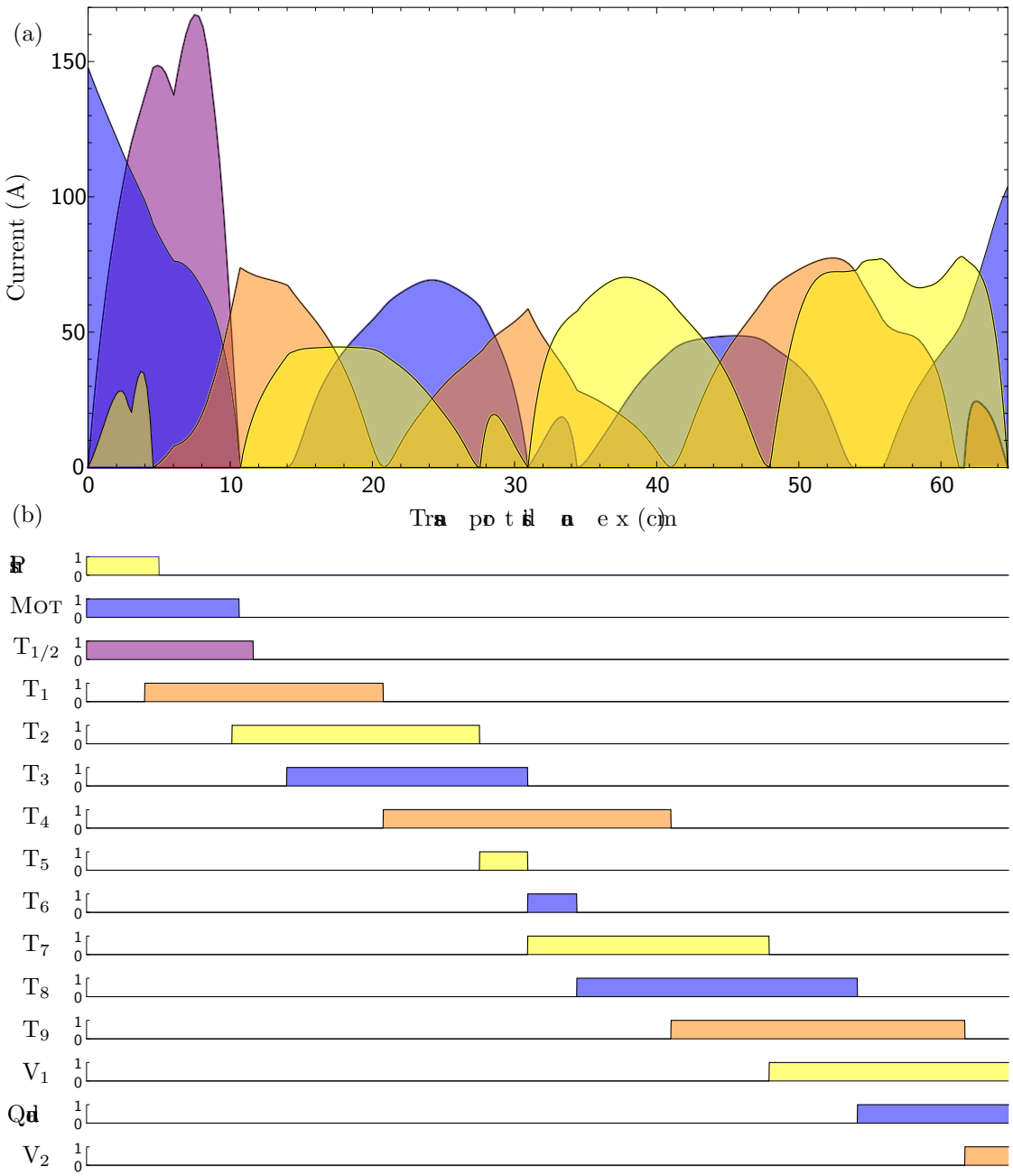

Figure 5.12: Transport currents and coil-switches as functions of the transport distance. (a) Calculated transport currents as functions of the transport distance. The currents are calculated using Eq. (5.18) and fulfill the imposed constraints shown in Fig. 5.11. (b) IGBT/Mosfet-commands to switch between different coil configurations. 1 and 0 correspond to a closed and open circuit, respectively. Comparing (a) and (b) shows which coils are active for a given transport distance.

Dynamics

In the previous section we calculated the transport-currents as functions of the transport position and calibrated the currents of the slave-coils of each power supply. To add dynamics to the transport we define the position as a function of the transport time.

The atoms have to be transported adiabatically to avoid heating. Because the trap shape and position vary with time, the magnetic trap is not conservative any more. Energy can be transferred to the cloud and increase its temperature. Therefore it is important not to exceed a maximum acceleration and that the variation time of the trap geometry is larger than the characteristic evolution times in the trap. These conditions are more stringent for ^{40}K than for ^{6}Li because of its larger mass. We estimate this time scale to be $\sim 15\,\mathrm{ms}$ [149]. On the other hand the Majorana lifetime of ^{6}Li for typical transport parameters is $\tau_{\mathrm{M}}^{\mathrm{Li}} \sim 30\,\mathrm{s}$, compared to $\tau_{\mathrm{M}}^{\mathrm{K}} \sim 200\,\mathrm{s}$ for ^{40}K [149]. Therefore the transport duration should be on the order of seconds.

Consider a transport from $x = 0$ to $x = x_{\mathrm{final}}$ with a time duration t_{final}. For a smooth transport we define the acceleration as a cubic polynomial of the transport time t

$$a(t) = a_* + b_* t + c_* t^2 + d_* t^3, \tag{5.26}$$

with the free parameters a_*, b_*, c_* and d_*. $a(t)$ is continuous differentiable. Integrating $a(t)$ yields the velocity $v(t)$ and the position $x(t)$, while the derivation defines the jerk $j(t)$. The definitions of $x(t)$, $v(t)$ and $a(t)$ yield a system of equations that can be solved with the following boundary conditions:

- For $t = 0\,\mathrm{s}$
  - $x(0) = 0\,\mathrm{m}$,
  - $v(0) = 0\,\mathrm{m/s}$,
  - $a(0) = 0\,\mathrm{m/s^2}$,
- For $t = t_{\mathrm{final}}$
  - $x(t_{\mathrm{final}}) = x_{\mathrm{final}}$,
  - $v(t_{\mathrm{final}}) = 0\,\mathrm{m/s}$,
  - $a(t_{\mathrm{final}}) = 0\,\mathrm{m/s^2}$.

In other words, the atoms should start and end the transport with zero velocity and zero acceleration. Figure 5.13 shows the position, the velocity, the acceleration and the jerk as functions of the transport time. By choosing the transport time t_{final} and the transport distance x_{final} we generate a clock-function to calculate the transport-currents as functions of the transport time. The currents and switches are saved to a .csv-file with a time resolution of 1 ms. This .csv-file contains the calibrated currents of each power

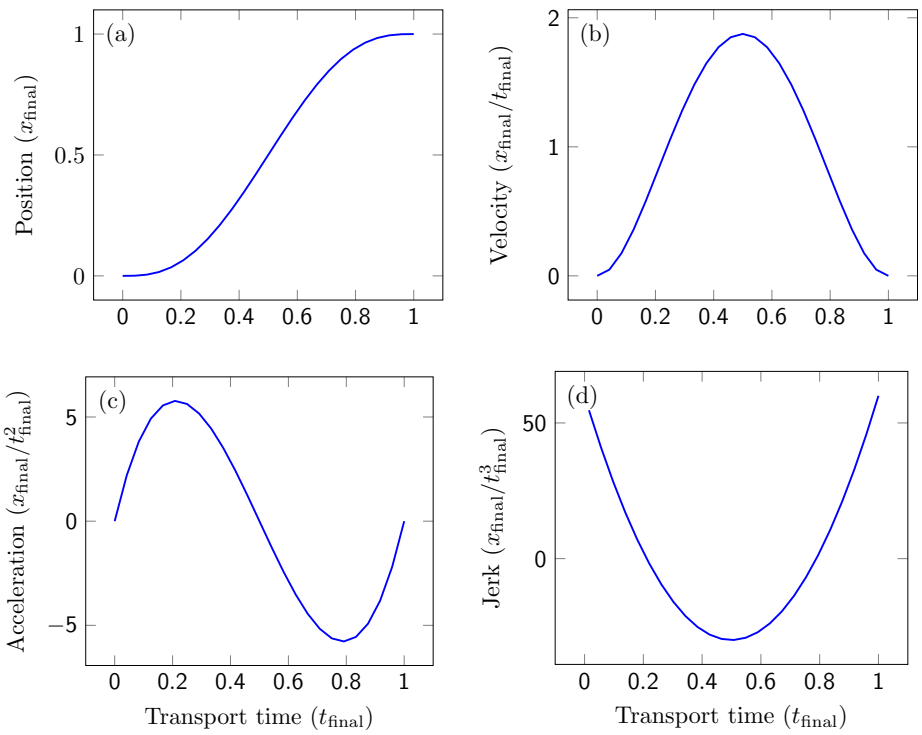

Figure 5.13: Transport dynamics. (a-d) show the position, the velocity, the acceleration and the jerk as functions of the transport time, respectively. The acceleration is defined as a cubic polynomial of the transport time, to assure smooth transport dynamics. At the starting and end position, both the velocity and the acceleration cancel.

supply and the values of the coil-switches in the corresponding columns as functions of the transport time. It is then imported in Cicero and included in the timing sequence. [11]

Trap trajectory The transport is divided in three sections with independent timings: The injection until T_1 and the transport in the first and second arm. Therefore, three independent transport-files are created and strung together in the Cicero timing-sequence. We experimentally optimized the dynamics to minimize heating and trap loss during transport. Table 5.1 summarizes the optimal timings for the three transport sections. The final temperature could be slightly reduced by decelerating the transport in the elbow region and the second arm (see heating in Fig. 5.14a). However, we observe heat expansion of the transport assembly for long transport times. This shifts the zero of the optically plugged magnetic quadrupole trap, such that the plug beam is brought out of centre. Furthermore, the gain in temperature is insignificant and a fast transport ensures high repetition rates.

	Distance (cm)	Duration (s)
x_0 to x_{T_1}	10.7	1
x_{T_1} to x_{elbow}	20.3	1.3
x_{elbow} to x_{full}	33.7	3

Table 5.1: Transport timings. The magnetic transport is divided in three sections with independent timings. For each sections the dynamics shown in Fig. 5.13 are applied. $x_0 = 0$ corresponds to the MOT-position, $x_{elbow} = 31\,\text{cm}$ denominates the elbow and $x_{full} = 64.7\,\text{cm}$ is the full transport length (see Fig. 5.6).

5.3.3 Experimental results

In the following we present the experiments we performed to analyse and optimize the magnetic transport for ^{40}K. The results for ^{6}K are given at the end of this section.

Round-trip experiment

The round-trip experiment allows to probe each transport position x_a. The atoms are transported form the MOT-position x_0 to x_a and back to x_0. Here the number of atoms and their temperature is measured by means of absorption imaging.

[11] It is possible to change the time resolution and total duration of the transport-file in Cicero. Therefore, the transport time can be varied by means of a variables, allowing for a fast and automatized optimization of the transport time.

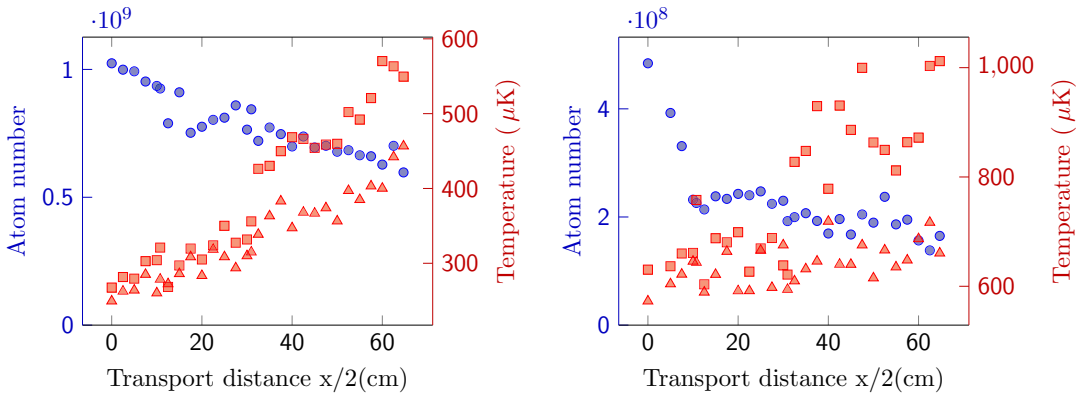

(a) with preceding D_1 molasses **(b)** no preceding D_1 molasses

Figure 5.14: Magnetic transport round-trip experiments for ^{40}K. Atom number (dots) and temperature in x- and z-direction (squares and triangles, respectively) as functions of the transport distance. After the atoms reach the final transport position, the transport sequence is inverted and brings the atoms back to the MOT position x=0, where the temperature and atom number are measured. (a) Roundtrip experiment with preceding D_1 molasses phase. The atom number decreases from 1×10^9 to 6×10^8 atoms for a complete round-trip from the MOT- to the science-chamber and back, yielding a transport efficiency of ∼80%. For a complete round-trip the temperature increases by 200(250) μK in z(x)-direction. The heating in x-direction is more pronounced, because of the direction change at the elbow. (b) Roundtrip experiment without preceding D_1 molasses phase. Compared to (a), the initial atom number is two times smaller, whereas the initial temperature is two times larger. The high initial temperature leads to a large atom loss until ∼15 cm and leads to a more pronounced heating in x-direction.

The round-trip diagnostics has several advantages compared to a direct imaging after a complete transport to the science cell. It provides local information along the transport direction, allowing for a step by step optimization. Furthermore the imaging setup for x_0 and x_a is identical. Therefore the transport efficiency and heating can be precisely measured. On the other hand, the round-trip diagnostics introduces dynamical artifacts. Because the velocity at x_a has to be zero, the dynamics differ from a complete transport. Moreover, the transported distance is twice as long as in a normal transport sequence. However, the measured atom number and temperature after a round-trip allow to estimate the values for the forward run to x_a. In addition, the different dynamics do not play an important role, as the acceleration is kept small.

Hence, round-trip diagnostics is a useful tool to estimate the transport efficiency and the heating to any transport postilion x_a, including a complete transport from the MOT- to the science chamber.

Figure 5.14 shows round-trip measurements performed with optimized transport parameters. To emphasize the importance of the D_1 molasses phase for our experimental

sequence, we measured the atom loss and heating during the transport, with (Fig. 5.14a) and without (Fig. 5.14b) preceding D_1 molasses phase. [12]

With preceding D_1 molasses phase, the transfer efficiency to the magnetic trap is close to one. Figure 5.14a shows the decrease of the atom number from 1×10^9 to 6×10^8 for a complete round-trip, yielding a transport efficiency of ∼80% for a forward run to the science-cell. [13] The temperature increases from $\sim 260\,\mu$K to $550\,\mu$K in x-direction and $450\,\mu$K in z-direction, for a complete round-trip. The more pronounced heating in transport direction is caused by the direction change at the elbow $x_{\mathrm{elbow}} = 31\,$cm. We estimate the heating for a full one way transport to $x_{\mathrm{full}} = 64.7\,$cm to be $\sim 100\,\mu$K in z-direction and $\sim 140\,\mu$K in x-direction.

Without preceding D_1 molasses and CMOT phase, the transfer efficiency to the magnetic trap is only ∼50% and the initial temperature is $\sim 600\,\mu$K (see Fig. 5.14b). The larger initial temperature leads to a severe atom loss form 5×10^8 to 2×10^8 over the first 10 cm of the transport. The DN10 differential pumping tube (see Fig. 5.8)truncates the wings of the atomic distribution. For a complete round-trip, the temperature in x-direction increases to $\sim 1\,$mK.

Summing up, in our experiment the D_1 molasses phase not only provides a reduced initial magnetic trap temperature, but also avoids a pronounced atom loss in the first transport region. With optimized transport-parameters we transfer 80% of the ^{40}K atoms, prepared in the MOT-chamber, to the science cell. The magnetic transport heats the atoms by $\sim 130\,\mu$K.

For ^{6}Li, we obtain a transport efficiency of 70% while the atoms are heated by $\sim 120\,\mu$K.

5.4 Evaporative cooling

Once the magnetically transported atoms arrive in the science cell, the path to quantum degeneracy is continued by means of evaporative cooling. To achieve high final atom numbers, we first evaporatively cool the atoms in a plugged magnetic quadrupole trap. After this intermediate stage, we load the atoms into an optical dipole trap, where we continue the evaporation.

5.4.1 Principle of evaporative cooling

The principle of evaporative cooling is to remove the high-energy tail of a thermalized cloud and to wait for the rethermalization of the sample left behind. The reduced

[12] For the measurements without the D_1 molasses phase, also the CMOT phase was skipped.
[13] The transport efficiency of ∼80% includes vacuum-losses.

energy per particle leads to a lower temperature of the remaining cloud. Repetition of this process further decreases the temperature, with no fundamental lower temperature limit, but is accompanied by a decreasing atom number. In contrast to laser cooling, evaporative cooling profits from high atomic densities [238–241].
The evaporation efficiency can be expressed by

$$T \propto N^{\alpha}, \tag{5.27}$$

where T is the temperature, N the atom number and α the efficiency parameter. α depends on the evaporation trajectory, efficiency of energy removal, losses due to background collisions and the elastic collision rate. A high elastic collision rate is important for the rethermalization. The elastic collision rate

$$\gamma = n\sigma v_T \tag{5.28}$$

depends on the atomic density n, the collision cross-section σ and the mean relative speed v_T. The mean relative speed of a classical gas is given by

$$v_T = \sqrt{\frac{16 k_\mathrm{B} T}{\pi m}}, \tag{5.29}$$

with the Boltzmann constant k_B and the particle mass m. Because the cloud size decreases with T, an efficient evaporation can increase the collision rate during the evaporation process. In this case, the increase in density is faster than the decrease of N and v_T. A large enough α leads to runaway evaporation for bosonic and classical gases. However, when cooling a Fermi gas into the degenerate regime, Fermi-Dirac statistics start to dominate the thermodynamics. Here, Fermi pressure and Pauli blocking lead to a decreasing collision rate, eventually falling to zero at $T = 0$.

5.4.2 Cooling approach

In our experiment, we evaporatively cool a spin mixture of ^{40}K, while ^{6}Li is cooled sympathetically. At the time this chapter is written, we are still optimizing the evaporative cooling phase. By now, we are able to sympathetically cool lithium in the optically plugged magnetic quadrupole trap and to load $\sim 1.5 \times 10^6$ atoms of each atomic species at a temperature of $\sim 55\,\mu$K into an optical dipole trap. Before we continue to work on the dual-species evaporation, we first characterize the single-species evaporation of ^{40}K. In the following, we present the preliminary results for single species evaporation of ^{40}K to quantum degeneracy.

RF evaporation

In a magnetic trap, atoms with higher energy probe larger magnetic fields. A RF field, at a given frequency, that couples trapped $g_F m_F > 0$ states to untrapped $g_{F'} m_{F'} < 0$ ones, removes hot atoms from the trap, because the atomic transitions are shifted and become resonant with the RF radiation at large magnetic fields. The effective trap depth changes with the RF frequency, enabling forced evaporation.

For ^{40}K we drive the magnetic field dependent transitions $|F = 9/2, m_F = 9/2\rangle \rightarrow |7/2, 7/2\rangle$ and $|9/2, 7/2\rangle \rightarrow |7/2, 7/2\rangle$ with a single microwave frequency to remove atoms [163].

As described in Section 2.10.1, the quadrupole trap in the science cell is formed by a custom made coil pair with inner and outer coils. When the ^{40}K atoms arrive in the science cell, the current in the outer coils is ramped to zero. The blue power supply, driving the inner coils, is at this stage operated in current control mode. During the RF evaporation the inner coil current is kept at 100 A, yielding a magnetic gradient of $B'_z = 280\,\mathrm{G/cm}$. We start with 8×10^8 ^{40}K atoms at 650 μK, and sweep the RF field from 1150 MHz to 1260 MHz in 5 s, typically producing a cloud of 1×10^8 atoms at 100 μK.

Optical dipole trap

The optical dipole trap at 1064 nm (ODT_1) is already switched on during the RF evaporation. A 12 W beam, oriented in y-direction [14], is focused to a waist of $w_0 = 42\,\mu\mathrm{m}$ and displaced by $z_0 = 100\,\mu\mathrm{m}$ from the magnetic trap center. We follow the approach presented in [242], by using a combined magnetic quadrupole and optical potential. The cold and dense cloud is transferred to the optical dipole trap by linearly lowering the magnetic field gradient from 250 G/cm to 5 G/cm in 800 ms. We are able to load 3.5×10^7 ^{40}K atoms with a temperature of 55 μK into the ODT. At this point, approximately 60% of the atoms are in the $|9/2, 9/2\rangle$ state and 40% are in the $|9/2, 7/2\rangle$ state. In the dipole trap evaporation is continued by lowering the beam power. During the evaporation, the inner coil current is set to 2.75 A, such that the magnetic gradient compensates the gravitational force for atoms in the $|9/2, 9/2\rangle$ state and provides confinement in the axial direction of the ODT.

[14] Horizontal axis, perpendicular to the transport direction in the second arm

Optical evaporation For $|\Delta| \ll \omega_0$, the dipole potential for an atom with an optical transition frequency ω_0 can be simplified [15] to

$$U_{\mathrm{dip}}(\mathbf{r}) = \frac{3\pi c^2}{2\omega_0^3}\frac{\Gamma}{\Delta} I(\mathbf{r}). \tag{5.30}$$

Here, Γ is the linewidth of the transition, $\Delta = \omega - \omega_0$ is the detuning of the driving frequency ω from transition frequency, and $I(\mathbf{r})$ is the intensity of the ODT [167]. Lowering the beam power forces evaporation, because atoms with an energy higher than the trap depth can escape. We exponentially decrease the beam power from 12 W to 170 mW in 5.5 s, to obtain $\sim 8 \times 10^6$ atoms at a temperature of $\sim 1.5\,\mu$K.

Crossed dipole trap To increase the confinement in axial direction (y-direction), we switch on a second laser beam at 1064 nm, propagation along the transport direction (x-axis), creating a crossed dipole trap. The second dipole trap (ODT_2) is linearly ramped from zero to 4.8 W in 1.5 s, and has a waist of 330 μm. We wait for 200 ms, to let the atoms fall into ODT_2. During this time, we ramp the magnetic gradient to zero. A small bias field in z-direction, applied during the complete evaporation, ensures that the atoms do not change their spin state. We continue the evaporation by exponentially ramping the ODT_1 power from 170 mW to a final value of 57 mW in 8 s.

Preliminary results At the end of the evaporation ramp, the trap frequencies are measured to be $\omega_\mathrm{x} = 2\pi \times 200\,\mathrm{Hz}$, $\omega_\mathrm{y} = 2\pi \times 25\,\mathrm{Hz}$ and $\omega_\mathrm{z} = 2\pi \times 217\,\mathrm{Hz}$. To determine the number of atoms in each spin state and the corresponding temperature, we perform a Stern-Gerlach experiment to separate the spin states [243, 244]. For this purpose, we apply a magnetic gradient of ∼25 G in z-direction and switch off the crossed optical dipole trap. The magnetic gradient exerts a force on the atoms and deflects them. The force experienced by an atom, depends on its magnetic moment and hence on its spin state (see Section 5.1.1), and leads to a spatial separation of different spin states. We switch off the gradient after 15 ms, when the spatial separation of the spin states is large enough. We wait another 10 ms, to make sure that the magnetic field reached zero, and perform absorption imaging.
Figure 5.15a depicts a cutout of an absorption image, showing ^{40}K atoms in the $|m_\mathrm{F} = 9/2\rangle$ state after a TOF of 25 ms. A polylog fit [166] to the cloud profile, that takes into account the measured trap frequencies, yields an atom number of $\sim 1.2 \times 10^6$, a temperature of

[15] Rotating-wave approximation. Here, the contribution of the magnetic confinement is neglected. The effective potential for atoms in the combined quadrupole plus dipole trap is given in [242].

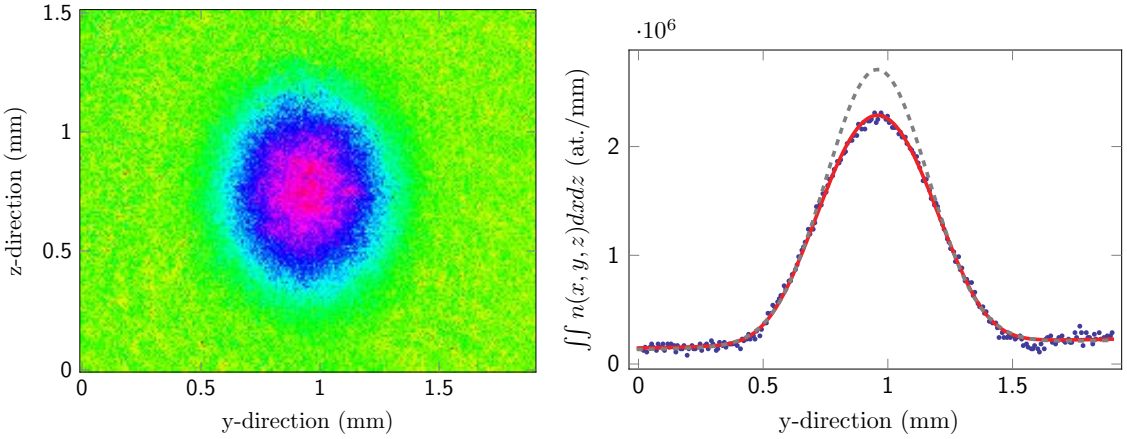

(a) Absorption imaging **(b)** Thomas-Fermi fit

Figure 5.15: (a) Time-of-flight absorption image of a degenerate Fermi gas of ^{40}K atoms in the $|9/2, 9/2\rangle$ state at $T/T_F \sim 0.27$ after a TOF of 25 ms. The first 15 ms a magnetic gradient of ~ 25 G in z-direction, was applied to separate the spin states. (b) Density distribution integrated along z. The observed profile (circles) is well described by fitting a polylogarithmic function to the data (red, solid line). A Gaussian distribution, fitted to the wings of the cloud (gray, dashed line), shows a substantial deviation from the data. The absorption image is averaged over six individual measurements.

260 nK and $T/T_F \sim 0.27$ (see Fig. 5.15b). A polylog fit to the $|m_F = 7/2\rangle$ cloud, results in an atom number of $\sim 7.1 \times 10^5$, a temperature of 270 nK and $T/T_F \sim 0.34$.

For a unitary Fermi gas, the transition to a superfluid of paired fermions occurs at $0.17\,T/T_F$ [92, 93]. To reach this interesting regime, we have to optimize the evaporation parameters to render the evaporation more efficient. Nevertheless, our preliminary results are promising and prove that we are able to produce a degenerate spin-mixture of ^{40}K atoms.

5.5 Conclusion

In this chapter, we presented the stages that lead from a dual species molasses to a quantum degenerate gas of ^{40}K atoms.

First, we described the principles of magnetic trapping and the transfer from the molasses to the magnetic quadrupole trap. Second, we investigated the thermalization in the magnetic quadrupole trap and explained the non-ergodic behavior of spin-polarized ^{6}Li atoms. Then, we characterized the magnetic transport, that conveys the atoms to the science-cell, where evaporation is initialized in an optically plugged magnetic quadrupole trap. The evaporation continues in a crosse optical dipole trap and ultimately leads to

a quantum degenerate spin-mixture of ^{40}K, in the spin-states $|F = 9/2, m_{\mathrm{F}} = 9/2\rangle$ and $|F = 9/2, m_{\mathrm{F}} = 7/2\rangle$, with atom numbers of $\sim 1.2 \times 10^6$ and $\sim 7.1 \times 10^5$, temperatures of 260 nK and 270 nK, and $T/T_{\mathrm{F}} \sim 0.27$ and $T/T_{\mathrm{F}} \sim 0.34$, respectively.
We demonstrated the importance of the simultaneous sub-Doppler cooling phase for the subsequent stages. The gain in temperature, atom number and density in combination with an improved magnetic transport efficiency yield high elastic collision rates and enable an efficient evaporation.

6 Conclusion

In this thesis, we presented the construction of a machine, designed to produce and investigate degenerate Fermi-Fermi gas mixtures of lithium and potassium with large atom numbers.

When I joined the Fermix team, the experimental apparatus has been already partially constructed. A fully functional dual-species MOT produced large samples of ^{6}Li and ^{40}K, with atom numbers on the order of 10^9 for both species. However, at this time, two major issues hindered the progress of the experiment. First, the magnetic transport from the MOT- to the science chamber had a poor transfer efficiency of less than 5%. Second, the insufficient vacuum quality in the science cell would have hindered an efficient evaporation to quantum degeneracy. Furthermore, the experimental control software was not adapted to handle complicated timing sequences and did not allow for automatized parameter scans. To overcome these problems, we first of all exchanged the control software. The ease of use of the new software, the possibility of automatically scanning several lists of parameters at the same time, as well as remote access, rendered the data acquisition efficient and flexible. We exchanged the vacuum assembly in the transport region with new designed vacuum parts, the internal walls coated with an active getter material. This increased the lifetime in the science-cell from 25 s to over 100 s. We could partially solve the transport problem by debugging and improving the transport sequence and by modifying the transport coil assembly. However, the transport efficiency was still limited to 50% and the temperatures in the science cell were too large to reach quantum degeneracy. Therefore, we developed a D_1 sub-Doppler cooling mechanism for ^{40}K to decrease the initial transport temperature. The D_1 molasses phase not only cools the ^{40}K atoms to deep sub-Doppler temperatures, but preserves the large atom numbers of the MOT. In combination with a preceding compressed MOT phase, the atomic density is increased by a factor of five, yielding a phase space density of 10^{-4}. As a consequence of the reduced initial transport temperature, the transport efficiency for ^{40}K increased from 50% to 80% and the final transport temperature was considerably reduced, compared to before. However, the large temperature difference of ^{40}K and ^{6}Li after the D_1 molasses phase created a new challenge. ^{40}K and ^{6}Li did not thermalize in

the magnetic trap, because of the small spacial overlap of the clouds. To decrease the initial ^{6}Li temperature, we implemented the D_1 molasses cooling also for ^{6}Li.

In this context, we utilized a novel all-solid state laser source, we further developed during my thesis, emitting 5 W of output power at 671 nm. The laser has a transversal mode quality factor of $M^2 \sim 1$, operates in longitudinal single-mode and has a linewidth small than 200 kHz. It could serve as a single high-power laser source for experiments involving cooling and trapping of lithium isotopes. Many more applications are thinkable, e.g. in atom interferometry, for lithium isotope separation, or as a low-intensity-noise pump for Cr:LiSAF lasers.

The simultaneous sub-Doppler cooling for ^{40}K and ^{6}Li proved to be robust and efficient. The D_1 molasses phase yields phase space densities of $\sim 10^{-4}$ for both ^{40}K and ^{6}Li. As a result, we obtain large and dense atomic samples for both atomic species after the magnetic transport. The low temperatures and high atomic densities in the optically plugged magnetic quadrupole trap yielded high elastic collision rates and enabled efficient evaporative cooling to quantum degeneracy.

Our new sub-Doppler cooling scheme is applicable to all alkali atoms. The D_1 molasses enables the production of atomic clouds with a high phase-space density, offering a promising route for fast evaporation to quantum degeneracy in optical or magnetic traps. By now, already several other research groups from all over the world have implemented our D_1 cooling scheme to improve the performance of their experiments [142–145] [1]. So far, the D_1 molasses has been adapted to all lithium and potassium isotopes. [2]

Furthermore, we planned and constructed all parts of the machine, necessary for evaporative cooling to quantum degeneracy in the science cell. The evaporation starts in an optically plugged magnetic quadrupole trap and continues in a crossed optical dipole trap. At the moment, we can create a degenerate spin mixture of ^{40}K in the spin-states $|F = 9/2, m_F = 9/2\rangle$ and $|F = 9/2, m_F = 7/2\rangle$, with atom numbers of $\sim 1.2 \times 10^6$ and $\sim 7.1 \times 10^5$, temperatures of 260 nK and 270 nK, and $T/T_F \sim 0.27$ and $T/T_F \sim 0.34$, respectively.

The next step on the way to a quantum degenerate ^{6}Li-^{40}K mixture is the optimization of the dual-species evaporation. Once we achieve a degenerate Fermi-Fermi mixture of ^{6}Li and ^{40}K, we could study many-body systems, where lithium and potassium evolve in different dimensions. One could for example study confinement induced resonances [108–112], p-wave resonances between ^{40}K-^{6}Li dimers and ^{40}K atoms tunable by the lattice

[1] and ^{7}Li by Ketterle at MIT, Cambridge, United States (private communication) and ^{40}K by Kuhr, University of Strathclyde, Glasgow, United Kingdom (private communication).

[2] We cooled all 5×10^9 ^{41}K atoms from a CMOT to a final temperature of 20 μK leading to a phase-space density of 1.1×10^{-4}.

depth [102], the Efimov-effect in mixed dimensions [119] or new many-body quantum phases like interlayer superfluidity, where ^{6}Li mediates interactions between ^{40}K atoms in different layers [120].

These are only some examples and it is possible that new ideas and developments will lead to new directions of our research. In any case, the robustness and high flexibility of the machine presented in this thesis, constitutes a solid fundament for the exploration of fascinating physics.

Bibliography

[1] M. H. Anderson, J. R. Ensher, M. R. Matthews, C. E. Wieman, and E. A. Cornell, *Observation of bose-einstein condensation in a dilute atomic vapor.*, Science (New York, N.Y.) **269**, 198 (1995). 1

[2] K. Davis, M. Mewes, M. Andrews, N. van Druten, D. Durfee, D. Kurn, and W. Ketterle, *Bose-Einstein Condensation in a Gas of Sodium Atoms*, Physical Review Letters **75**, 3969 (1995). 1, 28, 102

[3] C. Bradley, C. Sackett, J. Tollett, and R. Hulet, *Evidence of Bose-Einstein Condensation in an Atomic Gas with Attractive Interactions*, Physical Review Letters **75**, 1687 (1995). 1

[4] B. DeMarco, *Onset of Fermi Degeneracy in a Trapped Atomic Gas*, Science **285**, 1703 (1999). 1, 3, 29

[5] A. Einstein, *Quantentheorie des idealen einatomigen Gases, Sitzber*, Kgl. Preuss. Akad. Wiss (1924). 1

[6] Bose, *Plancks Gesetz und Lichtquantenhypothese*, Zeitschrift für Physik **26**, 178 (1924). 1

[7] W. Ketterle, D. S. Durfee, and D. M. Stamper-Kurn, *Making, probing and understanding Bose-Einstein condensates*, eprint arXiv:cond-mat/9904034 90 (1999). 1, 28, 102, 103, 104

[8] A. Leggett, *Bose-Einstein condensation in the alkali gases: Some fundamental concepts*, Reviews of Modern Physics **73**, 307 (2001). 1

[9] L. Pitaevskii and S. Stringari, *Bose-Einstein Condensation*, Oxford University Press (2003). 1

[10] C. J. Pethick and H. Smith, *Bose–Einstein Condensation in Dilute Gases*, Cambridge University Press, 2nd editio edn. (2008). 1

[11] M. R. Andrews, *Observation of Interference Between Two Bose Condensates*, Science **275**, 637 (1997). 1

[12] K. Madison, F. Chevy, W. Wohlleben, and J. Dalibard, *Vortex formation in a stirred Bose-Einstein condensate*, Physical Review Letters **84**, 806 (2000). 1

[13] J. R. Abo-Shaeer, C. Raman, J. M. Vogels, and W. Ketterle, *Observation of vortex lattices in Bose-Einstein condensates.*, Science (New York, N.Y.) **292**, 476 (2001). 1

[14] J. Denschlag, *Generating Solitons by Phase Engineering of a Bose-Einstein Condensate*, Science **287**, 97 (2000). 1

[15] S. Burger, K. Bongs, S. Dettmer, W. Ertmer, and K. Sengstock, *Dark Solitons in Bose-Einstein Condensates*, Physical Review Letters **83**, 5198 (1999). 1

[16] L. Khaykovich, F. Schreck, G. Ferrari, T. Bourdel, J. Cubizolles, L. D. Carr, Y. Castin, and C. Salomon, *Formation of a matter-wave bright soliton.*, Science (New York, N.Y.) **296**, 1290 (2002). 1

[17] K. E. Strecker, G. B. Partridge, A. G. Truscott, and R. G. Hulet, *Formation and propagation of matter-wave soliton trains.*, Nature **417**, 150 (2002). 1

[18] A. Matsubara, T. Arai, S. Hotta, J. S. Korhonen, T. Mizusaki, and A. Hirai, *Quest for Kosterlitz–Thouless Transition in Two-Dimensional Atomic Hydrogen*, Cambridge University Press, Cambridge (1995). 1

[19] I. F. Silvera, *The quest for Bose-Einstein condensation in atomic hydrogen*, Journal of Low Temperature Physics **101**, 49 (1995). 1

[20] A. P. Mosk, M. W. Reynolds, T. W. Hijmans, and J. T. M. Walraven, *Optical Observation of Atomic Hydrogen on the Surface of Liquid Helium*, Journal of Low Temperature Physics **113**, 217 (1998). 1

[21] A. Safonov, S. Vasilyev, I. Yasnikov, I. Lukashevich, and S. Jaakkola, *Observation of Quasicondensate in Two-Dimensional Atomic Hydrogen*, Physical Review Letters **81**, 4545 (1998). 1

[22] M. Greiner, O. Mandel, T. Esslinger, T. W. Hänsch, and I. Bloch, *Quantum phase transition from a superfluid to a Mott insulator in a gas of ultracold atoms.*, Nature **415**, 39 (2002). 1

[23] J. Weiner and P. S. Julienne, *Experiments and theory in cold and ultracold collisions*, Reviews of Modern Physics **71**, 1 (1999). 1

[24] S. Inouye, M. R. Andrews, J. Stenger, H.-J. Miesner, D. M. Stamper-Kurn, and W. Ketterle, *Observation of Feshbach resonances in a Bose-Einstein condensate*, Nature **392**, 151 (1998). 2, 3, 30

[25] I. Bloch, J. Dalibard, and W. Zwerger, *Many-body physics with ultracold gases*, Rev. Mod. Phys. **80**, 885 (2008). 2

[26] S. Giorgini and S. Stringari, *Theory of ultracold atomic Fermi gases*, Reviews of Modern Physics **80**, 1215 (2008). 2, 39

[27] L. Radzihovsky and D. E. Sheehy, *Imbalanced Feshbach-resonant Fermi gases*, Reports on Progress in Physics **73**, 076501 (2010). 2

[28] F. Chevy and C. Mora, *Ultra-cold polarized Fermi gases*, Reports on Progress in Physics **73**, 112401 (2010). 2

[29] S. Gupta, Z. Hadzibabic, M. W. Zwierlein, C. A. Stan, K. Dieckmann, C. H. Schunck, E. G. M. Van Kempen, B. J. Verhaar, and W. Ketterle, *Radio-frequency spectroscopy of ultracold fermions.*, Science (New York, N.Y.) **300**, 1723 (2003). 2

[30] Y. Shin, M. Saba, T. Pasquini, W. Ketterle, D. Pritchard, and A. Leanhardt, *Atom Interferometry with Bose-Einstein Condensates in a Double-Well Potential*, Physical Review Letters **92**, 050405 (2004). 2

[31] J. Stenger, S. Inouye, A. Chikkatur, D. Stamper-Kurn, D. Pritchard, and W. Ketterle, *Bragg Spectroscopy of a Bose-Einstein Condensate*, Physical Review Letters **82**, 4569 (1999). 2

[32] M. Yasuda and F. Shimizu, *Observation of Two-Atom Correlation of an Ultracold Neon Atomic Beam*, Physical Review Letters **77**, 3090 (1996). 2

[33] E. Burt, R. Ghrist, C. Myatt, M. Holland, E. Cornell, and C. Wieman, *Coherence, Correlations, and Collisions: What One Learns about Bose-Einstein Condensates from Their Decay*, Physical Review Letters **79**, 337 (1997). 2

[34] B. Tolra, K. O'Hara, J. Huckans, W. Phillips, S. Rolston, and J. Porto, *Observation of Reduced Three-Body Recombination in a Correlated 1D Degenerate Bose Gas*, Physical Review Letters **92**, 190401 (2004). 2

[35] S. Fölling, F. Gerbier, A. Widera, O. Mandel, T. Gericke, and I. Bloch, *Spatial quantum noise interferometry in expanding ultracold atom clouds.*, Nature **434**, 481 (2005). 2

[36] W. S. Bakr, J. I. Gillen, A. Peng, S. Fölling, and M. Greiner, *A quantum gas microscope for detecting single atoms in a Hubbard-regime optical lattice.*, Nature **462**, 74 (2009). 2

[37] W. S. Bakr, A. Peng, M. E. Tai, R. Ma, J. Simon, J. I. Gillen, S. Fölling, L. Pollet, and M. Greiner, *Probing the superfluid-to-Mott insulator transition at the single-atom level.*, Science **329**, 547 (2010). 2

[38] J. F. Sherson, C. Weitenberg, M. Endres, M. Cheneau, I. Bloch, and S. Kuhr, *Single-atom-resolved fluorescence imaging of an atomic Mott insulator.*, Nature **467**, 68 (2010). 2

[39] P. D. Lett, R. N. Watts, C. I. Westbrook, W. D. Phillips, P. L. Gould, and H. J. Metcalf, *Observation of Atoms Laser Cooled below the Doppler Limit*, Phys. Rev. Lett. **61**, 169 (1988). 2, 68

[40] A. G. Truscott, K. E. Strecker, W. I. McAlexander, G. B. Partridge, and R. G. Hulet, *Observation of Fermi pressure in a gas of trapped atoms.*, Science (New York, N.Y.) **291**, 2570 (2001). 3

[41] F. Schreck, L. Khaykovich, K. L. Corwin, G. Ferrari, T. Bourdel, J. Cubizolles, and C. Salomon, *Quasipure Bose-Einstein Condensate Immersed in a Fermi Sea*, Physical Review Letters **87**, 080403 (2001). 3

[42] J. McNamara, T. Jeltes, A. Tychkov, W. Hogervorst, and W. Vassen, *Degenerate Bose-Fermi Mixture of Metastable Atoms*, Physical Review Letters **97**, 080404 (2006). 3

[43] T. Fukuhara, Y. Takasu, M. Kumakura, and Y. Takahashi, *Degenerate Fermi Gases of Ytterbium*, Physical Review Letters **98**, 030401 (2007). 3

[44] M. Lu, N. Q. Burdick, and B. L. Lev, *Quantum Degenerate Dipolar Fermi Gas*, Physical Review Letters **108**, 215301 (2012). 3

[45] K. Aikawa, A. Frisch, M. Mark, S. Baier, R. Grimm, and F. Ferlaino, *Reaching Fermi Degeneracy via Universal Dipolar Scattering*, Physical Review Letters **112**, 010404 (2014). 3

[46] B. J. DeSalvo, M. Yan, P. G. Mickelson, Y. N. Martinez de Escobar, and T. C. Killian, *Degenerate Fermi Gas of ^{87}Sr*, Physical Review Letters **105**, 030402 (2010). 3

[47] M. K. Tey, S. Stellmer, R. Grimm, and F. Schreck, *Double-degenerate Bose-Fermi mixture of strontium*, Physical Review A **82**, 011608 (2010). 3

[48] Z. Hadzibabic, S. Gupta, C. Stan, C. Schunck, M. Zwierlein, K. Dieckmann, and W. Ketterle, *Fiftyfold Improvement in the Number of Quantum Degenerate Fermionic Atoms*, Physical Review Letters **91**, 160401 (2003). 3

[49] S. Nascimbène, N. Navon, K. J. Jiang, F. Chevy, and C. Salomon, *Exploring the thermodynamics of a universal Fermi gas.*, Nature **463**, 1057 (2010). 3, 4

[50] M. Inguscio, W. Ketterle, and C. Salomon (eds.), *Proceedings of the International School of Physics Enrico Fermi on Ultracold Fermi gases, Course CLXIV, Varenna,*, Società Italiana di Fisica (2006). 3

[51] E. Timmermans, *Degenerate Fermion Gas Heating by Hole Creation*, Physical Review Letters **87**, 240403 (2001). 3

[52] L. Carr, T. Bourdel, and Y. Castin, *Limits of sympathetic cooling of fermions by zero-temperature bosons due to particle losses*, Physical Review A **69**, 033603 (2004). 3

[53] S. Granade, M. Gehm, K. O'Hara, and J. Thomas, *All-Optical Production of a Degenerate Fermi Gas*, Physical Review Letters **88**, 120405 (2002). 3

[54] S. Jochim, M. Bartenstein, A. Altmeyer, G. Hendl, C. Chin, J. H. Denschlag, and R. Grimm, *Pure Gas of Optically Trapped Molecules Created from Fermionic Atoms*, Physical Review Letters **91**, 240402 (2003). 3

[55] C. Silber, S. Günther, C. Marzok, B. Deh, P. Courteille, and C. Zimmermann, *Quantum-Degenerate Mixture of Fermionic Lithium and Bosonic Rubidium Gases*, Physical Review Letters **95**, 170408 (2005). 3

[56] G. Roati, F. Riboli, G. Modugno, and M. Inguscio, *Fermi-Bose Quantum Degenerate ^{40}K-^{87}Rb Mixture with Attractive Interaction*, Physical Review Letters **89**, 150403 (2002). 3

[57] S. Inouye, J. Goldwin, M. Olsen, C. Ticknor, J. Bohn, and D. Jin, *Observation of Heteronuclear Feshbach Resonances in a Mixture of Bosons and Fermions*, Physical Review Letters **93**, 183201 (2004). 3

[58] M. Köhl, H. Moritz, T. Stöferle, K. Günter, and T. Esslinger, *Fermionic Atoms in a Three Dimensional Optical Lattice: Observing Fermi Surfaces, Dynamics, and Interactions*, Physical Review Letters **94**, 080403 (2005). 3

[59] C. Ospelkaus, S. Ospelkaus, L. Humbert, P. Ernst, K. Sengstock, and K. Bongs, *Ultracold Heteronuclear Molecules in a 3D Optical Lattice*, Physical Review Letters **97**, 120402 (2006). 3

[60] T. Rom, T. Best, D. van Oosten, U. Schneider, S. Fölling, B. Paredes, and I. Bloch, *Free fermion antibunching in a degenerate atomic Fermi gas released from an optical lattice.*, Nature **444**, 733 (2006). 3

[61] M. Taglieber, A.-C. Voigt, T. Aoki, T. Hänsch, and K. Dieckmann, *Quantum Degenerate Two-Species Fermi-Fermi Mixture Coexisting with a Bose-Einstein Condensate*, Physical Review Letters **100**, 010401 (2008). 3, 5

[62] C.-H. Wu, I. Santiago, J. W. Park, P. Ahmadi, and M. W. Zwierlein, *Strongly interacting isotopic Bose-Fermi mixture immersed in a Fermi sea*, Physical Review A **84**, 011601 (2011). 3, 5

[63] F. M. Spiegelhalder, A. Trenkwalder, D. Naik, G. Kerner, E. Wille, G. Hendl, F. Schreck, and R. Grimm, *All-optical production of a degenerate mixture of ^6Li and ^{40}K and creation of heteronuclear molecules*, Physical Review A **81**, 043637 (2010). 3, 5

[64] B. DeMarco, S. Papp, and D. Jin, *Pauli Blocking of Collisions in a Quantum Degenerate Atomic Fermi Gas*, Physical Review Letters **86**, 5409 (2001). 3

[65] H. Feshbach, *Unified theory of nuclear reactions*, Annals of Physics **5**, 357 (1958). 3

[66] U. Fano, *Effects of Configuration Interaction on Intensities and Phase Shifts*, Physical Review **124**, 1866 (1961). 3

[67] E. Tiesinga, B. J. Verhaar, and H. T. C. Stoof, *Threshold and resonance phenomena in ultracold ground-state collisions*, Physical Review A **47**, 4114 (1993). 3

[68] K. M. O'Hara, S. L. Hemmer, S. R. Granade, M. E. Gehm, and J. E. Thomas, *Measurement of the zero crossing in a Feshbach resonance of fermionic ^6Li*, Physical Review A **66**, 041401 (2002). 4

[69] K. Dieckmann, C. A. Stan, S. Gupta, Z. Hadzibabic, C. H. Schunck, and W. Ketterle, *Decay of an Ultracold Fermionic Lithium Gas near a Feshbach Resonance*, Physical Review Letters **89**, 203201 (2002). 4

[70] S. Jochim, M. Bartenstein, G. Hendl, J. Denschlag, R. Grimm, A. Mosk, and M. Weidemüller, *Magnetic Field Control of Elastic Scattering in a Cold Gas of Fermionic Lithium Atoms*, Physical Review Letters **89**, 273202 (2002). 4

[71] T. Loftus, C. Regal, C. Ticknor, J. Bohn, and D. Jin, *Resonant Control of Elastic Collisions in an Optically Trapped Fermi Gas of Atoms*, Physical Review Letters **88**, 173201 (2002). 4

[72] C. A. Regal and D. S. Jin, *Measurement of Positive and Negative Scattering Lengths in a Fermi Gas of Atoms*, Physical Review Letters **90**, 230404 (2003). 4

[73] C. A. Regal, C. Ticknor, J. L. Bohn, and D. S. Jin, *Tuning p-Wave Interactions in an Ultracold Fermi Gas of Atoms*, Physical Review Letters **90**, 053201 (2003). 4

[74] D. S. Petrov, C. Salomon, and G. V. Shlyapnikov, *Weakly Bound Dimers of Fermionic Atoms*, Physical Review Letters **93**, 090404 (2004). 4

[75] S. Jochim, M. Bartenstein, A. Altmeyer, G. Hendl, S. Riedl, C. Chin, J. Hecker Denschlag, and R. Grimm, *Bose-Einstein condensation of molecules.*, Science (New York, N.Y.) **302**, 2101 (2003). 4

[76] M. Greiner, C. A. Regal, and D. S. Jin, *Emergence of a molecular Bose-Einstein condensate from a Fermi gas.*, Nature **426**, 537 (2003). 4

[77] M. Zwierlein, C. Stan, C. Schunck, S. Raupach, S. Gupta, Z. Hadzibabic, and W. Ketterle, *Observation of Bose-Einstein Condensation of Molecules*, Physical Review Letters **91**, 250401 (2003). 4

[78] C. A. Regal, M. Greiner, and D. S. Jin, *Observation of Resonance Condensation of Fermionic Atom Pairs*, Physical Review Letters **92**, 040403 (2004). 4

[79] M. Zwierlein, C. Stan, C. Schunck, S. Raupach, A. Kerman, and W. Ketterle, *Condensation of Pairs of Fermionic Atoms near a Feshbach Resonance*, Physical Review Letters **92**, 120403 (2004). 4

[80] M. Bartenstein, A. Altmeyer, S. Riedl, S. Jochim, C. Chin, J. Denschlag, and R. Grimm, *Crossover from a Molecular Bose-Einstein Condensate to a Degenerate Fermi Gas*, Physical Review Letters **92**, 120401 (2004). 4

[81] J. Bardeen, L. N. Cooper, and J. R. Schrieffer, *Theory of Superconductivity*, Physical Review **108**, 1175 (1957). 4

[82] T. Bourdel, L. Khaykovich, J. Cubizolles, J. Zhang, F. Chevy, M. Teichmann, L. Tarruell, S. Kokkelmans, and C. Salomon, *Experimental Study of the BEC-BCS Crossover Region in Lithium 6*, Physical Review Letters **93**, 050401 (2004). 4

[83] M. W. Zwierlein, J. R. Abo-Shaeer, A. Schirotzek, C. H. Schunck, and W. Ketterle, *Vortices and superfluidity in a strongly interacting Fermi gas.*, Nature **435**, 1047 (2005). 4

[84] M. W. Zwierlein, A. Schirotzek, C. H. Schunck, and W. Ketterle, *Fermionic superfluidity with imbalanced spin populations.*, Science (New York, N.Y.) **311**, 492 (2006). 4

[85] G. B. Partridge, W. Li, R. I. Kamar, Y.-A. Liao, and R. G. Hulet, *Pairing and phase separation in a polarized Fermi gas.*, Science (New York, N.Y.) **311**, 503 (2006). 4

[86] J. Joseph, B. Clancy, L. Luo, J. Kinast, A. Turlapov, and J. Thomas, *Measurement of Sound Velocity in a Fermi Gas near a Feshbach Resonance*, Physical Review Letters **98**, 170401 (2007). 4

[87] D. Miller, J. Chin, C. Stan, Y. Liu, W. Setiawan, C. Sanner, and W. Ketterle, *Critical Velocity for Superfluid Flow across the BEC-BCS Crossover*, Physical Review Letters **99**, 070402 (2007). 4

[88] R. Jördens, N. Strohmaier, K. Günter, H. Moritz, and T. Esslinger, *A Mott insulator of fermionic atoms in an optical lattice.*, Nature **455**, 204 (2008). 4

[89] U. Schneider, L. Hackermüller, S. Will, T. Best, I. Bloch, T. A. Costi, R. W. Helmes, D. Rasch, and A. Rosch, *Metallic and insulating phases of repulsively interacting fermions in a 3D optical lattice.*, Science (New York, N.Y.) **322**, 1520 (2008). 4

[90] M. Horikoshi, S. Nakajima, M. Ueda, and T. Mukaiyama, *Measurement of universal thermodynamic functions for a unitary Fermi gas.*, Science (New York, N.Y.) **327**, 442 (2010). 4

[91] N. Navon, S. Nascimbène, F. Chevy, and C. Salomon, *The equation of state of a low-temperature Fermi gas with tunable interactions.*, Science (New York, N.Y.) **328**, 729 (2010). 4

[92] W. Ketterle and M. Zwierlein, *Making, probing and understanding ultracold Fermi gases*, Proc. of the Int. School of Phys. Enrico Fermi **CLXIV**, 247 (2008). 4, 128

[93] M. J. H. Ku, A. T. Sommer, L. W. Cheuk, and M. W. Zwierlein, *Revealing the superfluid lambda transition in the universal thermodynamics of a unitary Fermi gas.*, Science **335**, 563 (2012). 4, 128

[94] Q. Chen, J. Stajic, S. Tan, and K. Levin, *BCS–BEC crossover: From high temperature superconductors to ultracold superfluids*, Physics Reports **412**, 1 (2005). 4

[95] M. Iskin and C. de Melo, *Superfluid and Insulating Phases of Fermion Mixtures in Optical Lattices*, Physical Review Letters **99**, 080403 (2007). 4

[96] P. Fulde and R. A. Ferrell, *Superconductivity in a Strong Spin-Exchange Field*, Phys. Rev. **135**, A550 (1964). 4

[97] A. I. Larkin and Y. N. Ovchinnikov, *Inhomogeneous state of superconductors*, Sov. Phys. JETP **20** (1965). 4

[98] M. Dalmonte, K. Dieckmann, T. Roscilde, C. Hartl, A. E. Feiguin, U. Schollwöck, and F. Heidrich-Meisner, *Dimer, trimer, and Fulde-Ferrell-Larkin-Ovchinnikov liquids in mass- and spin-imbalanced trapped binary mixtures in one dimension*, Physical Review A **85**, 063608 (2012). 4

[99] W. V. Liu and F. Wilczek, *Interior Gap Superfluidity*, Physical Review Letters **90**, 047002 (2003). 4

[100] M. M. Forbes, E. Gubankova, W. V. Liu, and F. Wilczek, *Stability Criteria for Breached-Pair Superfluidity*, Phys. Rev. Lett. **94**, 17001 (2005). 4

[101] D. S. Petrov, G. E. Astrakharchik, D. J. Papoular, C. Salomon, and G. V. Shlyapnikov, *Crystalline Phase of Strongly Interacting Fermi Mixtures*, Phys. Rev. Lett. **99**, 130407 (2007). 4

[102] J. Levinsen, T. Tiecke, J. Walraven, and D. Petrov, *Atom-Dimer Scattering and Long-Lived Trimers in Fermionic Mixtures*, Physical Review Letters **103**, 153202 (2009). 4, 5, 133

[103] J. Deiglmayr, A. Grochola, M. Repp, K. Mörtlbauer, C. Glück, J. Lange, O. Dulieu, R. Wester, and M. Weidemüller, *Formation of Ultracold Polar Molecules in the Rovibrational Ground State*, Phys. Rev. Lett. **101**, 133004 (2008). 4

[104] K.-K. Ni, S. Ospelkaus, M. H. G. de Miranda, A. Pe'er, B. Neyenhuis, J. J. Zirbel, S. Kotochigova, P. S. Julienne, D. S. Jin, and J. Ye, *A High Phase-Space-Density Gas of Polar Molecules*, Science **322**, 231 (2008). 4

[105] R. Onofrio and C. Presilla, *Ultracold Atomic Fermi–Bose Mixtures in Bichromatic Optical Dipole Traps: A Novel Route to Study Fermion Superfluidity*, Journal of Statistical Physics **115**, 57 (2004). 5

[106] A. D. Lercher, T. Takekoshi, M. Debatin, B. Schuster, R. Rameshan, F. Ferlaino, R. Grimm, and H. C. Nägerl, *Production of a dual-species Bose-Einstein condensate of Rb and Cs atoms*, The European Physical Journal D **65**, 3 (2011). 5

[107] Y. Nishida and S. Tan, *Universal Fermi Gases in Mixed Dimensions*, Phys. Rev. Lett. **101**, 170401 (2008). 5

[108] M. Olshanii, *Atomic Scattering in the Presence of an External Confinement and a Gas of Impenetrable Bosons*, Physical Review Letters **81**, 938 (1998). 5, 132

[109] T. Bergeman, M. Moore, and M. Olshanii, *Atom-Atom Scattering under Cylindrical Harmonic Confinement: Numerical and Analytic Studies of the Confinement Induced Resonance*, Physical Review Letters **91**, 163201 (2003). 5, 132

[110] H. Moritz, T. Stöferle, K. Günter, M. Köhl, and T. Esslinger, *Confinement Induced Molecules in a 1D Fermi Gas*, Physical Review Letters **94**, 210401 (2005). 5, 132

[111] G. Lamporesi, J. Catani, G. Barontini, Y. Nishida, M. Inguscio, and F. Minardi, *Scattering in Mixed Dimensions with Ultracold Gases*, Physical Review Letters **104**, 153202 (2010). 5, 132

[112] E. Haller, M. J. Mark, R. Hart, J. G. Danzl, L. Reichsöllner, V. Melezhik, P. Schmelcher, and H.-C. Nägerl, *Confinement-Induced Resonances in Low-Dimensional Quantum Systems*, Physical Review Letters **104**, 153203 (2010). 5, 132

[113] P. Anderson, *Localized Magnetic States in Metals*, Physical Review **124**, 41 (1961). 5

[114] J. Kondo, *Resistance Minimum in Dilute Magnetic Alloys*, Progress of Theoretical Physics **32**, 37 (1964). 5

[115] J. Bauer, C. Salomon, and E. Demler, *Realizing a Kondo-Correlated State with Ultracold Atoms*, Physical Review Letters **111**, 215304 (2013). 5

[116] U. Gavish and Y. Castin, *Matter-Wave Localization in Disordered Cold Atom Lattices*, Phys. Rev. Lett. **95**, 20401 (2005). 5

[117] J. Billy, V. Josse, Z. Zuo, A. Bernard, B. Hambrecht, P. Lugan, D. Clément, L. Sanchez-Palencia, P. Bouyer, and A. Aspect, *Direct observation of Anderson localization of matter waves in a controlled disorder.*, Nature **453**, 891 (2008). 5

[118] G. Roati, C. D'Errico, L. Fallani, M. Fattori, C. Fort, M. Zaccanti, G. Modugno, M. Modugno, and M. Inguscio, *Anderson localization of a non-interacting Bose-Einstein condensate.*, Nature **453**, 895 (2008). 5

[119] Y. Nishida and S. Tan, *Confinement-induced Efimov resonances in Fermi-Fermi mixtures*, Physical Review A **79**, 060701 (2009). 5, 133

[120] Y. Nishida, *Phases of a bilayer Fermi gas*, Physical Review A **82**, 011605 (2010). 5, 133

[121] L. Pollet, M. Troyer, K. Van Houcke, and S. Rombouts, *Phase Diagram of Bose-Fermi Mixtures in One-Dimensional Optical Lattices*, Physical Review Letters **96**, 190402 (2006). 5

[122] A. Zujev, A. Baldwin, R. Scalettar, V. Rousseau, P. Denteneer, and M. Rigol, *Superfluid and Mott-insulator phases of one-dimensional Bose-Fermi mixtures*, Physical Review A **78**, 033619 (2008). 5

[123] M. Taglieber, A.-C. Voigt, F. Henkel, S. Fray, T. Hänsch, and K. Dieckmann, *Simultaneous magneto-optical trapping of three atomic species*, Physical Review A **73**, 011402 (2006). 5

[124] T. Tiecke, *Feshbach resonances in ultracold mixtures of the fermionic quantum gases ^{6}Li and ^{40}K*, Ph.D. thesis, Universiteit van Amsterdam (2009). 5, 29, 103

[125] A. Ridinger, S. Chaudhuri, T. Salez, U. Eismann, D. R. Fernandes, K. Magalhães, D. Wilkowski, C. Salomon, and F. Chevy, *Large atom number dual-species magneto-optical trap for fermionic ^{6}Li and ^{40}K atoms*, The European Physical Journal D **65**, 223 (2011). 5, 9, 21

[126] E. Wille, F. Spiegelhalder, G. Kerner, D. Naik, A. Trenkwalder, G. Hendl, F. Schreck, R. Grimm, T. Tiecke, J. Walraven, S. Kokkelmans, E. Tiesinga, and P. Julienne, *Exploring an Ultracold Fermi-Fermi Mixture: Interspecies Feshbach Resonances and Scattering Properties of ^{6}Li and ^{40}K*, Physical Review Letters **100**, 053201 (2008). 5

[127] E. Tiemann, H. Knöckel, P. Kowalczyk, W. Jastrzebski, A. Pashov, H. Salami, and A. Ross, *Coupled system a Σ3+ and X Σ1+ of KLi: Feshbach resonances and corrections to the Born-Oppenheimer approximation*, Physical Review A **79**, 042716 (2009). 5, 29

[128] T. G. Tiecke, M. R. Goosen, J. T. M. Walraven, and S. J. J. M. F. Kokkelmans, *Asymptotic-bound-state model for Feshbach resonances*, Physical Review A **82**, 042712 (2010). 5

[129] T. G. Tiecke, M. R. Goosen, A. Ludewig, S. D. Gensemer, S. Kraft, S. J. J. M. F. Kokkelmans, and J. T. M. Walraven, *Broad Feshbach resonance in the ^{6}Li-^{40}K mixture*, Physical Review Letters **104**, 053202 (2010). 5

[130] D. Naik, A. Trenkwalder, C. Kohstall, F. M. Spiegelhalder, M. Zaccanti, G. Hendl, F. Schreck, R. Grimm, T. M. Hanna, and P. S. Julienne, *Feshbach resonances in the ^{6}Li-^{40}K Fermi-Fermi mixture: elastic versus inelastic interactions*, The European Physical Journal D **65**, 55 (2011). 5

[131] A.-C. Voigt, M. Taglieber, L. Costa, T. Aoki, W. Wieser, T. W. Hänsch, and K. Dieckmann, *Ultracold Heteronuclear Fermi-Fermi Molecules*, Physical Review Letters **102**, 020405 (2009). 5

[132] A. Trenkwalder, C. Kohstall, M. Zaccanti, D. Naik, A. I. Sidorov, F. Schreck, and R. Grimm, *Hydrodynamic Expansion of a Strongly Interacting Fermi-Fermi Mixture*, Physical Review Letters **106**, 115304 (2011). 5

[133] C. Kohstall, M. Zaccanti, M. Jag, A. Trenkwalder, P. Massignan, G. M. Bruun, F. Schreck, and R. Grimm, *Metastability and coherence of repulsive polarons in a strongly interacting Fermi mixture.*, Nature **485**, 615 (2012). 5

[134] M. Jag, M. Zaccanti, M. Cetina, R. S. Lous, F. Schreck, R. Grimm, D. S. Petrov, and J. Levinsen, *Observation of a Strong Atom-Dimer Attraction in a Mass-Imbalanced Fermi-Fermi Mixture*, Physical Review Letters **112**, 075302 (2014). 5

[135] K. M. O'Hara, S. L. Hemmer, M. E. Gehm, S. R. Granade, and J. E. Thomas, *Observation of a strongly interacting degenerate Fermi gas of atoms.*, Science (New York, N.Y.) **298**, 2179 (2002). 5

[136] J. T. Stewart, J. P. Gaebler, C. A. Regal, and D. S. Jin, *Potential energy of a ^{40}K Fermi gas in the BCS-BEC crossover*, Physical Review Letters **97**, 220406 (2006). 5

[137] J. Dalibard and C. Cohen-Tannoudji, *Laser cooling below the Doppler limit by polarization gradients: simple theoretical models*, Journal of the Optical Society of America B **6**, 2023 (1989). 6, 68, 76, 80

[138] P. D. Lett, W. D. Phillips, S. L. Rolston, C. E. Tanner, R. N. Watts, and C. I. Westbrook, *Optical molasses*, J. Opt. Soc. Am. B **6**, 2084 (1989). 6, 76

[139] D. S. Weiss, E. Riis, Y. Shevy, P. J. Ungar, and S. Chu, *Optical molasses and multilevel atoms: experiment*, J. Opt. Soc. Am. B **6**, 2072 (1989). 6, 76

[140] D. R. Fernandes, F. Sievers, N. Kretzschmar, S. Wu, C. Salomon, and F. Chevy, *Sub-Doppler laser cooling of fermionic ^{40}K atoms in three-dimensional gray optical molasses*, EPL (Europhysics Letters) **100**, 63001 (2012). 6, 67, 76

[141] F. Sievers, N. Kretzschmar, S. Wu, D. R. Fernandes, D. Suchet, M. Rabinovic, L. Khaykovich, C. Salomon, and F. Chevy, *Simultaneous D_1 line sub-Doppler laser cooling of fermionic ^6Li and ^{40}K*, to be published . 6, 67, 76

[142] A. T. Grier, I. Ferrier-Barbut, B. S. Rem, M. Delehaye, L. Khaykovich, F. Chevy, and C. Salomon, *Λ-enhanced sub-Doppler cooling of lithium atoms in D_1 gray molasses*, Physical Review A **87**, 063411 (2013). 6, 97, 132

[143] D. Nath, R. K. Easwaran, G. Rajalakshmi, and C. S. Unnikrishnan, *Quantum-interference-enhanced deep sub-Doppler cooling of ^{39}K atoms in gray molasses*, Physical Review A **88**, 053407 (2013). 6, 97, 132

[144] G. Salomon, L. Fouché, P. Wang, A. Aspect, P. Bouyer, and T. Bourdel, *Gray-molasses cooling of ^{39}K to a high phase-space density*, EPL (Europhysics Letters) **104**, 63002 (2013). 6, 96, 97, 132

[145] A. Burchianti, G. Valtolina, J. A. Seman, E. Pace, M. De Pas, M. Inguscio, M. Zaccanti, and G. Roati, *Efficient all-optical production of large ^6Li quantum gases using D_1 gray-molasses cooling* 5 (2014). 6, 97, 132

[146] P. M. Duarte, R. A. Hart, J. M. Hitchcock, T. A. Corcovilos, T.-L. Yang, A. Reed, and R. G. Hulet, *All-optical production of a lithium quantum gas using narrow-line laser cooling*, Physical Review A **84**, 061406 (2011). 6

[147] D. McKay, D. Jervis, D. Fine, J. Simpson-Porco, G. Edge, and J. Thywissen, *Low-temperature high-density magneto-optical trapping of potassium using the open $4S\rightarrow 5P$ transition at 405 nm*, Phys. Rev. A **84**, 63420 (2011). 6

[148] A. Ridinger, *Towards quantum degenerate Fermi mixtures : Photoassociation of weakly bound ^6Li-^{40}K molecules*, Ph.D. thesis, Université Pierre et Marie Curie - Paris VI (2011). 9, 11, 13, 14, 15, 18, 19

[149] T. Salez, *Towards quantum degenerate atomic Fermi mixtures*, Ph.D. thesis, Université Pierre et Marie Curie - Paris VI (2011). 9, 108, 111, 120

[150] K. L. Moore, T. P. Purdy, K. W. Murch, S. Leslie, S. Gupta, and D. M. Stamper-Kurn, *Collimated, single-pass atom source from a pulsed alkali metal dispenser for laser-cooling experiments*, Review of Scientific Instruments **76**, 023106 (2005). 9

[151] A. Gozzini, F. Mango, J. H. Xu, G. Alzetta, F. Maccarrone, and R. A. Bernheim, *Light-induced ejection of alkali atoms in polysiloxane coated cells*, Il Nuovo Cimento D **15**, 709 (1993). 9

[152] C. Klempt, T. van Zoest, T. Henninger, O. Topic, E. Rasel, W. Ertmer, and J. Arlt, *Ultraviolet light-induced atom desorption for large rubidium and potassium magneto-optical traps*, Physical Review A **73**, 013410 (2006). 9

[153] M. Greiner, I. Bloch, T. W. Hänsch, and T. Esslinger, *Magnetic transport of trapped cold atoms over a large distance*, Phys. Rev. A **63**, 31401 (2001). 9, 26, 108

[154] G. Ferrari, M.-O. Mewes, F. Schreck, and C. Salomon, *High-power multiple-frequency narrow-linewidth laser source based on a semiconductor tapered amplifier*, Optics Letters **24**, 151 (1999). 14

[155] W. Phillips and H. Metcalf, *Laser Deceleration of an Atomic Beam*, Physical Review Letters **48**, 596 (1982). 14

[156] H. J. Metcalf and P. van der Straten, *Laser cooling and trapping of atoms*, Journal of the Optical Society of America B **20**, 887 (2003). 14, 20

[157] K. Dieckmann, R. Spreeuw, M. Weidemüller, and J. Walraven, *Two-dimensional magneto-optical trap as a source of slow atoms*, Physical Review A **58**, 3891 (1998). 15, 16

[158] J. Schoser, A. Batär, R. Löw, V. Schweikhard, A. Grabowski, Y. Ovchinnikov, and T. Pfau, *Intense source of cold Rb atoms from a pure two-dimensional magneto-optical trap*, Physical Review A **66**, 023410 (2002). 15

[159] S. Chaudhuri, S. Roy, and C. Unnikrishnan, *Realization of an intense cold Rb atomic beam based on a two-dimensional magneto-optical trap: Experiments and comparison with simulations*, Physical Review A **74**, 023406 (2006). 15

[160] N. Castagna, J. Guéna, M. D. Plimmer, and P. Thomann, *A novel simplified two-dimensional magneto-optical trap as an intense source of slow cesium atoms*, The European Physical Journal Applied Physics **34**, 21 (2006). 15

[161] J. Catani, P. Maioli, L. De Sarlo, F. Minardi, and M. Inguscio, *Intense slow beams of bosonic potassium isotopes*, Physical Review A **73**, 033415 (2006). 15

[162] T. Tiecke, S. Gensemer, A. Ludewig, and J. Walraven, *High-flux two-dimensional magneto-optical-trap source for cold lithium atoms*, Physical Review A **80**, 013409 (2009). 15

[163] B. DeMarco, J. Bohn, J. Burke, M. Holland, and D. Jin, *Measurement of p-Wave Threshold Law Using Evaporatively Cooled Fermionic Atoms*, Physical Review Letters **82**, 4208 (1999). 28, 126

[164] F. Schreck, *Mixtures of ultracold gases: Fermi sea and Bose-Einstein condensate of Lithium isotopes*, Ph.D. thesis, Université Pierre et Marie Curie - Paris VI (2002). 29, 103

[165] S. Falke, H. Knöckel, J. Friebe, M. Riedmann, E. Tiemann, and C. Lisdat, *Potassium ground-state scattering parameters and Born-Oppenheimer potentials from molecular spectroscopy*, Physical Review A **78**, 012503 (2008). 29

[166] B. DeMarco, *Quantum behavior of an atomic Fermi gas*, Ph.D. thesis, University of Colorado (2001). 30, 127

[167] R. Grimm, M. Weidemüller, and Y. B. Ovchinnikov, *Optical dipole traps for neutral atoms* 39 (1999). 30, 127

[168] A. Keshet, *Cicero Word Generator Technical and User Manual* (2008). 37

[169] M. Teichmann, *Ultracold 6Li Atoms in the BEC-BCS Crossover: Experiments and the Construction of a New Apparatus*, Ph.D. thesis, Université Pierre et Marie Curie - Paris VI (2007). 37

[170] U. Eismann, *A novel all-solid-state laser source for lithium atoms and three-body recombination in the unitary Bose gas*, Ph.D. thesis, Université Pierre et Marie Curie - Paris VI (2012). 39, 45, 53, 64

[171] U. Eismann, A. Bergschneider, F. Sievers, N. Kretzschmar, C. Salomon, and F. Chevy, *2.1-watts intracavity-frequency-doubled all-solid-state light source at 671 nm for laser cooling of lithium*, Opt. Express **21**, 9091 (2013). 39, 45, 65

[172] N. Kretzschmar, F. Sievers, U. Eismann, C. Salomon, and F. Chevy, *2.3-watts waveguide-doubled laser at 671 nm for laser cooling of lithium*, to be published . 39, 62, 66

[173] C. Chin, R. Grimm, P. Julienne, and E. Tiesinga, *Feshbach resonances in ultracold gases*, Rev. Mod. Phys. **82**, 1225 (2010). 39

[174] F. Y. Hou, L. Yu, X. J. Jia, Y. H. Zheng, C. D. Xie, and K. C. Peng, *Experimental generation of optical non-classical states of light with 1.34 μm wavelength*, The European Physical Journal D **62**, 433 (2011). 40

[175] F. A. Camargo, T. Zanon-Willette, T. Badr, N. U. Wetter, and J.-J. Zondy, *Tunable Single-Frequency Nd:YVO4 BiB3O6 Ring Laser at 671 nm*, Quantum Electronics, IEEE Journal of **46**, 804 (2010). 40, 53

[176] U. Eismann, F. Gerbier, C. Canalias, A. Zukauskas, G. Trénec, J. Vigué, F. Chevy, and C. Salomon, *An all-solid-state laser source at 671 nm for cold-atom experiments with lithium*, Applied Physics B **106**, 25 (2011). 40, 45, 46, 49, 50, 51, 53, 54, 55, 57, 62, 63, 65

[177] A. Miffre, M. Jacquey, M. Büchner, G. Trénec, and J. Vigué, *Atom interferometry measurement of the electric polarizability of lithium*, The European Physical Journal D - Atomic, Molecular, Optical and Plasma Physics **38**, 353 (2006). 40

[178] H. Müller, S.-w. Chiow, Q. Long, S. Herrmann, and S. Chu, *Atom Interferometry with up to 24-Photon-Momentum-Transfer Beam Splitters*, Phys. Rev. Lett. **100**, 180405 (2008). 40

[179] I. E. Olivares, A. E. Duarte, E. A. Saravia, and F. J. Duarte, *Lithium Isotope Separation With Tunable Diode Lasers*, Appl. Opt. **41**, 2973 (2002). 40

[180] S. A. Payne, L. K. Smith, R. J. Beach, B. H. T. Chai, J. H. Tassano, L. D. DeLoach, W. L. Kway, R. W. Solarz, and W. F. Krupke, *Properties of Cr:LiSrAlF$_6$ crystals for laser operation*, Appl. Opt. **33**, 5526 (1994). 40

[181] H. Rast, H. Caspers, and S. Miller, *Infrared Spectral Emittance and Optical Properties of Yttrium Vanadate*, Physical Review **169**, 705 (1968). 43

[182] L. McDonagh, R. Wallenstein, R. Knappe, and A. Nebel, *High-efficiency 60 W TEM$_{00}$ Nd:YVO$_4$ oscillator pumped at 888 nm*, Opt. Lett. **31**, 3297 (2006). 44, 46

[183] S. Chénais, F. Druon, S. Forget, F. Balembois, and P. Georges, *On thermal effects in solid-state lasers: The case of ytterbium-doped materials*, Progress in Quantum Electronics **30**, 89 (2006). 44

[184] G. Trénec, W. Volondat, O. Cugat, and J. Vigué, *Permanent magnets for Faraday rotators inspired by the design of the magic sphere*, Appl. Opt. **50**, 4788 (2011). 46

[185] P. Laporta and M. Brussard, *Design criteria for mode size optimization in diode-pumped solid-state lasers*, IEEE Journal of Quantum Electronics **27**, 2319 (1991). 48

[186] Y. Chen, T. Huang, C. Kao, C. Wang, and S. Wang, *Optimization in scaling fiber-coupled laser-diode end-pumped lasers to higher power: influence of thermal effect*, IEEE Journal of Quantum Electronics **33**, 1424 (1997). 48

[187] W. W. Rigrod, *Gain Saturation and Output Power of Optical Masers*, Journal of Applied Physics **34**, 2602 (1963). 49

[188] E. Khazanov, N. Andreev, A. Mal'shakov, O. Palashov, A. Poteomkin, A. Sergeev, A. Shaykin, V. Zelenogorsky, I. Ivanov, R. Amin, G. Mueller, D. Tanner, and D. Reitze, *Compensation of thermally induced modal distortions in Faraday isolators*, IEEE Journal of Quantum Electronics **40**, 1500 (2004). 49

[189] F. Lenhardt, M. Nittmann, T. Bauer, J. Bartschke, and J. A. L'huillier, *High-power 888-nm-pumped Nd:YVO4 1342-nm oscillator operating in the TEM_{00} mode*, Applied Physics B **96**, 803 (2009). 49, 57

[190] R. Polloni and O. Svelto, *Optimum coupling for intracavity second harmonic generation*, IEEE Journal of Quantum Electronics **4**, 528 (1968). 50

[191] R. Smith, *Theory of intracavity optical second-harmonic generation*, IEEE Journal of Quantum Electronics **6**, 215 (1970). 50

[192] J.-J. Zondy, F. A. Camargo, T. Zanon, V. Petrov, and N. U. Wetter, *Observation of strong cascaded Kerr-lens dynamics in an optimally-coupled cw intracavity frequency-doubled Nd:YLF ring laser*, Opt. Express **18**, 4796 (2010). 51, 55

[193] G. D. Boyd and D. A. Kleinman, *Parametric Interaction of Focused Gaussian Light Beams*, Journal of Applied Physics **39**, 3597 (1968). 51

[194] K. Fradkin, A. Arie, A. Skliar, and G. Rosenman, *Tunable midinfrared source by difference frequency generation in bulk periodically poled $KTiOPO_4$*, Applied Physics Letters **74**, 914 (1999). 51, 53, 55

[195] S. Emanueli and A. Arie, *Temperature-Dependent Dispersion Equations for $KTiOPO_4$ and $KTiOAsO_4$*, Appl. Opt. **42**, 6661 (2003). 51, 53, 55

[196] M. Peltz, U. Bäder, A. Borsutzky, R. Wallenstein, J. Hellström, H. Karlsson, V. Pasiskevicius, and F. Laurell, *Optical parametric oscillators for high pulse energy and high average power operation based on large aperture periodically poled KTP and RTA*, Applied Physics B **73**, 663 (2001). 51

[197] K. I. Martin, W. A. Clarkson, and D. C. Hanna, *Self-suppression of axial mode hopping by intracavity second-harmonic generation*, Opt. Lett. **22**, 375 (1997). 53, 55

[198] S. Helmfrid and K. Tatsuno, *Stable single-mode operation of intracavity-doubled diode-pumped Nd:YVO_4 lasers: theoretical study*, J. Opt. Soc. Am. B **11**, 436 (1994). 53, 55

[199] W. Leeb, *Losses introduced by tilting intracavity etalons*, Applied physics **6**, 267 (1975). 53

[200] L. S. Rothman, I. E. Gordon, A. Barbe, D. Benner, P. F. Bernath, M. Birk, V. Boudon, L. R. Brown, A. Campargue, J.-P. Champion, K. Chance, L. H. Coudert, V. Dana, V. M. Devi, S. Fally, J.-M. Flaud, R. R. Gamache, A. Goldman, D. Jacquemart, I. Kleiner, N. Lacome, W. J. Lafferty, J.-Y. Mandin, S. T. Massie, S. N. Mikhailenko, C. E. Miller, N. Moazzen-Ahmadi, O. V. Naumenko, A. V. Nikitin, J. Orphal, V. I. Perevalov, A. Perrin, A. Predoi-Cross, C. P. Rinsland, M. Rotger, M. Simeckova, M. A. H. Smith, K. Sung, S. A. Tashkun, J. Tennyson, R. A. Toth, A. C. Vandaele, and J. V. Auwera, *The HITRAN 2008 molecular spectroscopic database*, Journal of Quantitative Spectroscopy and Radiative Transfer **110**, 533 (2009). 54

[201] R. DeSalvo, H. Vanherzeele, D. J. Hagan, M. Sheik-Bahae, G. Stegeman, and E. W. V. Stryland, *Self-focusing and self-defocusing by cascaded second-order effects in KTP*, Opt. Lett. **17**, 28 (1992). 54

[202] S. Holmgren, V. Pasiskevicius, and F. Laurell, *Generation of 2.8 ps pulses by mode-locking a Nd:$GdVO_4$ laser with defocusing cascaded Kerr lensing in periodically poled KTP*, Opt. Express **13**, 5270 (2005). 54

[203] C. Schäfer, C. Fries, C. Theobald, and J. A. L'huillier, *Parametric Kerr lens mode-locked, 888 nm pumped Nd:YVO_4 laser*, Opt. Lett. **36**, 2674 (2011). 54

[204] J. E. Hastie, S. Calvez, M. D. Dawson, T. Leinonen, A. Laakso, J. Lyytikäinen, and M. Pessa, *High power CW red VECSEL with linearly polarized TEM_{00} output beam*, Opt. Express **13**, 77 (2005). 57

[205] F. Lenhardt, A. Nebel, R. Knappe, M. Nittmann, J. Bartschke, and J. A. L'huillier, *Efficient Single-Pass Second Harmonic Generation of a Continuous Wave Nd:YVO_4- Laser at 1342 nm Using MgO:PPLN*, in *Conference on Lasers and Electro-Optics 2010*, CThEE5, Optical Society of America (2010). 57

[206] G. C. Bjorklund, *Frequency-modulation spectroscopy: a new method for measuring weak absorptions and dispersions*, Optics Letters **5**, 15 (1980). 61

[207] N. Kretzschmar, *PhD Thesis*, to be published, École Normale Supérieure. 62, 66

[208] C. Cohen-Tannoudji and D. Guéry-Odelin, *Advances in Atomic Physics: An Overview*, vol. 53, World Scientific (2011). 67

[209] S. Chu, *Nobel Lecture: The manipulation of neutral particles*, Reviews of Modern Physics **70**, 685 (1998). 67

[210] C. N. Cohen-Tannoudji, *Nobel Lecture: Manipulating atoms with photons*, Reviews of Modern Physics **70**, 707 (1998). 67

[211] W. D. Phillips, *Nobel Lecture: Laser cooling and trapping of neutral atoms*, Reviews of Modern Physics **70**, 721 (1998). 67

[212] T. Hänsch and A. Schawlow, *Cooling of gases by laser radiation*, Optics Communications **13**, 68 (1975). 67

[213] Y. Castin, *Les limites du refroidissement laser dans les mélasses optiques à une dimension*, Ph.D. thesis, Université Pierre et Marie Curie - Paris VI (1992). 68

[214] C. Salomon, J. Dalibard, W. D. Phillips, A. Clairon, and S. Guellati, *Laser Cooling of Cesium Atoms Below 3 μK*, Europhysics Letters (EPL) **12**, 683 (1990). 69

[215] A. Aspect, E. Arimondo, R. Kaiser, N. Vansteenkiste, and C. Cohen-Tannoudji, *Laser Cooling below the One-Photon Recoil Energy by Velocity-Selective Coherent Population Trapping*, Physical Review Letters **61**, 826 (1988). 70

[216] M. Kasevich and S. Chu, *Laser Cooling below a Photon Recoil with Three-Level Atoms*, Physical Review Letters **69**, 1741 (1992). 70

[217] F. Bardou, J.-P. Bouchaud, A. Aspect, and C. Cohen-Tannoudji, *Levy Statistics and Laser Cooling*, Cambridge University Press, Cambridge (2001). 71

[218] G. Alzetta, A. Gozzini, L. Moi, and G. Orriols, *An experimental method for the observation of r.f. transitions and laser beat resonances in oriented Na vapour*, Il Nuovo Cimento B Series 11 **36**, 5 (1976). 71, 73

[219] E. Arimondo and G. Orriols, *Nonabsorbing atomic coherences by coherent two-photon transitions in a three-level optical pumping*, Lettere Al Nuovo Cimento Series 2 **17**, 333 (1976). 71

[220] M. S. Shahriar, P. R. Hemmer, M. G. Prentiss, P. Marte, J. Mervis, D. P. Katz, N. P. Bigelow, and T. Cai, *Continuous polarization-gradient precooling-assisted velocity-selective coherent population trapping*, Phys. Rev. A **48**, R4035 (1993). 73

[221] M. Weidemüller, T. Esslinger, M. A. Ol'shanii, A. Hemmerich, and T. W. Hänsch, *A Novel Scheme for Efficient Cooling below the Photon Recoil Limit*, EPL **27**, 109 (1994). 73, 74, 75

[222] G. Grynberg and J.-Y. Courtois, *Proposal for a Magneto-Optical Lattice for Trapping Atoms in Nearly-Dark States*, EPL (Europhysics Letters) **27**, 41 (1994). 73

[223] D. Boiron, C. Triché, D. R. Meacher, P. Verkerk, and G. Grynberg, *Three-dimensional cooling of cesium atoms in four-beam gray optical molasses*, Physical Review A **52**, 3425 (1995). 73, 75

[224] T. Esslinger, F. Sander, A. Hemmerich, T. W. Hänsch, H. Ritsch, and M. Weidemüller, *Purely optical dark lattice*, Optics Letters **21**, 991 (1996). 73, 75

[225] D. Boiron, A. Michaud, P. Lemonde, Y. Castin, C. Salomon, S. Weyers, K. Szymaniec, L. Cognet, and A. Clairon, *Laser cooling of cesium atoms in gray optical molasses down to 1.1 μK*, Physical Review A **53**, R3734 (1996). 73, 75

[226] M. Ol'shaniĭ and V. Minogin, *Three-dimensional velocity-selective coherent population trapping of a (3+3)-level atom*, Optics Communications **89**, 393 (1992). 73

[227] T. Walker, D. Sesko, and C. Wieman, *Collective behavior of optically trapped neutral atoms*, Physical Review Letters **64**, 408 (1990). 73

[228] C. J. Cooper, G. Hillenbrand, J. Rink, C. G. Townsend, K. Zetie, and C. J. Foot, *The Temperature of Atoms in a Magneto-optical Trap*, Europhysics Letters (EPL) **28**, 397 (1994). 73

[229] S. Kulin, *Préparation et manipulation de paquets d'ondes atomiques ultrafroids*, Ph.D. thesis, Université Pierre et Marie Curie - Paris VI (1997). 73

[230] Y. Castin and J. Dalibard, *Quantization of Atomic Motion in Optical Molasses*, EPL **14**, 761 (1991). 80

[231] A. Migdall, J. Prodan, W. Phillips, T. Bergeman, and H. Metcalf, *First Observation of Magnetically Trapped Neutral Atoms*, Physical Review Letters **54**, 2596 (1985). 99

[232] W. Ketterle and D. E. Pritchard, *Trapping and focusing ground state atoms with static fields*, Applied Physics B Photophysics and Laser Chemistry **54**, 403 (1992). 100

[233] G. Breit and I. Rabi, *Measurement of Nuclear Spin*, Physical Review **38**, 2082 (1931). 100

[234] D. Pritchard, *Cooling Neutral Atoms in a Magnetic Trap for Precision Spectroscopy*, Physical Review Letters **51**, 1336 (1983). 102

[235] W. Petrich, M. Anderson, J. Ensher, and E. Cornell, *Stable, Tightly Confining Magnetic Trap for Evaporative Cooling of Neutral Atoms*, Physical Review Letters **74**, 3352 (1995). 102

[236] F. Schreck, G. Ferrari, K. Corwin, J. Cubizolles, L. Khaykovich, M.-O. Mewes, and C. Salomon, *Sympathetic cooling of bosonic and fermionic lithium gases towards quantum degeneracy*, Physical Review A **64**, 011402 (2001). 103

[237] H. J. Lewandowski, D. M. Harber, D. L. Whitaker, and E. A. Cornell, *Simplified System for Creating a Bose–Einstein Condensate*, Journal of Low Temperature Physics **132**, 309 (2003). 108

[238] J. Walraven and T. Hijmans, *Atomic hydrogen in magnetostatic traps*, Physica B: Condensed Matter **197**, 417 (1994). 125

[239] W. Ketterle and N. J. V. Druten, *Evaporative Cooling of Trapped Atoms*, Advances in Atomic, Molecular and Optical Physics **37**, 181 (1996). 125

[240] H. Hess, *Evaporative cooling of magnetically trapped and compressed spin-polarized hydrogen*, Physical Review B **34**, 3476 (1986). 125

[241] O. Luiten, M. Reynolds, and J. Walraven, *Kinetic theory of the evaporative cooling of a trapped gas*, Physical Review A **53**, 381 (1996). 125

[242] Y.-J. Lin, A. Perry, R. Compton, I. Spielman, and J. Porto, *Rapid production of ^{87}Rb Bose-Einstein condensates in a combined magnetic and optical potential*, Physical Review A **79**, 063631 (2009). 126, 127

[243] W. Gerlach and O. Stern, *Das magnetische Moment des Silberatoms*, Zeitschrift für Physik **9**, 353 (1922). 127

[244] E. A. Hinds and I. G. Hughes, *Magnetic atom optics: mirrors, guides, traps, and chips for atoms*, Journal of Physics D: Applied Physics **32**, R119 (1999). 127